

Coupling of single neutron configurations to collective core excitations in  $^{162}\text{Yb}$  using  $^{163}\text{Yb}$



UNIVERSITY *of the*  
WESTERN CAPE

Makuhane Abel Sithole

A thesis submitted for the degree of Master of Physical Sciences at  
the University of the Western Cape.

Supervisor: Prof. J. F. Sharpey-Schafer<sup>1</sup>

Co-supervisors: Dr. T. S. Dinoko<sup>1,4</sup>

and Dr. S. N. T. Majola<sup>2,3,4</sup>

University of the Western Cape<sup>1</sup>

University of Zululand<sup>2</sup>

University of Stellenbosch<sup>3</sup>

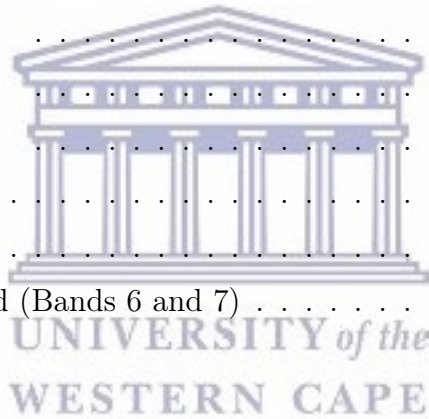
iThemba LABS<sup>4</sup>

July 2017

# Contents

<b>Declaration</b>	<b>1</b>
<b>Abstract</b>	<b>2</b>
<b>1 Introduction</b>	<b>6</b>
<b>2 Literature Review and Applicable Theory</b>	<b>9</b>
2.1 Introduction . . . . .	9
2.2 The Nuclear Shell Model . . . . .	10
2.3 Deformed Nuclei . . . . .	11
2.4 Rotational States . . . . .	13
2.5 Vibrational States . . . . .	15
2.6 The Nilsson Model. . . . .	16
2.7 Single-particle and Collective Degrees of Freedom . . . . .	19
2.7.1 The Cranked Shell Model . . . . .	20
2.8 Interaction of Radiation with Matter . . . . .	22
2.8.1 Photoelectric Absorption . . . . .	23
2.8.2 Compton Scattering . . . . .	23
2.8.3 Pair Production . . . . .	26
<b>3 Experimental Methods</b>	<b>27</b>
3.1 Reaction Choice . . . . .	27
3.2 Heavy-Ion Fusion Evaporation (HIFE) . . . . .	28
3.3 Detection of Gamma Radiation . . . . .	31
3.3.1 Semiconductor Detectors . . . . .	31
3.3.2 High-Purity Germanium (HPGe) Detectors . . . . .	32
3.3.3 Clover Detectors . . . . .	33
3.3.4 Compton Suppression Spectrometer . . . . .	34
3.3.5 The AFRODITE array . . . . .	36
3.4 Correlations of gamma transitions . . . . .	38
3.4.1 Angular Distribution and Correlation of gamma-rays . . . . .	38
3.4.2 Angular Distribution . . . . .	39
3.4.3 Angular Correlations . . . . .	40

3.4.4	Directional Correlations of Gamma Rays from Oriented States (DCO)	42
3.4.5	Linear Polarization Measurements . . . . .	43
3.5	Data Analysis . . . . .	45
3.5.1	Energy Calibration . . . . .	45
3.5.2	Efficiency Calibration . . . . .	47
3.5.3	Gamma-gamma matrix construction . . . . .	49
3.5.4	Spin and Parity Selection Rules . . . . .	51
3.5.5	Midas MTsort . . . . .	52
<b>4</b>	<b>Experimental Results</b>	<b>53</b>
4.1	Contaminants . . . . .	53
4.2	Status of the Rotational Bands in $^{163}\text{Yb}$ Nucleus . . . . .	57
4.2.1	The Yrast Band (+,+) . . . . .	57
4.2.2	Other New States . . . . .	66
4.2.3	Band 1 (-,+) . . . . .	67
4.2.4	Band 2 (-,+) . . . . .	69
4.2.5	Band 3 (+,-) . . . . .	71
4.2.6	Band 4 (-,-) . . . . .	73
4.2.7	Band 5 . . . . .	75
4.2.8	High-K Band (Bands 6 and 7) . . . . .	77
<b>5</b>	<b>Discussion</b>	<b>79</b>
5.1	The Positive Parity Bands: Yrast and Band 3 . . . . .	85
5.2	The Negative Parity Bands 2 and 5 . . . . .	86
5.3	Band 4 . . . . .	95
5.4	High-K Bands (Bands 6 and 7) . . . . .	95
<b>6</b>	<b>Conclusion</b>	<b>98</b>
<b>7</b>	<b>Future Plan</b>	<b>99</b>
<b>8</b>	<b>References</b>	<b>100</b>



## List of Figures

1	Decay scheme for the $^{163}\text{Yb}$ observed by [5] from ( $^{16}\text{O},4\text{n}$ ) data. . . . .	8
2	Diagram showing oblate, spherical and prolate shapes of the nucleus [15].	12
3	A schematic diagram showing a valence particle orbiting around a prolate deformed nucleus. This valence particle is also rotating about the x-axis with an angular velocity (rotational frequency) $\omega$ . The angular momentum caused by the collective rotation of the core is denoted by $\vec{R}$ , and it amounts to the total angular momentum $\vec{I}$ of the system when it is summed with the angular momentum of the valence nucleon $\vec{j}$ ( $= \vec{J}$ ) $\rightarrow \vec{j}$ for several valence nucleons. The projection of $\vec{j}$ ( $= \vec{J}$ ) and $\vec{I}$ onto the symmetry axis is $\Omega$ ( $= \mathbf{K}$ , although, $\mathbf{I}_x$ is the projection of $\vec{I}$ onto the rotational axis [18].	14
4	Schematic representation of the different vibrational modes of a liquid drop.	15
5	The Nilsson diagram for protons in the $52 \leq Z \leq 82$ region, showing the single-particle energies as a function of the deformation parameter $\varepsilon_2$ . The labelling convention is $\Omega[\text{N}n_z\Lambda]$ , where N is a major harmonic oscillator shell quantum number, $n_z$ is the number of nodes in the wave-function in the z direction and $\Lambda$ is the component of angular momentum along the symmetry axis or z-axis. $\Omega = \Lambda + \Sigma$ is the projection of $j = I + s$ onto the z-axis. Also positive-parity states is denoted by solid lines while dashed lines represent negative-parity states [21, 19]. . . . .	17
6	The Nilsson diagram for neutrons in the $82 \leq Z \leq 126$ region, showing the single-particle energies as a function of the deformation parameter $\varepsilon_2$ . The labelling convention is $\Omega[\text{N}n_z\Lambda]$ , where N is a major harmonic oscillator shell quantum number, $n_z$ is the number of nodes in the wave-function in the z direction and $\Lambda$ is the component of angular momentum along the symmetry axis or z-axis. $\Omega = \Lambda + \Sigma$ is the projection of $j = I + s$ onto the z-axis. Also positive-parity states is denoted by solid lines while dashed lines represent negative-parity states [21, 19]. . . . .	18

7	Illustration of the labelling of orbitals in various models and the salient features implied by the cranking term, for the s-d shell orbits. This diagram also shows how some levels have a very strong dependence on the rotational frequency $\omega$ , these are orbits corresponding to large j and small K values. The signatures $\alpha = +$ and $\alpha = -$ correspond to $\alpha = +1/2$ and $\alpha = -1/2$ , respectively [27]. . . . .	21
8	Relative importance of the three photon interaction mechanisms and their energy regions of dominance [33]. . . . .	22
9	Schematic of the mechanism of the photoelectric absorption process. . . . .	24
10	Schematic of the mechanism of the Compton Scattering process. . . . .	24
11	A polar plot of the Klein-Nishina formula [33]. . . . .	25
12	Schematic of the mechanism of the pair production-annihilation process. . . . .	26
13	PACE4 simulation of the residual nucleus yield (in percentage %) as a function of $^{16}\text{O}$ bombarding energy of a $^{152}\text{Sm}$ target. . . . .	28
14	Simple demonstration of how different residual nuclei are populated due to exit channels. Each exit channel is associated to its specific cross section, which indicates the probability for the nuclear reaction to proceed through it [38]. . . . .	29
15	A diagram of the heavy-ion fusion evaporation process, along with a time scale. An accelerated projectile nucleus collides and fuses with a target nucleus forming a compound system. The compound system first cools by evaporation of neutrons, protons and /or alpha particles. It then loses the rest of its excitation energy and almost all of its initial angular momentum by the emission of gamma rays. The total decay process is completed very quickly, in about $10^{-9}$ seconds [39]. . . . .	30
16	Illustration of a typical coaxial n-type HPGe detector and its crystal [29]. . . . .	32
17	A picture of Clover detector that can fit into a BGO shield with its cylindrical liquid nitrogen dewar and the crystal arrangement of a 4 segment Clover detector [30]. . . . .	33
18	Schematic of a Compton suppressed spectrometer (CSS) made up of several collimated HPGe detectors axially surrounded by BGO shields [29]. . . . .	34

19	Spectra from a $^{60}\text{Co}$ source showing the dramatic difference in the P/T ratio with the employment of Compton Suppression. The Compton suppressed Ge detector has a P/T ratio of about 60% and unsuppressed Ge detector has a P/T ratio of about 20%. This means that 80% of the events collected are background in the unsuppressed case [35]. . . . .	35
20	Photo showing HPGe clover detectors in BGO escaped suppressed shield in the AFRODITE array. . . . .	36
21	Schematic of initial orientation in fusion-evaporation reactions [42]. . . . .	38
22	Gamma correlation measurement setup. Coincident measurements of consecutive gammas are performed [45]. . . . .	40
23	Schematic diagram showing level scheme for two successive gamma rays. . . . .	41
24	The angles in a directional correlation of two successive radiations emitted from an axially oriented state (DCO). . . . .	42
25	Linear polarization measurements using a clover detector. . . . .	43
26	The setup showing linear polarization measurements of gamma-rays [49]. . . . .	44
27	The schematic mapping of the quadratic equation $E = a_0 + a_1x + a_2x^2$ and the linear equation $E = 0.5x'$ [35]. . . . .	46
28	Relative efficiency curve for all 8 AFRODITE clover detectors measured with a $^{152}\text{Eu}$ radioactive source. . . . .	48
29	Time spectrum used for extraction of coincidence events obtained in the current experiment. Typical events occurred in the gate 987-1010 ns. . . . .	49
30	Background-subtracted total projection Spectrum (gamma-gamma coincidences $2.5 \times 10^9$ ). The gamma rays labelled in black colour belong to $^{164}\text{Yb}$ and are produced by 4n channel. The gamma labelled in maroon belongs to $^{162}\text{Yb}$ and was produced by 6n channel of the present heavy-ion fusion evaporation reaction. The gamma rays labelled in green belong in both $^{163}\text{Yb}$ , and $^{164}\text{Yb}$ nuclei. The gamma rays labelled in red belong to $^{152}\text{Sm}$ and are produced by the coulomb excitation of the target. The gamma rays belonging to $^{163}\text{Yb}$ are produced by the 5n channel of the present HIFE reaction and are labelled in violet colour. . . . .	50
31	Partial level scheme of $^{164}\text{Yb}$ . . . . .	55

32	Coincidence spectrum from the $^{152}\text{Sm}(^{16}\text{O},5\text{n})^{163}\text{Yb}$ and $^{152}\text{Sm}(^{16}\text{O},\alpha3\text{n})^{161}\text{Er}$ reactions obtained by setting a gate on the transition at 198 keV. The yrast sequence in $^{161}\text{Er}$ is labelled in violet. Transitions labelled in black belong to $^{163}\text{Yb}$ , and $^{164}\text{Yb}$ . . . . .	56
33	Coincidence spectrum from the $^{152}\text{Sm}(^{16}\text{O},5\text{n})^{163}\text{Yb}$ reaction obtained by setting a gate on the transition 345 keV. . . . .	58
34	Partial level scheme of $^{163}\text{Yb}$ deduced from the current work, showing previously known bands. Findings from the current work are labelled in red. . . . .	59
35	The complete level scheme of $^{163}\text{Yb}$ deduced from the current work. Findings from the current work are labelled in red while previously known transitions, deduced from previous in-beam work are labelled in black. . . . .	60
36	Polarization spectrum used to calculate linear polarization anisotropy in $^{163}\text{Yb}$ (see equation 21). . . . .	62
37	DCO spectrum of the matrix constructed for the measurements of $R_{DCO}$ ratios projected onto $135^0$ in $^{163}\text{Yb}$ nucleus. . . . .	63
38	Partial level scheme of $^{163}\text{Yb}$ showing new nuclear levels transition, (highlighted in red). . . . .	64
39	Experimentally measured DCO ratios, ( $R_{DCO}$ ), in $^{163}\text{Yb}$ , deduced in the current work versus gamma-ray energies. . . . .	65
40	Plot for polarization anisotropy measurements as a function of energy obtained from this work. . . . .	66
41	Coincidence spectrum from the $^{152}\text{Sm}(^{16}\text{O},5\text{n})^{163}\text{Yb}$ reaction obtained by setting a gate on the transition 670 keV. Transitions labelled in violet are E2 transitions that belong to band 1, and transitions labelled in black are also E2 transitions that belong to band 2 and the yrast band of $^{163}\text{Yb}$ nucleus. . . . .	67
42	Coincidence spectrum from the $^{152}\text{Sm}(^{16}\text{O},5\text{n})^{163}\text{Yb}$ reaction obtained by setting a gate on the transition 468 keV. Transitions labelled in violet are E2 transitions that belong to band 2, labelled in black are also E2 transitions of the yrast band. . . . .	69
43	Coincidence spectrum from the $^{152}\text{Sm}(^{16}\text{O},5\text{n})^{163}\text{Yb}$ reaction obtained by setting a gate on the transition 220 keV. . . . .	71

44	Coincidence spectrum from the $^{152}\text{Sm}(^{16}\text{O},5\text{n})^{163}\text{Yb}$ reaction obtained by setting a gate on the transition 590 keV. Transitions labelled in violet are E2 transitions that belong to band 4, while those labelled in black are E2 transitions of yrast band. The transition labelled in red is the new E1 transition that connects band 4 and the yrast band and also the E2 transition which extend band 4 up to spin $51/2^-$ . . . . .	73
45	Coincidence spectrum from the $^{152}\text{Sm}(^{16}\text{O},5\text{n})^{163}\text{Yb}$ reaction obtained by setting a gate on the newly observed transition 539 keV. Newly observed transitions are labelled in red, the known transitions of this band are labelled in violet and the transitions labelled in black belong to the yrast band in the present coincidence spectrum. . . . .	75
46	Coincidence spectrum from the $^{152}\text{Sm}(^{16}\text{O},5\text{n})^{163}\text{Yb}$ reaction obtained by setting a gate on the transition at 189 keV. Transitions labelled in red belong to the high-K band. . . . .	77
47	Alignments deduced for bands in $^{163}\text{Yb}$ as function of $\hbar\omega$ in the current work. The labels in the legends indicate the bands as they are labelled in Figure 35. The reference parameters are chosen to be $\mathcal{J}_0 = 23\hbar^2.\text{MeV}^{-1}$ and $\mathcal{J}_1 = 90\hbar^4.\text{MeV}^{-3}$ for $^{163}\text{Yb}$ . The alignment for the ground state band of $^{162}\text{Yb}$ is also shown for comparison. Here, Harris parameterization with values $\mathcal{J}_0 = 20\hbar^2.\text{MeV}^{-1}$ and $\mathcal{J}_1 = 90\hbar^4.\text{MeV}^{-3}$ are used for $^{162}\text{Yb}$ [54]. . .	81
48	Experimental Routhians (single-particle energies in the rotating frame) plotted against rotational frequency, $\hbar\omega$ for bands belonging to $^{163}\text{Yb}$ . The Harris parameters used for the reference are $\mathcal{J}_0 = 23\hbar^2.\text{MeV}^{-1}$ and $\mathcal{J}_1 = 90\hbar^4.\text{MeV}^{-3}$ . Signature partner bands are labelled in the same colours. Open symbols denote positive signature and closed symbols represent negative signature. . . . .	82



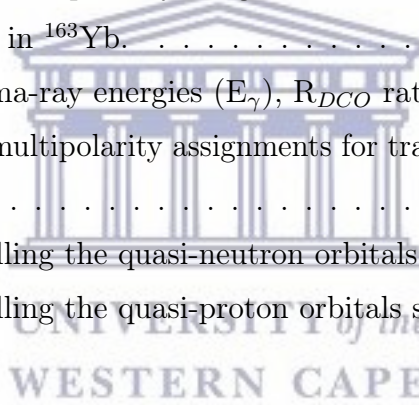
49	<p>cranked shell model diagram of quasi-particle routhians for <math>^{162}\text{Yb}</math> neutrons. The rotational frequency in this diagram denoted by <math>\omega/\omega_0</math>, is expressed in units of the oscillator frequency <math>\omega_0</math>. The quasi-particle routhians, are expressed in units of the harmonic oscillator energy <math>\hbar\omega_0</math>. Full lines are used for quasi-particle trajectories with positive parity and signature <math>\alpha = 1/2</math>, that is <math>(+,1/2)</math>. Short-dashed lines are used for quasi-particle trajectories with positive parity and signature <math>\alpha = -1/2</math>, that is <math>(+,-1/2)</math>. Dot-dashed lines are used for quasi-particle trajectories with negative parity and signature <math>\alpha = 1/2</math>, that is <math>(-,1/2)</math>. Long-dashed lines are used for quasi-particle trajectories with negative parity and signature <math>\alpha = -1/2</math>, that is <math>(-,-1/2)</math> [55]. The labelling convention used for the Routhian energies shown in the plot are given in Table 10. . . . .</p>	88
50	<p>cranked shell model diagram of quasi-particle routhians for <math>^{162}\text{Yb}</math> protons. The rotational frequency in this diagram denoted by <math>\omega/\omega_0</math>, is expressed in units of the oscillator frequency <math>\omega_0</math>. The quasi-particle routhians, are expressed in units of the harmonic oscillator energy <math>\hbar\omega_0</math>. Full lines are used for quasi-particle trajectories with positive parity and signature <math>\alpha = 1/2</math>, that is <math>(+,1/2)</math>. Short-dashed lines are used for quasi-particle trajectories with positive parity and signature <math>\alpha = -1/2</math>, that is <math>(+,-1/2)</math>. Dot-dashed lines are used for quasi-particle trajectories with negative parity and signature <math>\alpha = 1/2</math>, that is <math>(-,1/2)</math>. Long-dashed lines are used for quasi-particle trajectories with negative parity and signature <math>\alpha = -1/2</math>, that is <math>(-,-1/2)</math> [55]. The labelling convention used for the Routhian energies shown in the plot are given in Table 11. . . . .</p>	89
51	<p>A plot of experimental excitation energies minus a rigid rotor for all bands in <math>^{163}\text{Yb}</math>. Open symbols denote positive signature and closed symbols represent negative signature. . . . .</p>	90
52	<p>Compilation of experimental excitation energies minus a rigid rotor for the <math>3/2^-</math> [521] and <math>5/2^+</math> [642] signature partner bands in <math>^{157}\text{Gd}</math> [58], <math>^{159}\text{Dy}</math> [59], <math>^{161}\text{Er}</math> [5], and <math>^{163}\text{Yb}</math>. The addition of band 4 in <math>^{163}\text{Yb}</math> is to show the signature inversion around <math>10 \hbar</math>. Signature partner bands are labelled in the same colours. Open symbols denote positive signature and closed symbols represent negative signature. . . . .</p>	91

53	Compilation of Routhian plots for the $3/2^-$ [521] and $5/2^+$ [642] signature partner bands in $^{157}\text{Gd}$ , $^{159}\text{Dy}$ , $^{161}\text{Er}$ , and $^{163}\text{Yb}$ . The Harris parameters for $^{157}\text{Gd}$ : $\mathcal{J}_0 = 27.3\hbar^2.\text{MeV}^{-1}$ and $\mathcal{J}_1 = 256.6\hbar^4.\text{MeV}^{-3}$ , $^{159}\text{Dy}$ : $\mathcal{J}_0 = 28\hbar^2.\text{MeV}^{-1}$ and $\mathcal{J}_1 = 110\hbar^4.\text{MeV}^{-3}$ , $^{161}\text{Er}$ : $\mathcal{J}_0 = 26\hbar^2.\text{MeV}^{-1}$ and $\mathcal{J}_1 = 90\hbar^4.\text{MeV}^{-3}$ , and $^{163}\text{Yb}$ : $\mathcal{J}_0 = 23\hbar^2.\text{MeV}^{-1}$ and $\mathcal{J}_1 = 90\hbar^4.\text{MeV}^{-3}$ . Signature partner bands are labelled in the same colours. Open symbols denote positive signature and closed symbols represent negative signature. . . . .	92
54	Compilation of spin alignment plots for the $3/2^-$ [521] and $5/2^+$ [642] signature partner bands in $^{157}\text{Gd}$ , $^{159}\text{Dy}$ , $^{161}\text{Er}$ , and $^{163}\text{Yb}$ . The Harris parameters for $^{157}\text{Gd}$ : $\mathcal{J}_0 = 27.3\hbar^2.\text{MeV}^{-1}$ and $\mathcal{J}_1 = 256.6\hbar^4.\text{MeV}^{-3}$ [60], $^{159}\text{Dy}$ : $\mathcal{J}_0 = 28\hbar^2.\text{MeV}^{-1}$ and $\mathcal{J}_1 = 110\hbar^4.\text{MeV}^{-3}$ , $^{161}\text{Er}$ : $\mathcal{J}_0 = 26\hbar^2.\text{MeV}^{-1}$ and $\mathcal{J}_1 = 90\hbar^4.\text{MeV}^{-3}$ , and $^{163}\text{Yb}$ : $\mathcal{J}_0 = 23\hbar^2.\text{MeV}^{-1}$ and $\mathcal{J}_1 = 90\hbar^4.\text{MeV}^{-3}$ . Signature partner bands are labelled in the same colours. Open symbols denote positive signature and closed symbols represent negative signature. . . . .	93
55	Compilation of B(E1)/B(E2) ratios as a function of spin for $3/2^-$ [521] bands in $^{161}\text{Yb}$ , $^{159}\text{Dy}$ and in $^{163}\text{Yb}$ . . . . .	94
56	Compilation of the experimental excitation energies, minus the rigid rotor plots for the $11/2^-$ [505], $3/2^-$ [521] and $5/2^+$ [642] signature partner bands in $^{159}\text{Dy}$ [58], $^{161}\text{Er}$ [59], and $^{163}\text{Yb}$ [5]. The Signature partner bands are labelled in the same colours. Open symbols denote positive signature and closed symbols represent negative signature. . . . .	96
57	Compilation of B(M1)/B(E2) ratios as a function of spin for $11/2^-$ [505] bands in $^{163}\text{Yb}$ , $^{161}\text{Er}$ , and the $11/2^-$ [505] bands in $^{159}\text{Dy}$ [59, 58]. . . . .	97

## List of Tables

1	Indicates the sign of the linear polarization of gamma-rays for different radiation type. . . . .	44
2	Energy versus % yields from PACE4. In this work a beam of $E_{lab} = 93$ MeV was used. . . . .	54
3	Energy levels, gamma-ray energies ( $E_\gamma$ ), $R_{DCO}$ ratios, linear polarization anisotropy $A_p$ , and multipolarity (multi.) assignments of transitions depopulating the yrast band. . . . .	61

4	Energy levels, gamma-ray energies ( $E_\gamma$ ), $R_{DCO}$ ratios, linear polarization anisotropy $A_p$ , and multipolarity assignments of transitions depopulating band 1 in $^{163}\text{Yb}$ . . . . .	68
5	Energy levels, gamma-ray energies ( $E_\gamma$ ), $R_{DCO}$ ratios, linear polarization anisotropy $A_p$ , and multipolarity assignments of transitions depopulating the rotational levels of band 2. . . . .	70
6	Energy levels, gamma-ray energies ( $E_\gamma$ ), $R_{DCO}$ ratios, linear polarization anisotropy $A_p$ , and multipolarity assignments of transitions depopulating the rotational levels of band 3 in $^{163}\text{Yb}$ . . . . .	72
7	Energy levels, gamma-ray energies ( $E_\gamma$ ), $R_{DCO}$ ratios, linear polarization anisotropy $A_p$ , and multipolarity assignments of transitions depopulating the rotational levels of band 4 in $^{163}\text{Yb}$ . . . . .	74
8	Energy levels, gamma-ray energies ( $E_\gamma$ ), $R_{DCO}$ ratios, linear polarization anisotropy $A_p$ , and multipolarity assignments of transitions depopulating the rotational levels in $^{163}\text{Yb}$ . . . . .	76
9	Energy levels, gamma-ray energies ( $E_\gamma$ ), $R_{DCO}$ ratios, linear polarization anisotropy $A_p$ , and multipolarity assignments for transitions in $^{163}\text{Yb}$ decay scheme. . . . .	78
10	Convention for labelling the quasi-neutron orbitals shown in Figure 49. . . . .	83
11	Convention for labelling the quasi-proton orbitals shown in Figure 50. . . . .	84



# Declaration

I, the undersigned, hereby declare that the work contained in this thesis is my own original work and that I have not previously in its entirety or in part submitted it at any university for a degree.

Signature.....

Date.....



UNIVERSITY *of the*  
WESTERN CAPE

## Abstract

In odd-nuclei the single nucleon can couple to collective excitations of its even-even core nucleus [1]. These collective excitations lie within the pairing gap and are therefore the lowest energy excitations of the core [1]. Our physics motivation is to search for structures where an odd neutron couples to collective excitations of the  $^{162}\text{Yb}$  core. We also searched for high-K structures in this nucleus. The experiment  $^{152}\text{Sm}(^{16}\text{O},5\text{n})^{163}\text{Yb}$  at  $E_{lab} = 93$  MeV was performed to study  $^{163}\text{Yb}$  at iThemba LABS. The gamma-decays from the reaction products have been detected using the AFRODITE (AFRican Omnipurpose Detector for Innovative Techniques and Experiments) gamma-ray spectrometer [2] equipped with 8 escape-suppressed clover detectors. After a comprehensive analysis, the level scheme of  $^{163}\text{Yb}$  has been extended and new bands have been established in this current work, in particular the band based on the ground state has been built up to spin  $43/2^-$ . A high-K band has been established in the current work for the first time in this nucleus. An additional 16 new states in  $^{163}\text{Yb}$  were observed and all decay to the yrast band. Directional Correlations of Gamma Rays from Oriented States (DCO) and polarization analysis were performed to determine the spin and parity of new levels. The cranked shell model was used for comparison of experimental data in this work.



UNIVERSITY of the  
WESTERN CAPE

# Dedication

Am dedicating this thesis to my little girl Precious, this is for you girl, you will always be my precious gift from God daddy loves you.



UNIVERSITY *of the*  
WESTERN CAPE

## Acknowledgements

First I would like to thank God who gave me this precious life, and for placing an open door of success before me that no one can shut. “History of all great works is to witness that no great work was ever done without either the active or passive support a person’s surrounding and one’s close quarters”.

I am thankful to my supervisor Prof. J.F. Sharpey-Schafer, whose expertise in nuclear physics, generous guidance, understanding, and support made me to work on a great topic of my interest. It was a pleasure working with him.

Word of appreciation to Dr. T.S. Dinoko for all his contribution he made in this thesis, including showing me how to do my data analysis, teaching me all the programs (eg, xmgrace) I used to plot all my spectra and all plots in my thesis, reading my thesis and coming up with useful suggestions.

Thanks to Dr. S.N.T. Majola for all the sacrifice and effort you put in this project. He is a selflessness person, he put all his own post doctoral work on hold to ensure that this project is completed. He helped me a lot in analysing and interpreting my level scheme. To me he is a mentor, friend and brother, Ndo livhuwa vho dokotela Majola.

I am grateful to Ms. N. Khumalo for helping me with the information needed to sort my data. Thanks to UWC Physics staff, AFRODITE staff and NRF for their contributions to this thesis.

To Dr. R. Nchodu, thanks for his guidance, involvement, support and contribution in this thesis.

To Prof. R. Lindsay, thanks for his guidance, involvement and contribution in this thesis.

Thanks to these two best colleagues of mine, Mr. L. Mdletshe and Ms. S. Jongile for working as a team.

Word of appreciation to Dr. Obed Shirinda for showing me how to use cranked shell model to interpret my results.

To A. Kunyana thanks Mfana for being a friend .

To pastor Sumbana M.P. (My mother in Christ), Ndo livhuwa ngeletshedzo yavho, u di netisa havho, vha tshi itela uri ndi vhe na vhu matshelo ha vhudi.

To my family and friends thanks for your support and guidance.

To A. Ndou, thanks for being a lovely girl friend to me love you nana.

To N.J. Mukwevho, thanks for being lovely friend (brother) to me.

To Fatima, Na khensa nwana mhani ka leswi u ni edleleke swona e vutonwini, Xikwembu a xi ku katekise.

Last but not the least, I would also like to give thanks to the people I could not mention here but have played a wonderful role to motivate me.





# Contents

## Chapter 1

### 1 Introduction

In the last 20 years, no detailed spectroscopy has been carried out for some nuclei in the transitional rare earth region, in particular the nucleus of interest and its neighbouring nuclei, except for the recent comprehensive search of triaxially superdeformed bands [3]. This work focuses mainly on the spectroscopy of  $^{163}\text{Yb}$ , an  $N = 93$  nucleus, located in the transitional rare earth region. The majority of nuclei in this region ( $N \sim 90$ ) are predominantly known for their rich spectroscopy, which is a consequence of the investigative works that have been carried out at high spin, in the last two to three decades. The apparent lack of understanding about the formation of the majority of experimental features observed at low spin, has suddenly renewed the interest on the spectroscopy of these nuclei. For instance, a wealth of experimental data collected over the past 10 years, mainly at iThemba LABS (Laboratory for Accelerator Based Sciences), has led to an alternative interpretation of the low-lying first excited  $0^+$  states [3, 4]. On one hand, the traditional description of these states has always been that they are a  $\beta$  vibration along the nuclear symmetry axis. On the other hand, the latest interpretation describes these bands as the  $2p$ - $2h$  states configurations, which have nothing to do with vibrational collectivity- as is the case in the frame-work of Bohr and Mottelson.

In search for a more accurate description of the microscopic nature of the above-mentioned low-lying  $K^\pi = 0^+$  state in  $N \sim 90$  even-even nuclei, Sharpey-Schafer *et al.*, [3, 4] recently pointed out the importance of the coupling of the single-particle orbitals in the neighbouring odd- $N$  nucleus to the collective excitations of the neighbouring  $\Omega$  in an odd-mass nucleus. Experimentally, such coupling in the neighbouring odd-nucleus can be manifested by  $K_{<} = |\Omega - 2|$  and  $K_{>} = \Omega + 2$ , which respectively correspond to the anti-parallel or parallel coupling mode of a  $K^\pi = 2^+ \gamma$  vibrational band, such couplings have been reported in  $^{155}\text{Gd}$ ,  $^{155}\text{Dy}$ ,  $^{157}\text{Dy}$ ,  $^{159}\text{Er}$ ,  $^{165}\text{Ho}$ ,  $^{167}\text{Er}$ , and other nuclei in the 150-160

mass region. Sparse experimental evidence to date suggest that a  $K^\pi = 2^+$  band-head will be informative as it give clues to the particle-excited core interaction and the underlying microstructure of the collective  $K^\pi = 2^+$  core excitation.

In the core nucleus  $^{162}\text{Yb}$  there should also be high-K bands. The high-K bands in  $^{162}\text{Yb}$  are also expected to couple to the single quasi-neutron orbitals in  $^{163}\text{Yb}$  and they are of considerable interest in this work. The high-K band built on the  $11/2^- [505]$  orbital has not been observed in  $^{163}\text{Yb}$ , and we intend to search for this structure in the current work.

The experiment was performed at iThemba LABS, using the AFRODITE (African Omnipurpose Detector for Innovative Techniques and Experiments) array, to help in understanding the detailed spectroscopy of the  $^{163}\text{Yb}$  nucleus. The last experiments carried in this nucleus, were to study the backbending behaviour of this nucleus [5] and to search for band crossing and signature splitting (see Figure 1) [6].



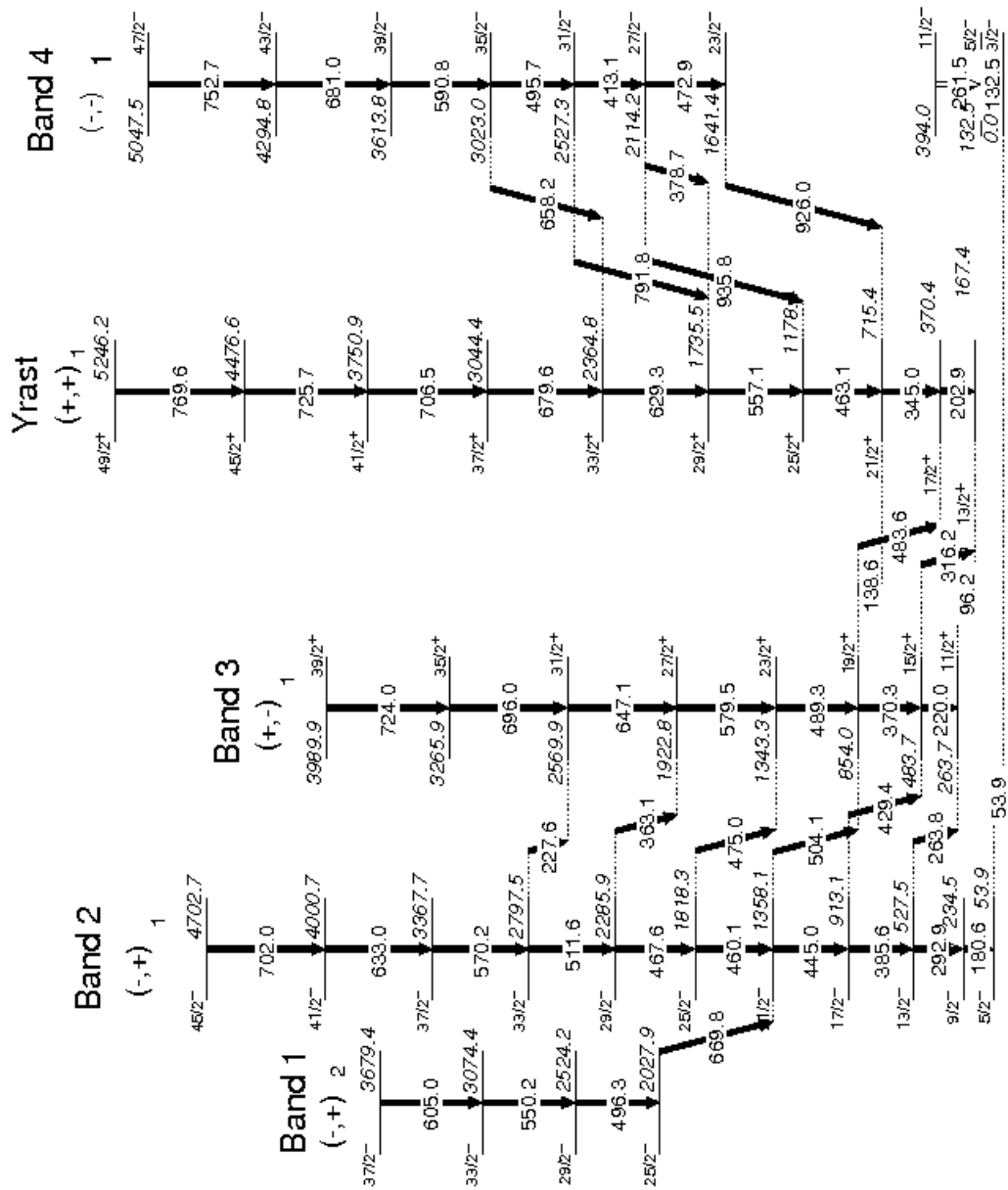


Figure 1: Decay scheme for the  $^{163}\text{Yb}$  observed by [5] from  $(^{16}\text{O}, 4n)$  data.

## Chapter 2

# 2 Literature Review and Applicable Theory

## 2.1 Introduction

The picture of the nuclear system, and forces that governs it, remain illusive. This is because the size of the nucleus is very small and nuclear forces are far more complicated than other well-known forces. Due to lack of detailed knowledge of nuclear forces, nuclear models have been developed, each of which is useful in more or less limited fashion. In order to understand and predict the properties of a nucleus, we have to understand how nuclear forces influence the behaviour of the nucleus. In nuclei, this is achieved by choosing an oversimplified theory which possess mathematical descriptions that have been successfully used to explain physical systems with properties similarly to those of a nucleus. If this theory is fairly successful in accounting for at least a few properties of the nucleus, we can then improve the model by adding additional terms such that it can account for as many observables as possible. A good nuclear model must have the ability to account for previously measured nuclear properties. Also, it should have the ability to predict additional nuclear properties that can be measured in new experiments. The earlier model(s) treated the nucleus like a drop of liquid, whereby nucleons present in the nucleus interact very strongly among themselves. Other instrumental models which have been useful since the early days to date were constructed in analogy with the shell model of the atom. Within this framework, the nucleons are weakly interacting among themselves and constrained in a mean-field. This approach gave rise to the Fermi gas model, shell model, Nilsson model, etc [7].

## 2.2 The Nuclear Shell Model

Although the liquid drop model contributed a lot in understanding the bulk properties of nuclei, it has some limitations. In fact this model fails to account for some of the observables that are due to shell effects. In an attempt to address these limitations, the shell model, analogous to that of the atomic shell model, was adopted in nuclear theory [8]. This model states that; the motion of each nucleon is controlled by the average attractive force of all the other nucleons. The resulting orbits form “shells”, just as the electrons in case of the atoms. The nucleons are added to the nucleus and they drop into the lowest energy shells available, as permitted by the Pauli exclusion principle. This model was very successful in accounting for the shell effects mentioned above, and in explaining the origin of magic numbers once a spin-orbit force was added. Some of the magic numbers for nuclear shell closures are 2, 8, 20, 28, 50, 82, and 126. For example,  $^{116}\text{Sn}$  has a magic number of protons (50) and  $^{54}\text{Fe}$  has a magic number of neutrons (28) [9]. Some nuclei for example  $^{40}\text{Ca}$  and  $^{208}\text{Pb}$ , have magic numbers for both protons and neutrons, these nuclei have exceptional stability and are called “doubly magic” [9]. Filled shells have a total angular momentum,  $J$ , equal to zero. The outer most nucleon near the fermi-surface (a valence nucleon) determines the spin  $J$  of the new ground state. When nucleons (single or pairs) are excited out of the ground state they change the angular momentum of the nucleus as well as its parity and isospin projection quantum numbers. The shell model describes how much energy is required to move nucleons from one orbit to another and how the quantum numbers change. Quantum mechanics and shell-model theory permit nuclear scientists to compute the transition probability (rate of decay) between nuclear states [9]. For nuclei whose structure can be described by a small number of valence nucleons outside filled shells, the shell model calculations agree very well with the measured values of spin, parity assignments and transition probabilities [9]. Over the years nuclear scientists have been refining the shell model in order to understand the details of nuclear structure and to make that knowledge available for applications in other nuclear technology [10].

## 2.3 Deformed Nuclei

The phenomenon of nuclear deformation has a long and interesting history. As early as 1924 it was suggested by Pauli [11] that the hyperfine structure of atomic and molecular energy levels resulted from the electromagnetic interaction with nonspherical atomic nuclei. The experimental evidence was given ten years later by Schüler and Schmidt [12]. The fact that nuclei need not to be spherical was then emphasized by N. Bohr in his classic paper on the nuclear liquid drop model [13] in which he introduced the concept of nuclear shape vibrations [14]. Nuclear deformations play a crucial role in nuclear physics because they explain many nuclear properties such as nuclear shapes. A nucleus with a completely filled shell of protons and neutrons is spherical in shape but other nuclei are deformed in shape. These deformed shapes arise because these nuclei can lower their energy by rearranging their protons and neutrons into deformed shells that accommodate different number of nucleons. The general nuclear shape can be expressed as:

$$R(\theta, \varphi) = R_0 \left[ 1 + \sum_{\lambda\mu} \alpha_{\lambda\mu} Y_{\lambda}^{\mu}(\theta, \varphi) \right] \quad (1)$$

where  $R(\theta, \varphi)$  is the distance from the center of the nucleus to the surface.

$R_0$  is the radius of the sphere of the same volume, and

$\alpha_{\lambda\mu}$  are the coefficients of the spherical harmonics  $Y_{\lambda}^{\mu}(\theta, \varphi)$ .

Different  $\alpha_{\lambda\mu}$  corresponding to different types of deformations and shapes are shown in Figure 2. Figure 2 also shows that the quadrupole deformation parameter, usually denoted by  $\beta_2, \varepsilon_2, or \delta_2$ , can be used for distinguishing between prolate and oblate deformation. This association is mainly dependent on the quadrupole deformation sign. For instance a negative value of  $\varepsilon_2$  corresponds to an oblate shape whereas a positive value of  $\varepsilon_2$  reflects the elongation of a nucleus into a prolate shape [15].

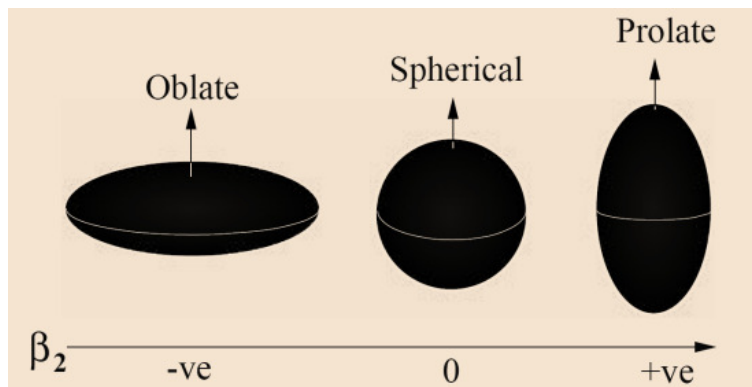


Figure 2: Diagram showing oblate, spherical and prolate shapes of the nucleus [15].

## 2.4 Rotational States

Collective rotational motion can only be observed in nuclei with a non-spherical shape. This is related to the fact that, in quantum mechanics, a wave function representing a perfectly spherical symmetric system has no preferred direction in space and a rotation does not lead to any observable change. Therefore, the rotational energy of the nuclear system can only be measured if there is a deviation from spherical symmetry. If the nucleons in a nucleus couple to give a net spin of zero in the ground state, as is the case for an even-even nucleus, the rotational angular momentum is the same as the total nuclear angular momentum  $I$  (quantum number  $l$ ) of the total wave function  $Y_l^M(\theta, \phi)$  also known as a spherical harmonic, which describes the rotation of the states. Here it is worth noting that  $M$  is the projection of  $l$  along the symmetry  $z$ -axis. The parity of this wave function, therefore, is  $(-1)^l$ . The magnitude of the rotational angular momentum is given by  $\hbar\omega$  where  $\omega$  is the angular frequency of the rotation (see Figure 3) and  $\mathcal{J}$  is the moment of inertia. The expression for determining energies of a rotational system is obtained from the classical relation by substituting the quantum mechanical eigenvalues  $I(I + 1)\hbar^2$ , which correspond to the expectation value of the square of the rotational angular momentum [17]. Thus, we find that:

$$E(I) = \frac{1}{2}\mathcal{J}\omega^2 = \frac{(\mathcal{J}\omega)^2}{2\mathcal{J}} = \frac{I(I + 1)\hbar^2}{2\mathcal{J}} \quad (2)$$



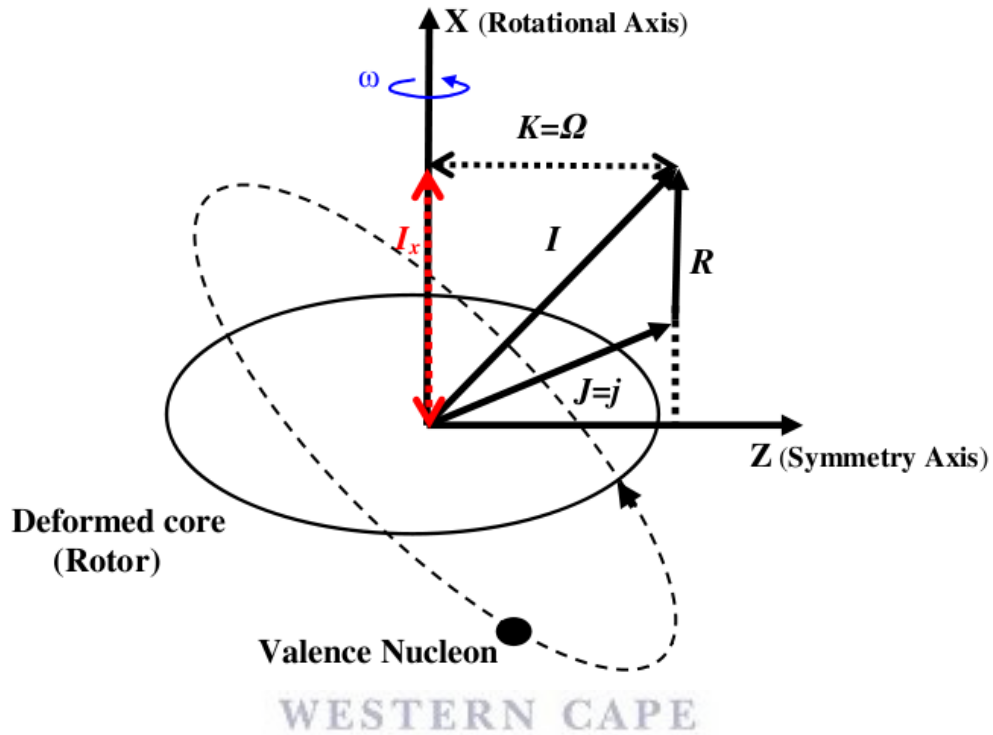


Figure 3: A schematic diagram showing a valence particle orbiting around a prolate deformed nucleus. This valence particle is also rotating about the x-axis with an angular velocity (rotational frequency)  $\omega$ . The angular momentum caused by the collective rotation of the core is denoted by  $\vec{R}$ , and it amounts to the total angular momentum  $\vec{I}$  of the system when it is summed with the angular momentum of the valence nucleon  $\vec{j}$  ( $= \vec{J}$ )  $\rightarrow \vec{j}$  for several valence nucleons. The projection of  $\vec{j}$  ( $= \vec{J}$ ) and  $\vec{I}$  onto the symmetry axis is  $\Omega$  ( $= \mathbf{K}$ , although,  $\mathbf{I}_x$  is the projection of  $\vec{I}$  onto the rotational axis [18]).

## 2.5 Vibrational States

The liquid drop model predicts that a nucleus will be spherical in its ground state. Any deformation of the shape from equilibrium increases the surface-energy term and, provided that  $Z$  is not too high, there will be a minimum in the graph of potential energy as a function of deformation. For small deformations near the minimum, the shape is parabolic, like the harmonic-oscillator potential. It is possible for the nucleus to vibrate about its equilibrium shape and exist in quantum states that can be obtained by solving the Schrödinger equation, using a suitable harmonic-oscillator potential. These states can be classified by considering the different vibrational modes of a liquid drop. Figure 4 is the schematic illustration of the lowest vibrational modes of a spherical system. In each case, the dashed line is the equilibrium and the solid line indicates an instantaneous view of the vibrating surface.

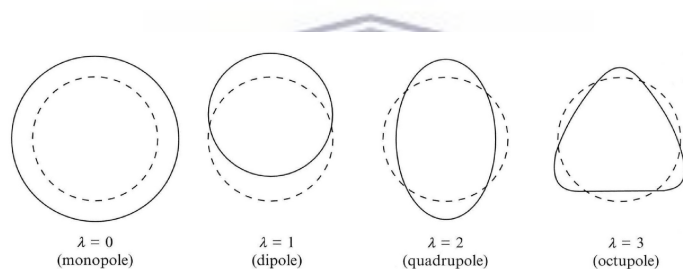


Figure 4: Schematic representation of the different vibrational modes of a liquid drop.

Any three-dimensional surface can be described by expressing the radius as sum of spherical harmonics:

$$R = R_0 \left[ 1 + \left( \sum_{\lambda=0}^{\infty} \right) \left( \sum_{m=-\lambda}^{\lambda} \alpha_{\lambda m}(t) Y_{\lambda}^m(\theta, \phi) \right) \right] \quad (3)$$

where  $\theta$  and  $\phi$  denote the angular co-ordinates of a point on the surface.  $R_0$  represents the radius of a sphere with the same volume as the nucleus. The  $\alpha_{\lambda m}(t)$  are amplitudes, which may be constant to describe a fixed shape or time dependent to describe a time-varying distribution such as a vibration. The expansion is in terms of multipoles, each represented by a spherical harmonic  $Y_{\lambda}^m(\theta, \phi)$ . The first four axially symmetric, vibrational modes about a spherical shape for the multipoles  $\lambda = 0$  to 3, are shown in Figure 4. Each mode has a characteristic frequency  $\omega\lambda$ , which depends on the amount of material in motion and the strength of restoring force. The energy is quantized in units of  $\hbar\omega\lambda$ . A single quantum of vibrational energy is called a phonon and its spin and parity are given by the spin and parity of the spherical harmonic, which are  $\lambda$  and  $(-1)^{\lambda}$  [17].

## 2.6 The Nilsson Model.

Over the years, the spherical shell model has proved to be valuable and has been successfully used to describe nuclear properties across the nuclear chart. However with the growing amount of nuclear data, experimental evidence of rotational bands and large quadrupole moments, indicated that the description of nuclei in terms of an independent single-particle motion in a spherical potential is inadequate. In a search for a model which could address such limitations the deformed shell model was introduced. The most commonly known model of this kind is the Nilsson model [19] that explains nuclear properties of deformed nuclei (such as the assignment of configurations to single-particle states in deformed nuclei), both prolate and oblate (see Figure 2) [15]. This model postulates a deformation dependent Hamiltonian, commonly referred to as Nilsson Hamiltonian:

$$H = \frac{p^2}{2m} + \frac{1}{2}m[\omega_x^2(x^2 + y^2) + \omega_z^2z^2] + Cl\vec{s} + Dl^2 \quad (4)$$

In the deformed potential constants,  $\omega_x$ ,  $\omega_y$  and  $\omega_z$  are the orthogonal oscillator frequencies in a three dimensional space. The third term is a consequence of the spin-orbit interaction. The last term  $l^2$  is a correction added to the Nilsson Hamiltonian to bring it in line with what is observed experimentally [20]. C and D are constants of proportionality and they are often explained in terms of other parameters. i.e.,  $\kappa = \frac{C}{2\hbar\omega_0}$  and  $\mu = \frac{2D}{C}$ . Equation 4 is used to determine the energies of the single-particle levels in non-spherical nuclei. The graphical representation of the Nilsson model is a plot of single-particle energies, in units of  $\hbar\omega_0$ , as a function of quadrupole deformation parameter  $\varepsilon_2$ . These diagrams, known as Nilsson diagrams are relevant to the present work and are shown in Figures 5 and 6 for protons and neutrons, respectively. This model has had a remarkable success in qualitatively accounting for most observed features of single-particle levels across the nuclear chart for deformed nuclei.

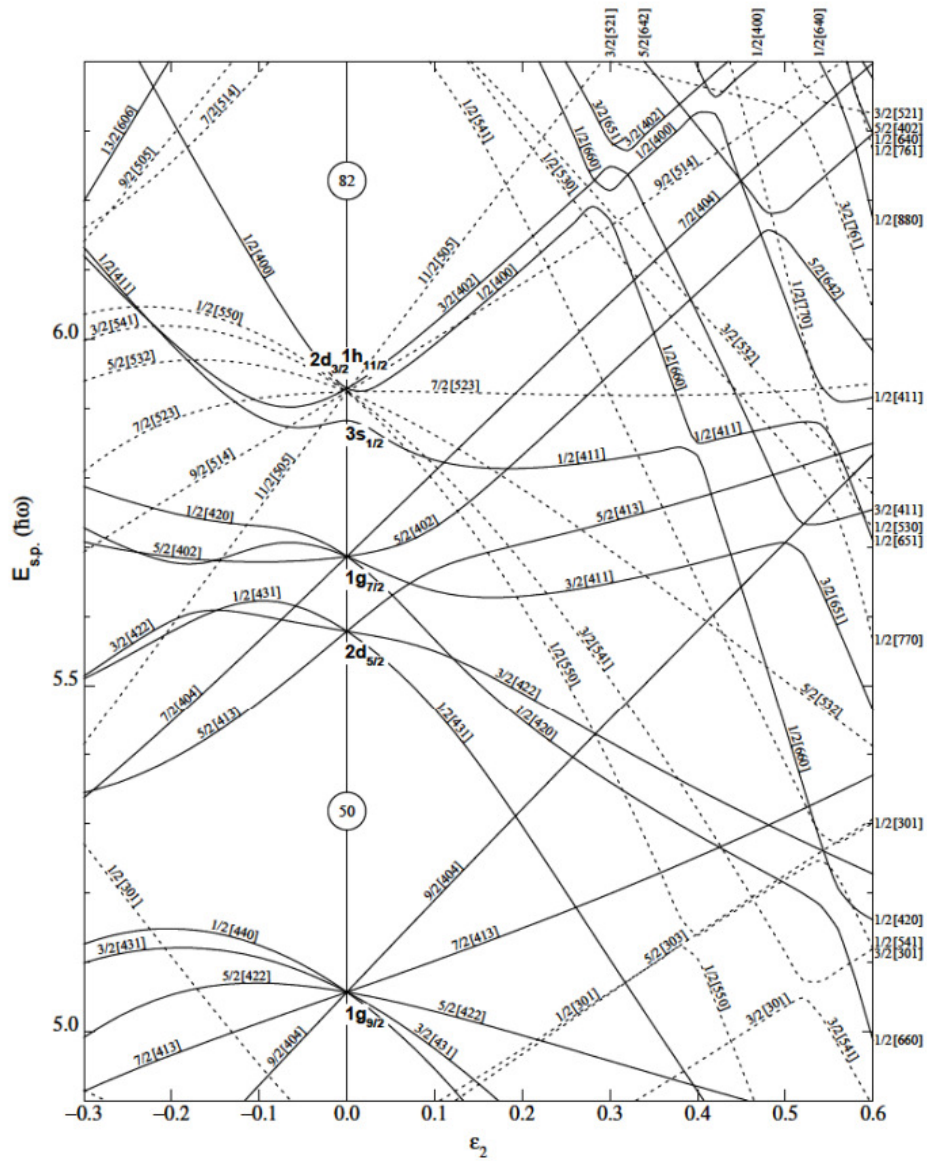


Figure 5: The Nilsson diagram for protons in the  $52 \leq Z \leq 82$  region, showing the single-particle energies as a function of the deformation parameter  $\varepsilon_2$ . The labelling convention is  $\Omega[Nn_z\Lambda]$ , where  $N$  is a major harmonic oscillator shell quantum number,  $n_z$  is the number of nodes in the wave-function in the  $z$  direction and  $\Lambda$  is the component of angular momentum along the symmetry axis or  $z$ -axis.  $\Omega = \Lambda + \Sigma$  is the projection of  $j = I + s$  onto the  $z$ -axis. Also positive-parity states is denoted by solid lines while dashed lines represent negative-parity states [21, 19].

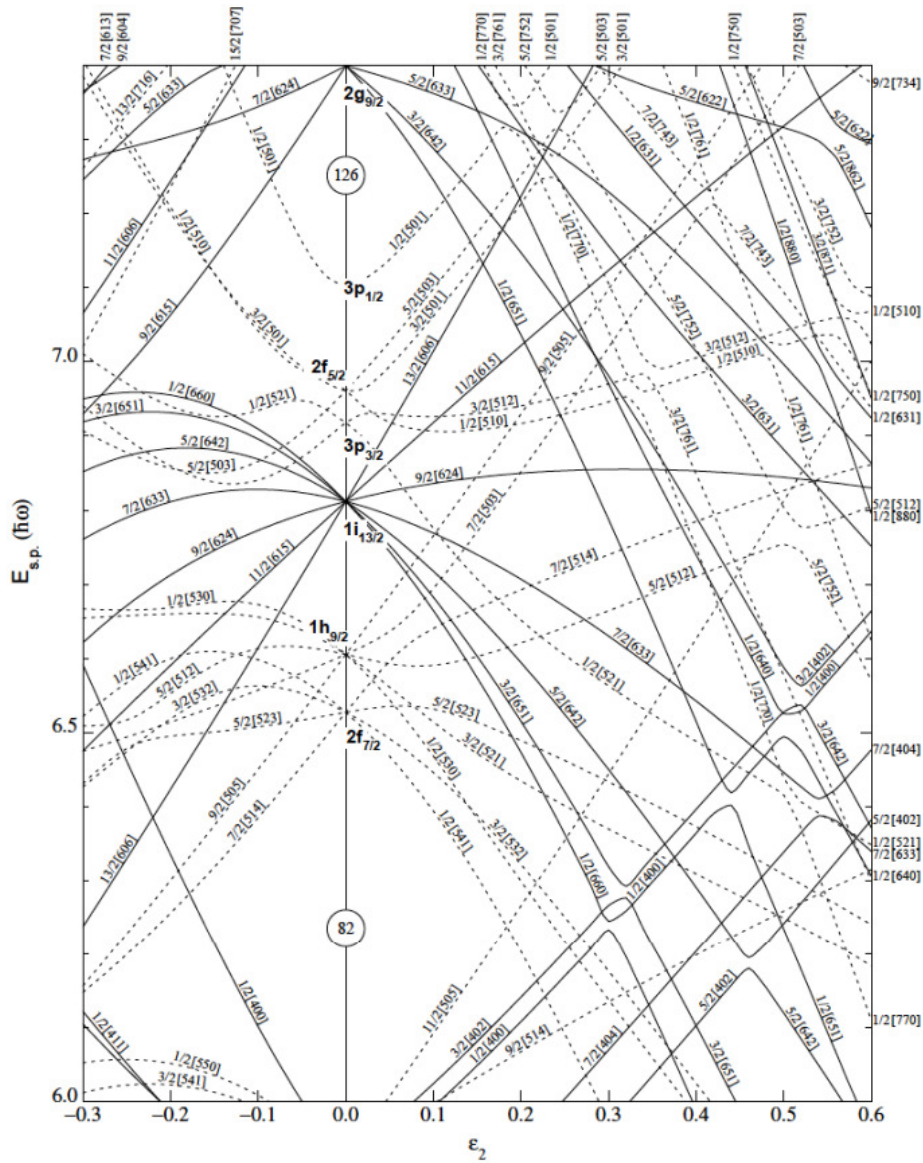


Figure 6: The Nilsson diagram for neutrons in the  $82 \leq Z \leq 126$  region, showing the single-particle energies as a function of the deformation parameter  $\epsilon_2$ . The labelling convention is  $\Omega[Nn_z\Lambda]$ , where  $N$  is a major harmonic oscillator shell quantum number,  $n_z$  is the number of nodes in the wave-function in the  $z$  direction and  $\Lambda$  is the component of angular momentum along the symmetry axis or  $z$ -axis.  $\Omega = \Lambda + \Sigma$  is the projection of  $j = l + s$  onto the  $z$ -axis. Also positive-parity states is denoted by solid lines while dashed lines represent negative-parity states [21, 19].

## 2.7 Single-particle and Collective Degrees of Freedom

In general, nuclear excitation may exhibit two extreme types of behaviour: (i) single-particle excitations of the individual valence nucleons to different single-particle levels, and (ii) collective modes of excitation involving a coherent motion of the nucleus as a whole. The collective model, as treated up to now [22], always deals with nuclei containing an even number of protons and neutrons. The next step of complication arises if one of those numbers is odd. i.e., if an additional nucleon is added to an even-even nuclear system. It must then be expected that excitations of both collective and single-particle character may be observed notwithstanding their interplay [7]. The interplay between the single-particle and collective excitation modes underlies an astounding diversity of experimental level schemes [23].



### 2.7.1 The Cranked Shell Model

The cranked shell model (CSM) was developed to assist in the limitations of Nilsson model. This arises from the non-spherical shape or the separation of the motion, around the nucleus, of an individual nucleon from rotations of the nucleus itself in space. In the past three to four decades, there came a time where modern experimental techniques revealed experimental observables associated with the interplay between collective core excitations, and single nucleon excitations, which were not easy to account for theoretically. This situation was resolved by the cranked shell model, which may be used to interpret the behaviour of nuclei at high-spin [24]. The first discussion of cranking (rotation) about an x-axis, perpendicular to the symmetry z-axis, was given by Inglis in 1954-1956 [25, 26], and was further developed by Bengtsson and Frauendorf in 1979 [27]. In this model, nucleons are treated as independent particles moving in an average potential, which is rotated externally with constant angular velocity  $\omega$  about a fixed axis. This rotation exerts an additional force(s) on the nuclear system (coriolis and centrifugal) and thus, an extra term must be added to the Hamiltonian to account for these. In the laboratory frame the system may be described by the time-dependent single-particle Schrödinger equation [28]:

$$i\hbar \frac{\partial \psi_{lab}}{\partial t} = h_{lab} \psi_{lab}, \quad (5)$$

where  $h_{lab}$  and  $\psi_{lab}$  are the single-particle Hamiltonian and wavefunction of the system in the laboratory frame, respectively. The rotation of the average field, which is not symmetric with respect to the rotational axis, introduces the time dependence to the Schrödinger equation. This may, however, be reduced to stationary equation of motion when the laboratory frame is transformed into the rotating frame (intrinsic frame, or else known as, the body-fixed frame). The transformation is achieved by means of the unitary rotation operator  $R(t)$ :

$$R(t) = \frac{e^{-i\omega t j_x}}{\hbar} \quad (6)$$

where  $\vec{j}_x$  is the total angular momentum operator along the rotational x-axis, for a single-particle. The single-particle Hamiltonian is found to be:

$$h_{Rot.} = \hat{h}_{lab} - \omega \vec{j}_x, \quad (7)$$

where  $h_{Rot.}$  is the single-particle Hamiltonian in the rotating system, referred to as the cranking Hamiltonian or Routhian. The term  $-\omega \vec{j}_x$  contains the coriolis and centrifugal contributions, due to the non-inertial system of the rotating frame, which modify the

nucleon orbitals. The eigenvalues of this Hamiltonian are known as Routhians. The total cranking Hamiltonian  $H_{Rot.}$  can be obtained from the sum of all the single-particle cranking Hamiltonians of equation above:

$$H_{Rot.} = \sum_{i=1}^A h_{Rot.} = H_{lab} - \omega \vec{J}_x, \quad (8)$$

$$\vec{J}_x = \sum_{i=1}^A \vec{j}_x.$$

The theory can therefore describe both single-particle, as well as collective effects (see Figure 7 [29]). At this frequency the coriolis force has sufficient energy to break a pair of nucleons with angular momentum  $j$  in magnetic substates  $m$  and  $-m$ . The nucleons can then align to have a total spin  $J = m + m(-1)$ . For  $i_{13/2}$  neutrons, the situation in this work,  $J = 13/2 + 11/2 = 12$ . This alignment is the cause of the experimentally observed “back bending” of rotational bands in nuclei. This model has had a remarkable success in providing a microscopic description of collective rotational bands in deformed and superdeformed nuclei [27].

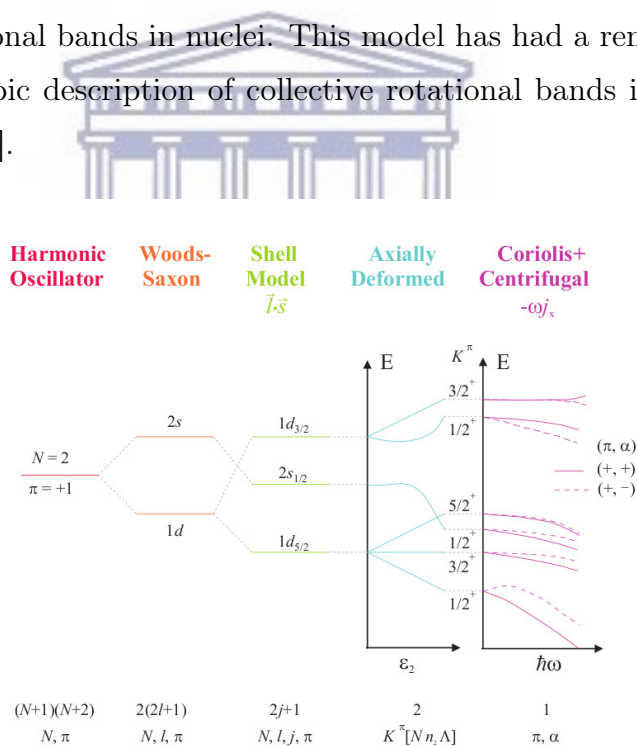


Figure 7: Illustration of the labelling of orbitals in various models and the salient features implied by the cranking term, for the s-d shell orbits. This diagram also shows how some levels have a very strong dependence on the rotational frequency  $\omega$ , these are orbits corresponding to large  $j$  and small  $K$  values. The signatures  $\alpha = +$  and  $\alpha = -$  correspond to  $\alpha = +1/2$  and  $\alpha = -1/2$ , respectively [27].



## 2.8 Interaction of Radiation with Matter

Gamma-rays were identified in 1900 by Becquerel and Villard as a component of the radiation from uranium that had much higher penetrability than alpha and beta particles [31]. The term radiation applies to the emission and propagation of energy through space or material. Detection of gamma-rays is possible as a result of their interaction with the detector material. Although there are many ways in which gamma-rays can interact with matter, there are three major interaction mechanisms that play an important role in radiation measurements namely: photoelectric absorption, Compton scattering and pair production. All these processes lead to the partial or complete transfer of gamma-ray energy to electron [32]. The regions of dominance of these three photon interaction mechanisms as a function of photon energy and atomic number of the absorbing material are shown in Figure 8 [33].

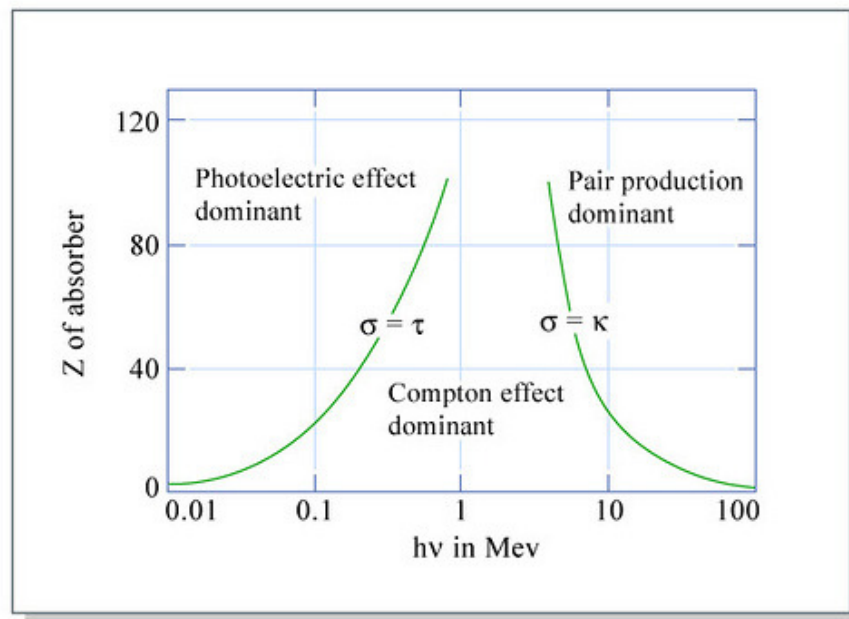


Figure 8: Relative importance of the three photon interaction mechanisms and their energy regions of dominance [33].

### 2.8.1 Photoelectric Absorption

In the process of photoelectric absorption, a photon undergoes an interaction with a bound atomic electron in which the photon energy is completely absorbed. Subsequently the energetic photoelectron is ejected from the atom from one of its bound shells. The interaction is with the atom as a whole and cannot take place with free electrons [32]. For gamma-rays of sufficient energy, the most probable origin of this process is the most tightly bound or K shell of the atom for gamma-rays of sufficient energy. The photoelectron appears with an energy given by:

$$E_e = h\nu - E_b \quad (9)$$

where  $E_b$  denotes the binding energy of the photoelectron in its original shell. For gamma-ray energies of more than a few hundred keV, the photoelectron carries off the majority of the original photon energy [32]. This process is the predominant mode of interaction for gamma-rays of relatively low energy. It is also important for gamma-ray detection because the gamma-ray gives up all its energy, and the resulting pulse falls in the full-energy peak. Figure 9 is the schematic representation of the photoelectric absorption [34]. The process is also enhanced for absorber materials of high atomic number  $Z$ . No single analytic expression is valid for the probability of photoelectric absorption per atom over all ranges of  $E_\gamma$  and  $Z$ , but a rough approximation is given by [32]:

$$\tau \cong \text{constant} \times \frac{Z^n}{E^{3.5}} \quad (10)$$

where the exponent  $n$  varies between 4 and 5 over the gamma-ray energy region of interest.

### 2.8.2 Compton Scattering

The interaction of Compton scattering takes place between the incident gamma-ray photon and an electron in the absorbing material. In Compton scattering, the incoming gamma-ray photon is deflected through an angle  $\theta$  with respect to its original direction [32]. The photon interacts with an electron and is scattered, losing a portion of its energy to the electron (assumed to be initially at rest), which is then known as a recoil electron.

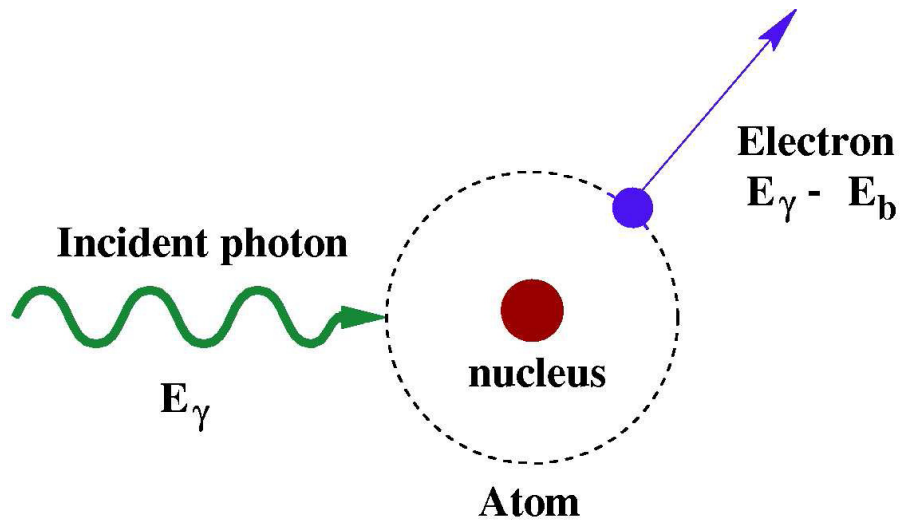


Figure 9: Schematic of the mechanism of the photoelectric absorption process.

Because all angles of scattering are possible, the energy transferred to electron can vary from zero to large fraction of the gamma-ray energy. The expression that relates the energy transfer and the scattering angle for any given interaction can simply be derived by writing simultaneous equations for the conservation of energy and momentum [32]. Using the symbols defined in the sketch of Figure 10, we can show that:

$$\frac{1}{E'_\gamma} - \frac{1}{E_\gamma} = \frac{1}{m_0 C^2} (1 - \cos\theta) \quad (11)$$

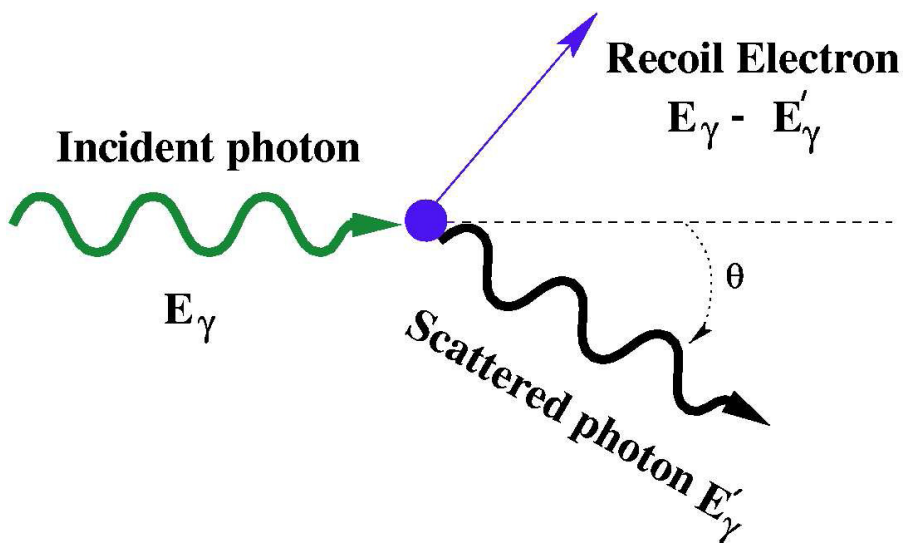


Figure 10: Schematic of the mechanism of the Compton Scattering process.

where  $m_0C^2$  is the electron rest mass energy,  $E'_\gamma$  is related to the incident gamma-ray energy and the energies are in keV. For small scattering angles  $\theta$ , very little energy is transferred. Some of the original energy is always retained by the incident photon, even in the extreme situations such as  $\theta = \pi$ . The probability of Compton scattering per atom of the absorber depends on the number of electrons available. The angular distribution of the scattered gamma-ray is predicted by the Klein-Nishina formula for the differential scattering cross section [32]  $\frac{d\sigma}{d\Omega}$ :

$$\frac{d\sigma}{d\Omega} = Z(r_0)^2 \left( \frac{1}{1 + \alpha(1 - \cos\theta)} \right)^2 \left( \frac{1 + \cos^2\theta}{2} \right) \left( 1 + \frac{\alpha^2(1 - \cos\theta)^2}{1 + \cos^2\theta[1 + \alpha(1 - \cos\theta)]} \right) \quad (12)$$

where  $\alpha$  is fine structure constant and  $r_0$  is the classical electron radius. Figure 11 illustrates the strong tendency for forward scattering at high values of the gamma-ray energy.

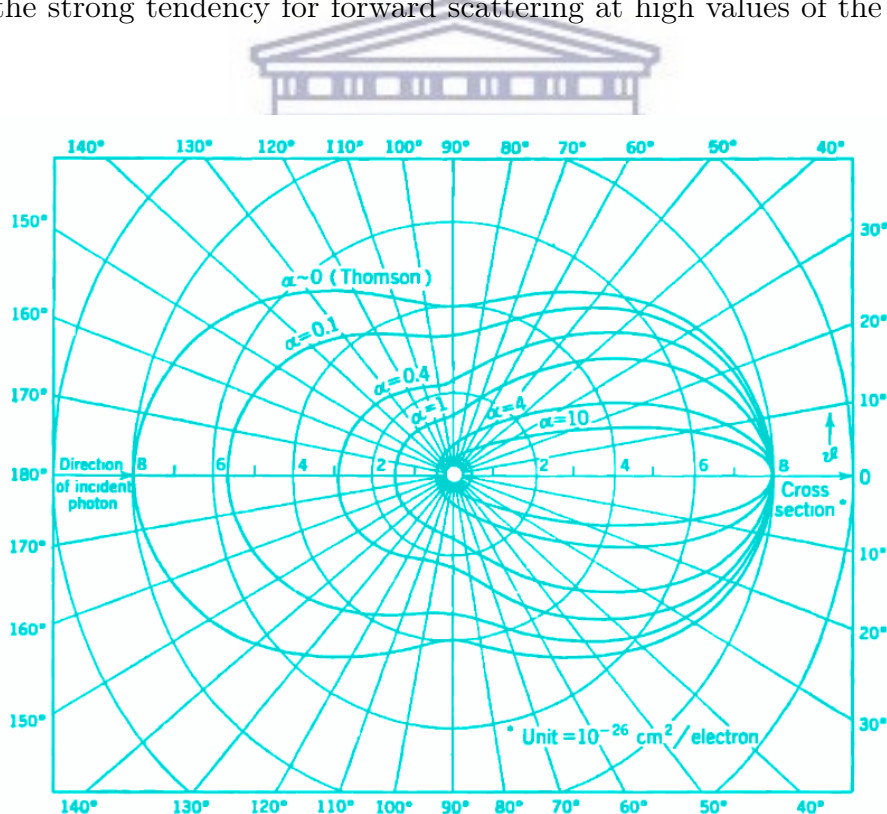


Figure 11: A polar plot of the Klein-Nishina formula [33].

### 2.8.3 Pair Production

The process of pair production involves the transformation of a photon into an electron-positron pair. A gamma-ray with an energy of at least 1.022 MeV can create an electron-positron pair when its under the influence of the strong electromagnetic field in the vicinity of the nucleus (see Figure 12) [32]. In this interaction the nucleus receives a very small amount of recoil energy to conserve momentum, but the nucleus is otherwise unchanged and the gamma-ray disappears. This interaction has a threshold of 1.022 MeV because that is the minimum energy required to create the electron and positron. But if the gamma-ray energy exceeds twice the rest-mass energy of an electron (1.022 MeV), the process of pair production is energetically possible. No simple expression exists for the probability of pair production per nucleus, but its magnitude varies approximately as the square of the absorber atomic number [32]. The schematic representation of pair production process is shown in Figure 12.

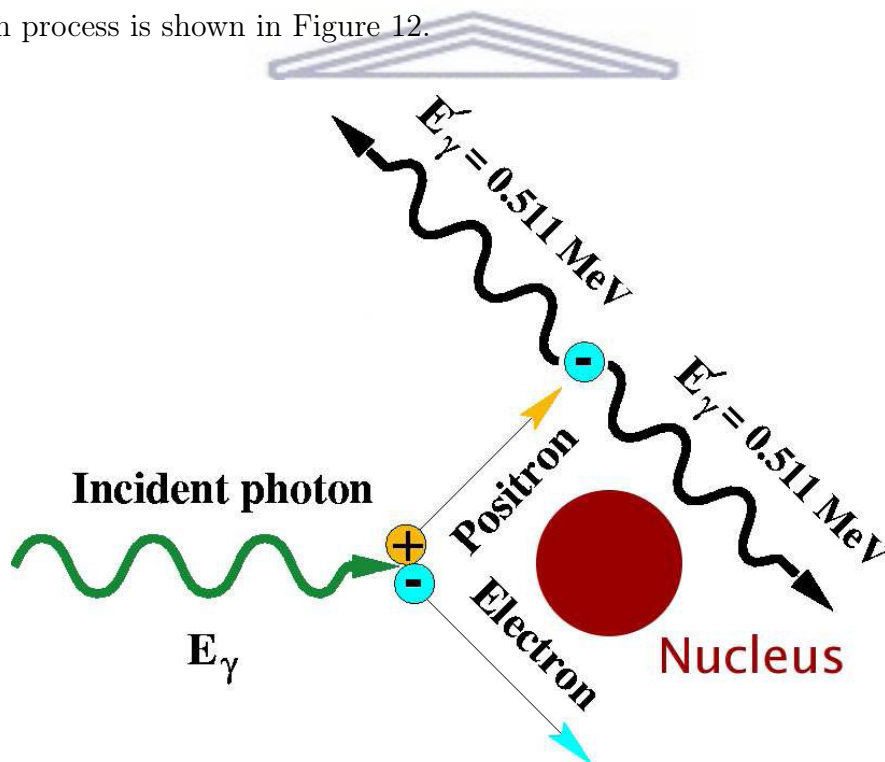


Figure 12: Schematic of the mechanism of the pair production-annihilation process.

## Chapter 3

# 3 Experimental Methods

## 3.1 Reaction Choice

In this experiment we used the Projected Angular momentum Coupled Evaporation (PACE4) [30] simulation to determine the optimal energy for the beam used in our Heavy-Ion Fusion Evaporation (HIFE) reaction. PACE4 employs a Monte Carlo simulation to calculate predicted cross-section and angular momentum for the reaction of interest. The choice of a thicker target is of interest since it leads to achieving high statistics in the experiment. Thicker targets increase the number of interactions between the beam and target particles leading to a higher event rate, and thus better statistics. On the other hand, if the target is very thin the recoils into vacuum will have the full Doppler shift giving narrow peaks, and good resolution, but the event rate decreases for a given beam current. Figure 13 shows a PACE4 plot representing yields (in percentage %) versus beam energy for different channels. The energy of 93 MeV was chosen, as indicated by the dotted vertical line, which maximizes the angular momentum in  $^{163}\text{Yb}$  that was produced.

The fusion evaporation reaction  $^{152}\text{Sm}(^{16}\text{O},5n)^{163}\text{Yb}$  has been used to search for structures where an odd neutron couples to core excitations of  $^{162}\text{Yb}$ . Heavy fusion-evaporation has the ability to give the most efficient way to reach high-spin states in these rare earth nuclei [36]. The  $^{16}\text{O}$  beam was delivered by the  $K = 200$  separated sector cyclotron at iThemba LABS (Cape Town) and used to bombard the  $^{152}\text{Sm}$  target. The energy of  $^{16}\text{O}$  beam was chosen in order to enhance the production of  $^{163}\text{Yb}$ . The target was a metallic  $^{152}\text{Sm}$  ( $\sim 98.27\%$ ) foil with a thickness of  $5 \text{ mg/cm}^2$  to ensure that the recoiling nuclei stopped in the target.  $0.5 \text{ mm}$  copper absorbers were used in front of the gamma-ray detector to reduce the detection of x-rays. The number of gamma-gamma coincidences in this experiment was  $2.5 \times 10^9$  events, allowing different rotational bands of the nucleus to be identified.

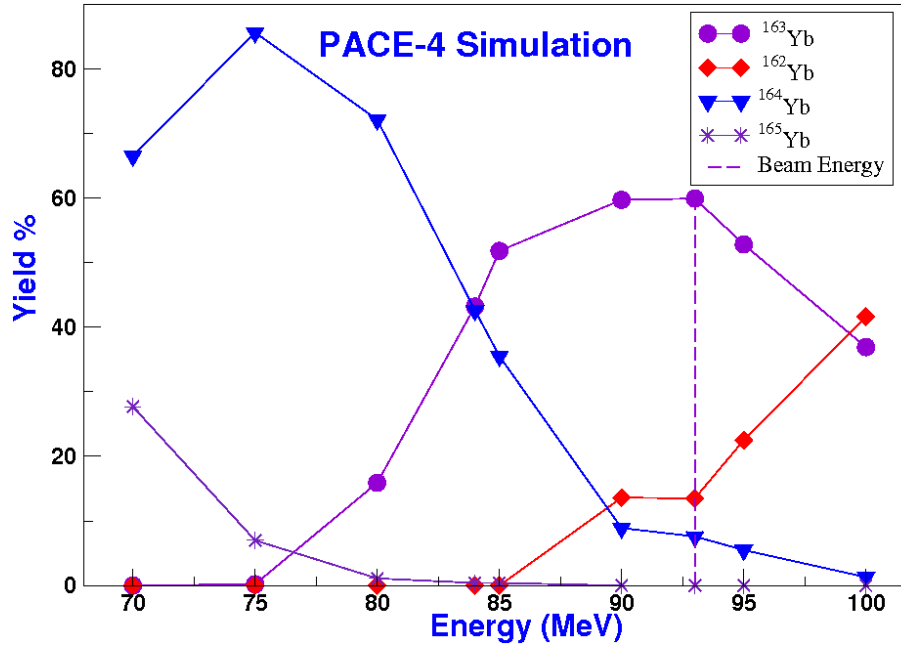


Figure 13: PACE4 simulation of the residual nucleus yield (in percentage %) as a function of  $^{16}\text{O}$  bombarding energy of a  $^{152}\text{Sm}$  target.

### 3.2 Heavy-Ion Fusion Evaporation (HIFE)

Fusion evaporation reaction is a commonly method used to study excited states of neutron deficient nuclei [36]. In the present work, this reaction was used to populate the excited nucleus. It was done by fusing the  $^{16}\text{O}$  beam with a  $^{152}\text{Sm}$  target which resulted in the formation of a very excited unstable compound nucleus  $^{168}\text{Yb}$ . The excited nucleus evaporates five (statistical evaporation) neutrons until less excited  $^{163}\text{Yb}$  remains. Each evaporation neutron takes about 10 MeV away from the very excited  $^{168}\text{Yb}$  compound nucleus. This residual nucleus ( $^{163}\text{Yb}$ ) eventually loses its energy and angular momentum by emitting gamma-rays. The corresponding electromagnetic transitions connect different excited states in the nucleus with each other all the way to the ground state. Their properties provide detailed information about the internal structure of the nucleus. It takes 8 MeV to separate a neutron from the compound nucleus, it also needs an extra 2 MeV on average, to give it enough kinetic energy to access a big enough phase space to increase the probability of emission [37]. In order for a fusion reaction to occur, the projectile kinetic energy (beam energy) must be greater than the Coulomb repulsion energy due to the repulsive charges on the projectile and target. The Coulomb barrier that needs to be overcome is given approximately by:

$$E_c = \frac{1.44Z_1Z_2}{1.16(A_1^{\frac{1}{3}} + A_2^{\frac{1}{3}} + 2)} \quad (13)$$

where  $Z_1$  and  $Z_2$  denote the beam and target atomic numbers respectively,  $A_1$  and  $A_2$  refer to the beam and target mass numbers respectively [37]. Figure 14 is the representation of how several different channels can be populated, due to emission of different number of nucleons.

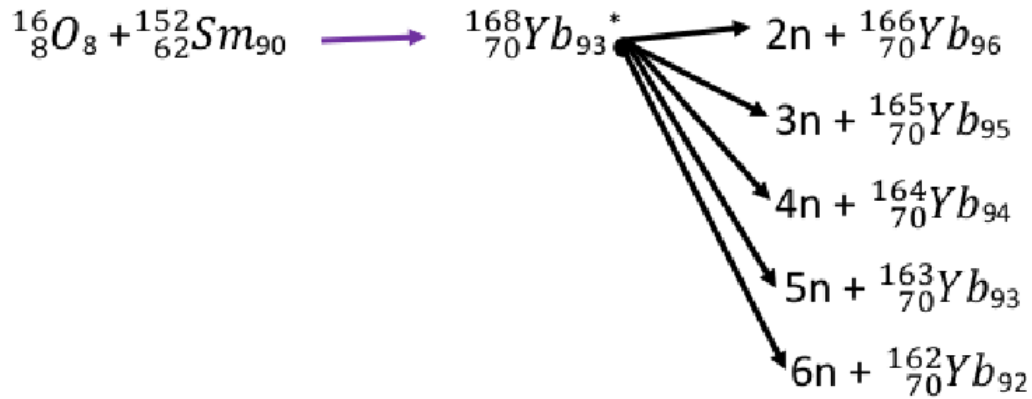


Figure 14: Simple demonstration of how different residual nuclei are populated due to exit channels. Each exit channel is associated to its specific cross section, which indicates the probability for the nuclear reaction to proceed through it [38].

The schematic representation of heavy-ion fusion evaporation is shown in Figure 15.



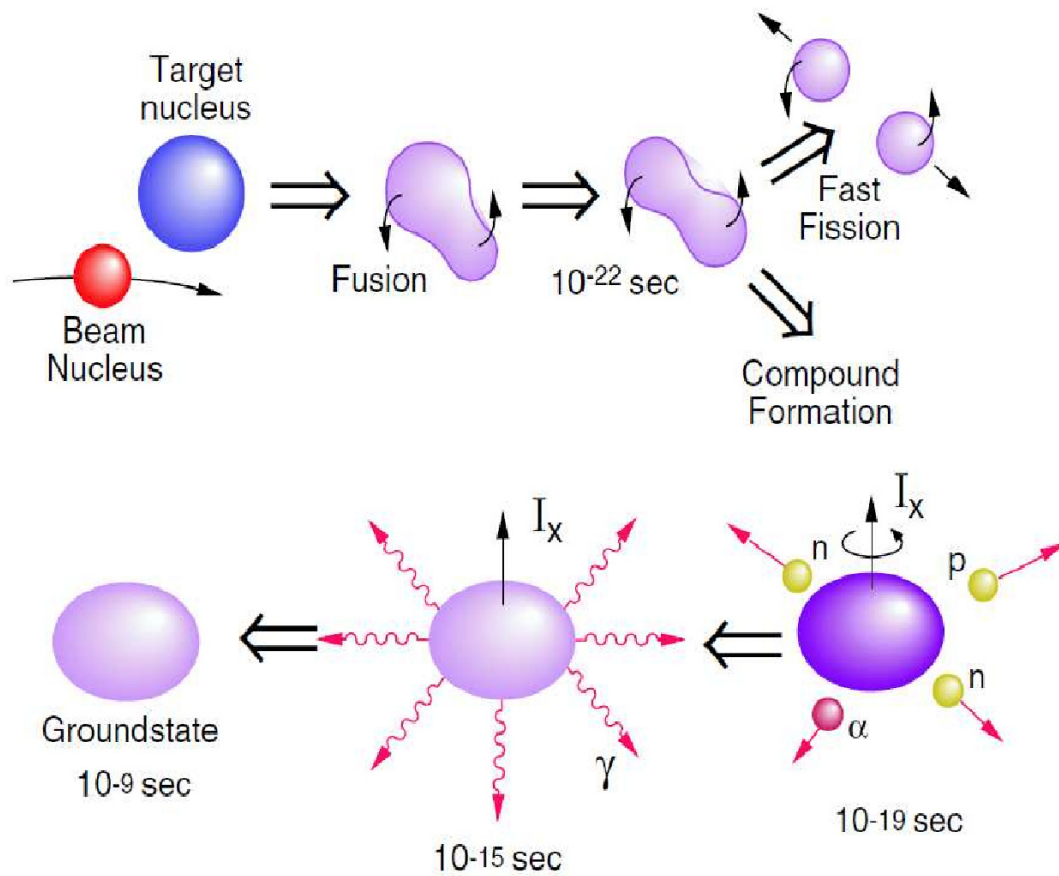


Figure 15: A diagram of the heavy-ion fusion evaporation process, along with a time scale. An accelerated projectile nucleus collides and fuses with a target nucleus forming a compound system. The compound system first cools by evaporation of neutrons, protons and /or alpha particles. It then loses the rest of its excitation energy and almost all of its initial angular momentum by the emission of gamma rays. The total decay process is completed very quickly, in about  $10^{-9}$  seconds [39].

## 3.3 Detection of Gamma Radiation

### 3.3.1 Semiconductor Detectors

A nucleus may emit radiation in the form of gamma-rays, when it de-excites. The emitted gamma-rays contain information on the structure of the nucleus [23]. In order to obtain the information contained on the structure of the nucleus, we have to use the detectors to detect those gamma-rays. Semiconductor detectors are one of the detectors used in gamma-ray spectroscopy. Semiconductor detectors are essentially solid-state ionization chambers with the electron-hole pairs playing the role of electron-ion pairs in gas detectors. These detectors operate through the promotion of electrons from the valence band to the conduction band. Semiconductor detectors are preferably used for gamma-ray spectroscopy because they have good energy resolution. The incident gamma-ray photon produces electron-hole pairs which can be collected by the application of a voltage across the detector material. The preferred semiconductor is one with a lower band-gap and a low level of impurities. Silicon and germanium are the two ideal candidates, of semiconductor detectors, because they have higher atomic numbers, which provides a high absorption coefficient for the incident gamma radiation.

### 3.3.2 High-Purity Germanium (HPGe) Detectors

Germanium (Ge) detectors belong to a class of semiconductor detectors known for their superior energy resolution as compared to scintillation detectors [32]. These detectors are mainly used for gamma-ray detection. A gamma-ray entering the active part of a Ge semiconductor detector interacts through the three absorption processes, described in the previous sections, to create electron hole pairs. The average energy required to create such pairs (e-h pairs) is about 3.6 eV for silicon (Si) and 3 eV for germanium [17]. Germanium detectors are the preferred detectors for gamma-ray spectroscopy because they possess a high atomic number ( $Z = 32$ ), which favours the photoelectric effect compared to silicon that has ( $Z = 14$ ). The Ge detector is essentially a reverse biased p-n junction. At the junction between the p-type and n-type material, the migration of electrons from the n-type material and holes from the p-type material results in the formation of a region of net zero charge. This region is known as the depletion region, a region devoid of any mobile charge carriers [23]. Most Ge detectors used in Gamma-ray spectroscopy are coaxial n-type, as shown in Figure 16 [29].

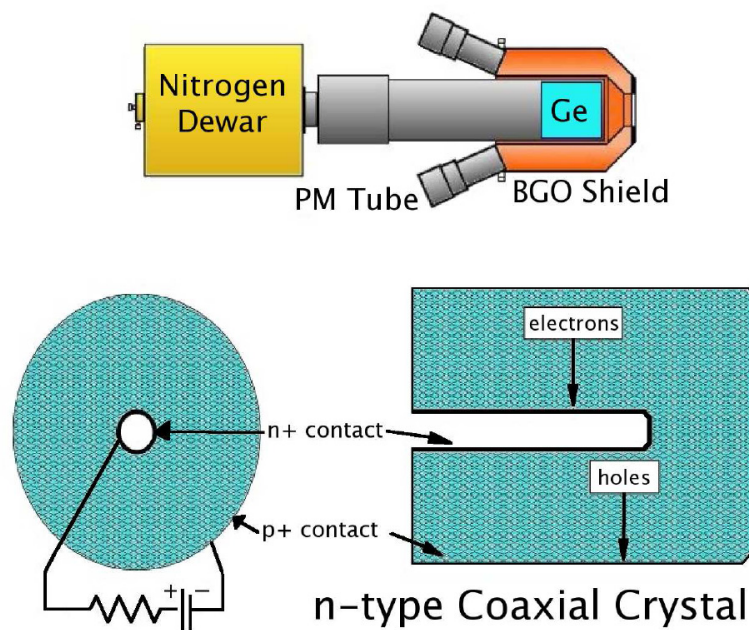


Figure 16: Illustration of a typical coaxial n-type HPGe detector and its crystal [29].

### 3.3.3 Clover Detectors

25 years ago detector developments have been made that enable high efficiency detectors to be made which maintain excellent spectrum quality, and clover detectors are one of those detectors [30]. The first clover detector was initially developed in France by Canberra in the frame of the EUROGAM collaboration. A clover detector (composite detector) is a gamma-ray detector consisting of four coaxial n-type high purity germanium (Ge) crystals each modelled and mounted in an ordinary cryostat to form a structure which looks like a four-leaf clover, and are the first composite detector to be used in a large array [40]. These detectors give 2.6 keV with  $3\mu\text{s}$  ( $^{152}\text{Eu}$ ) for energy resolution and timing performances and in add back mode the clover efficiency at 1332 keV is 32% higher than the combined efficiency of the individual elements. Each clover detector is surrounded by a bismuth germanate (BGO) Compton suppression shield. By mounting four smaller crystals in an ordinary cryostat a detector of a given volume can be formed at a reduced cost, since large volume high purity single crystals of Ge are more expensive. The individual smaller Ge crystals present a smaller solid angle than large volume Ge detector, thus significantly reducing the effects of Doppler broadening on the resulting spectra. Clover detectors can also be used to measure the linear polarization of the gamma-rays in order to determine the electric or magnetic nature of the incident photons [41].

Figure 17 shows a schematic representation of clover germanium detector.

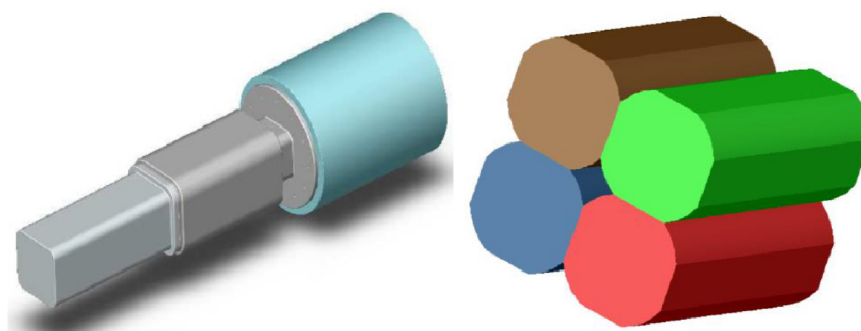


Figure 17: A picture of Clover detector that can fit into a BGO shield with its cylindrical liquid nitrogen dewar and the crystal arrangement of a 4 segment Clover detector [30].

### 3.3.4 Compton Suppression Spectrometer

In gamma-ray spectrometry performed with HPGe detectors, the detection of low intensity gamma-ray lines is complicated by the presence of Compton scattered gamma-rays of high energy escaping from the detector. The development of the Compton suppression spectrometer (CSS), which reduces the noise content from escaping Compton scattered photons to the gamma energy spectrum have been developed. These CSSes consist of a primary HPGe detector (see Figure 18) and surrounding secondary detector with appropriate data acquisition and processing electronics.

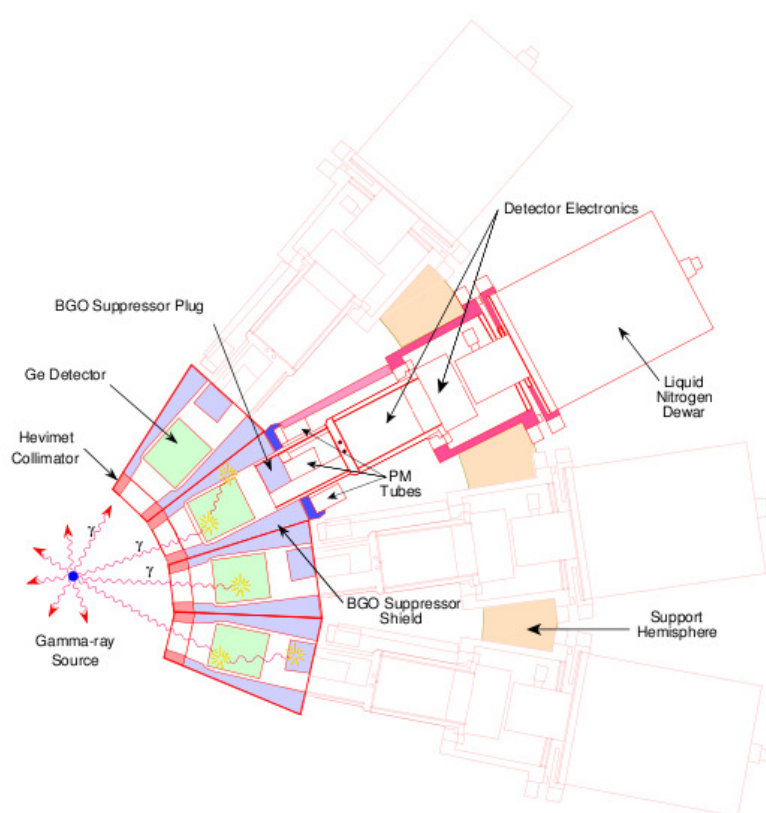


Figure 18: Schematic of a Compton suppressed spectrometer (CSS) made up of several collimated HPGe detectors axially surrounded by BGO shields [29].

For instance if the a gamma-ray is detected in both the Ge detector and the secondary detector within specific time frame, then it is interpreted as scattering event (or an unwanted event) and is not written to the tape. Due to the requirement of good timing properties and cost considerations, the secondary detector is typically a scintillation detector. The most common scintillation material for this application is bismuth germanate ( $Bi_4Ge_3O_{12}$ ), abbreviated as BGO [35]. The goal of Compton suppression is to improve

the quality of the data by reducing the number of partial energy events in the spectrum. A Compton suppressed Ge detector typically has a peak-to-total ratio of about 60%. A spectrum showing a  $^{60}\text{Co}$  source for both suppressed and unsuppressed Ge detector is illustrated in Figure 19 [35]. The P/T is the sum of the counts in the 1173 and 1332 keV peaks in  $^{60}\text{Co}$  divided by the total number of counts above a chosen minimum.

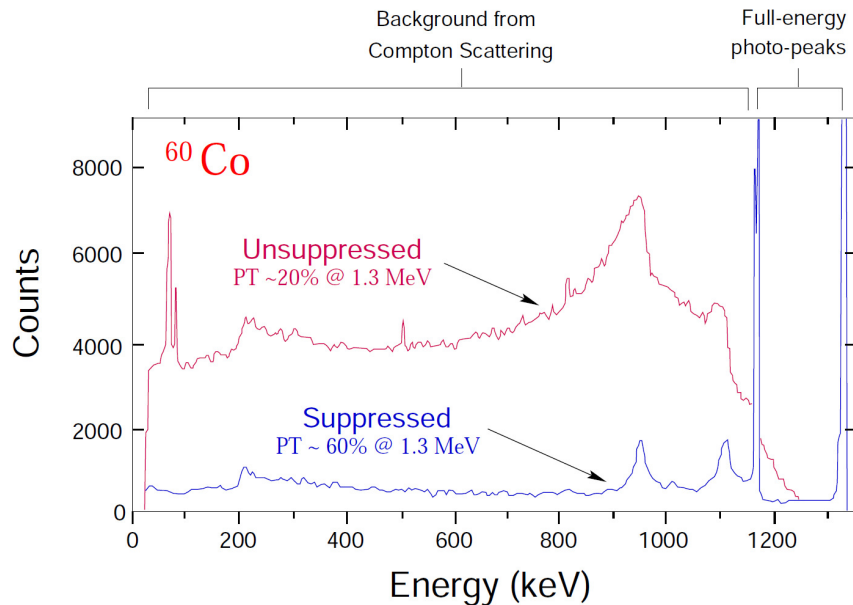


Figure 19: Spectra from a  $^{60}\text{Co}$  source showing the dramatic difference in the P/T ratio with the employment of Compton Suppression. The Compton suppressed Ge detector has a P/T ratio of about 60% and unsuppressed Ge detector has a P/T ratio of about 20%. This means that 80% of the events collected are background in the unsuppressed case [35].

### 3.3.5 The AFRODITE array

AFRODITE is an acronym derived from AFRican Omnipurpose Detector for Innovative Techniques and Experiments. The AFRODITE array at iThemba LABS (Cape Town) is mounted in a rhombicuboctahedron frame with 16 detector positions. The array normally consists of nine HPGe clover detector and seven low energy photon spectrometer (LEPS), where these detectors are positioned at angles of  $45^\circ$ ,  $90^\circ$  and  $135^\circ$  with respect to the beam direction. Only 8 clover detectors were used in the current work, 4 positioned at  $90^\circ$  and 4 positioned at  $135^\circ$ . These detectors were mounted around the target chamber so that they can detect gamma-rays from the fusion evaporation reaction. Inside the target chamber there is a target ladder which is used to control the position of the target; this is done by moving the target ladder vertically. The target ladder consists of three slots, first two slots were respectively used as an empty frame and a ruby for beam focusing. The third slot was used for mounting the  $^{152}\text{Sm}$  target. Figure 20 is a photograph showing HPGe clover detectors in the AFRODITE array.

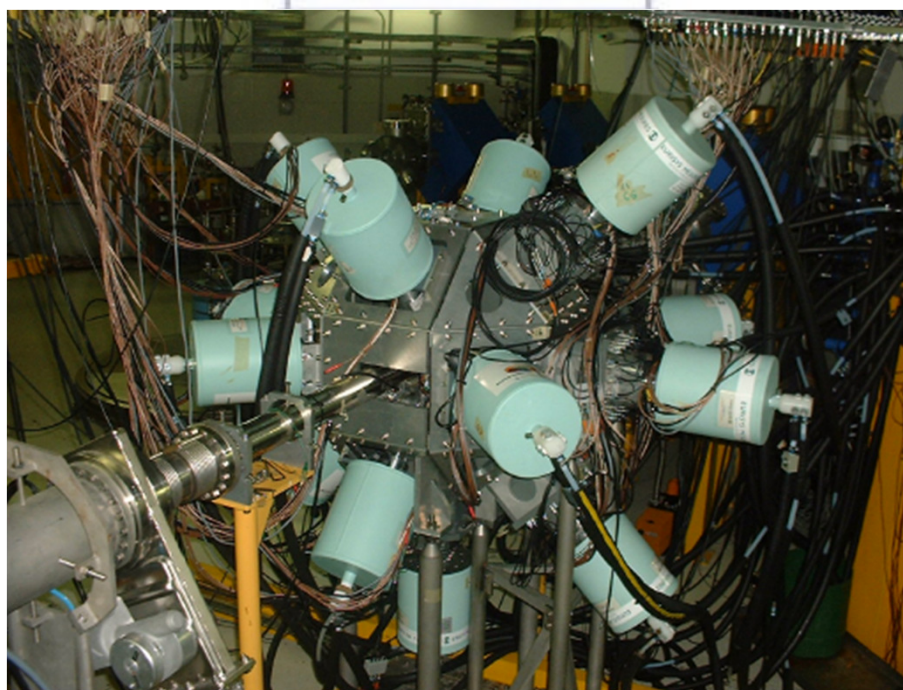


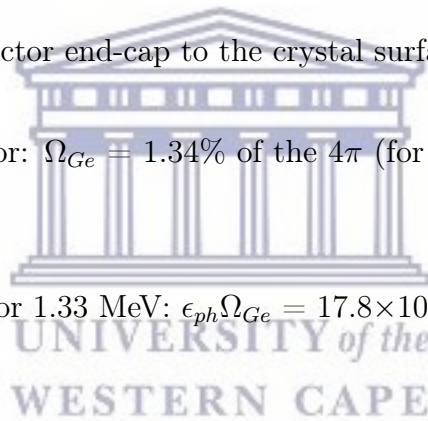
Figure 20: Photo showing HPGe clover detectors in BGO escaped suppressed shield in the AFRODITE array.

In order for a gamma-ray to be detected, it must interact with matter, that interaction must be recorded. Fortunately, the electromagnetic nature of gamma-ray photons allows them to interact strongly with the charged electrons in the atoms of all matter. The key

process by which a gamma-ray is detected is ionization, where it gives up part or all of its energy to an electron as described in section 3.2. Many different detectors have been used to register the gamma-ray and its energy.

### Specification of clover detectors [30] in the AFRODITE array

- Peak-to-total ratio for 1.33 MeV:  $(P/T)_{Ge} = 0.30$
- Add-back factor for 1.33 MeV: 1.56
- Total opening angle:  $\theta = 23.2^\circ$
- Distance from the crystal surface to the target centre:  $D_{tc} = 196$  mm
- Distance from the detector end-cap to the crystal surface:  $D_{ec} = 2.0$  mm
- Solid angle per detector:  $\Omega_{Ge} = 1.34\%$  of the  $4\pi$  (for a 0.2 mm distance between crystals)
- photo-peak efficiency for 1.33 MeV:  $\epsilon_{ph}\Omega_{Ge} = 17.8 \times 10^{-4}$





## 3.4 Correlations of gamma transitions

### 3.4.1 Angular Distribution and Correlation of gamma-rays

The measurements of the angular distributions, angular correlations and polarizations of the gamma-ray transitions are performed in order to determine the multipolarity of the gamma-transitions, and the relative spins and parities of excited nuclear states formed in fusion-evaporation reactions. In fusion-evaporation reactions the compound nucleus is formed in a state so that its angular momentum vector ( $\tilde{\mathbf{I}} = \tilde{\mathbf{r}} \times \tilde{\mathbf{p}}$ ) is perpendicular to the axis defined by the direction of the beam, as shown in Figure 21. This aligns the spin of the residual nuclei so that the magnetic quantum number, with respect to the beam direction,  $m \approx 0$ . The subsequent evaporation of particles causes some smearing of the

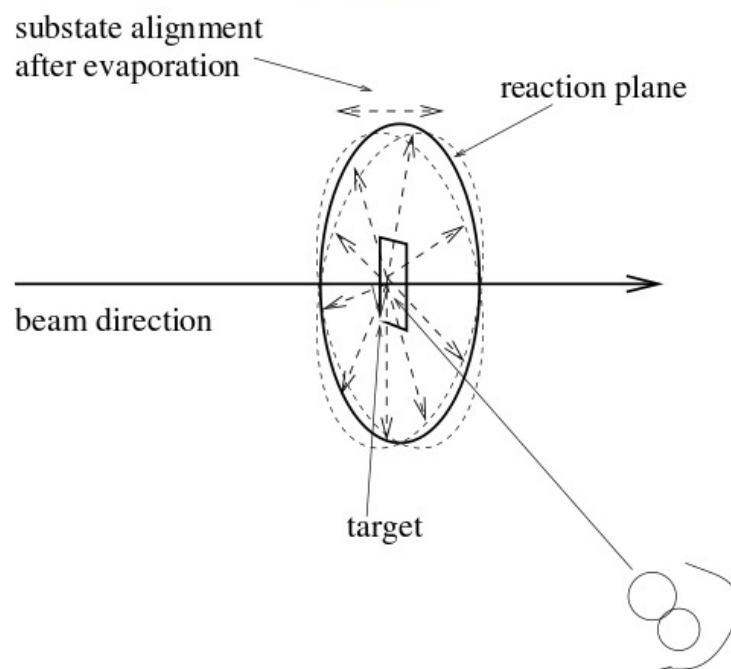


Figure 21: Schematic of initial orientation in fusion-evaporation reactions [42].

direction of the alignment, but even so the nucleus retains a high degree of alignment for times of the order of nanoseconds. When a nucleus in such a state emits gamma-radiation, the relative intensities at different angles with respect to the beam axis depend on the multipolarity of the transition [43].

### 3.4.2 Angular Distribution

The angular distribution of gamma-rays,  $W(\theta)$ , is the relative probability that a photon will be emitted at an angle  $\theta$  with respect to the beam direction. In order to have an angular distribution, oriented nuclear states are required. Oriented means that the population of the  $m$  substates depends only on the magnitude of  $m$ , and not on its sign. The general formula for the angular distribution function is given by:

$$W(\theta) = \sum_k A_k P_k(\cos\theta) \quad (14)$$

where  $W(\theta)$  is the gamma-ray intensity measured at angle  $\theta$  with respect to the beam direction,  $P_k(\cos\theta)$  are the standard Legendre polynomials, and  $A_k$  is the angular distribution coefficient. The  $A_k$  value depends on the substate or  $m$ -population distribution and the values of the initial and final state spins [44]. For pure dipole  $\Delta\mathbf{I} = 1$  transition (E1 or M1), the angular distribution will be given by:

$$W(\theta) = A_0[1 + A_2 P_2(\cos\theta)] \quad (15)$$

where  $P_2(\cos\theta) = \frac{1}{2}(3\cos^2\theta - 1)$  and  $A_0$  is the true intensity of the gamma-ray. For this type of transition  $A_2$  is negative and results in an angular distribution with a minimum at  $0^\circ$  and a maximum at  $90^\circ$ . For a quadrupole ( $\Delta\mathbf{I} = 2$ ) transition (E2), the distribution will have the form,

$$W(\theta) = A_0[1 + A_2 P_2(\cos\theta) + A_4 P_4(\cos\theta)] \quad (16)$$

where  $P_4(\cos\theta) = \frac{1}{8}(35\cos^4\theta - 30\cos^2\theta + 3)$ . If  $A_2$  is positive and  $A_4$  negative, it has an angular distribution with a minimum at  $90^\circ$  and maximum at  $0^\circ$ .

### 3.4.3 Angular Correlations

In angular correlations measurements, two detectors are placed at angles,  $\theta_1$  and  $\theta_2$  with respect to the beam direction and the angle between the detectors is  $\phi$  as shown in Figure 22. Consider an event where two gamma-rays emitted in cascade from initial nuclear

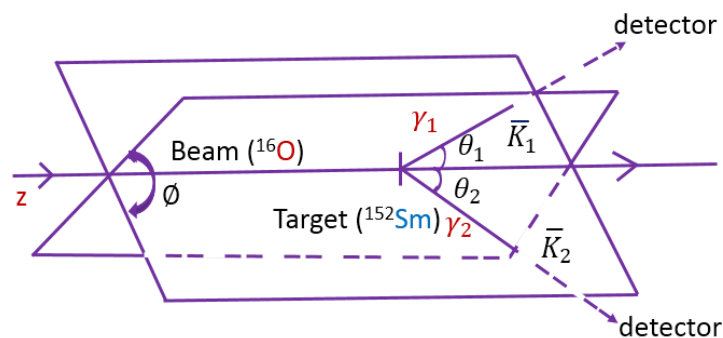
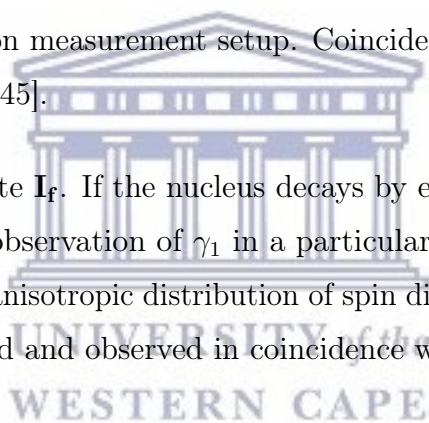


Figure 22: Gamma correlation measurement setup. Coincident measurements of consecutive gammas are performed [45].

state  $\mathbf{I}_i$  to a final nuclear state  $\mathbf{I}_f$ . If the nucleus decays by emitting  $\gamma_1$  followed by  $\gamma_2$  as indicated in Figure 23, the observation of  $\gamma_1$  in a particular direction picks out a set of nuclei in the state  $\mathbf{I}$  with an anisotropic distribution of spin directions and the distribution will persist until  $\gamma_2$  is emitted and observed in coincidence with  $\gamma_1$  [46].



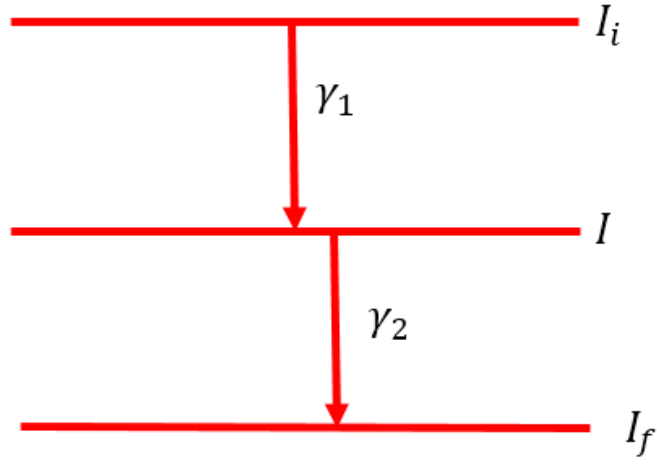


Figure 23: Schematic diagram showing level scheme for two successive gamma rays.

The angular correlation of the two successive gamma-rays emitted from an oriented source is thus given by [46]:

$$W(\theta_1, \theta_2, \phi) = \sum_{\lambda_1 \lambda_2} B\lambda_1(\mathbf{I}_1) \mathbf{A}_\lambda^{\lambda_2 \lambda_1}(\mathbf{X}_1) \mathbf{A}_{\lambda_2}(\mathbf{X}_2) \mathbf{H}_{\lambda_1 \lambda_2}(\theta_1, \theta_2, \phi) \quad (17)$$

From the above expression N is a normalisation factor, and the indices  $\lambda$ ,  $\lambda_1$  and  $\lambda_2$  are integers limited by the spins and multiplicities of the gamma-ray transitions.  $B\lambda_1(\mathbf{I}_1)$  are orientation parameters that depend on the substate population parameters:

$$B\lambda_1(I_i) = (2I + 1) \sum_m (-1)^{I+1} \langle I - m | m | \lambda 0 \rangle P(m) \quad (18)$$

The  $A_\lambda^{\lambda_2 \lambda_1}$  coefficients are defined as:

$$A_\lambda^{\lambda_2 \lambda_1} = [F_\lambda^{\lambda_2 \lambda_1}(LLI_f I_i) + 2\delta F_\lambda^{\lambda_2 \lambda_1}(LL'I_f I_i + \delta^2 F_\lambda^{\lambda_2 \lambda_1}(L'L'I_f I_i))] \frac{1}{1 + \delta^2} \quad (19)$$

These coefficients contain information on the nuclear wave function and spins of the states, multiplicities and mixing ratios of the transitions. The F-coefficients are products of Winger 3-j and 9-j symbols. The function  $H_{\lambda_1 \lambda_2}(\theta_1, \theta_2, \phi)$  describes the angular dependence [45].

### 3.4.4 Directional Correlations of Gamma Rays from Oriented States (DCO)

The directional correlation from oriented states (DCO), is the ratio of two angular correlation functions  $W(\theta_1, \theta_2, \phi)$  and  $W(\theta_2, \theta_1, \phi)$ , which is used to determine the multipole order (i.e dipole or quadrupole) of the gamma-transitions in any nucleus of interest. DCO measurements involve the determination of the coincidence intensities for two gammas. The dipole or quadrupole nature of transitions can be investigated by placing detectors at different angles. The directional correlation from an oriented state is given by:

$$R_{DCO} = \frac{W(\theta_1, \theta_2, \phi)}{W(\theta_2, \theta_1, \phi)} \quad (20)$$

where  $W(\theta_1, \theta_2, \phi)$  is the angular correlation of  $\gamma_1$  detected at  $\theta_1$  in coincidence with  $\gamma_2$  detected at  $\theta_2$ , and  $W(\theta_2, \theta_1, \phi)$  is the angular correlation of  $\gamma_1$  detected at  $\theta_2$  in coincidence with  $\gamma_2$  detected at  $\theta_1$ , as shown in Figure 24. The experimental  $R_{DCO}$  is given by:

$$R_{DCO} = \frac{I_{\theta_2}^{\gamma_1}(Gated_{\theta_1}^{\gamma_2})}{I_{\theta_1}^{\gamma_1}(Gated_{\theta_2}^{\gamma_2})} \quad (21)$$

where  $I_{\theta_2}^{\gamma_1}$  is the intensity of  $\gamma_1$  detected at  $\theta_2$  and  $I_{\theta_1}^{\gamma_1}(Gated_{\theta_2}^{\gamma_2})$  is the intensity of  $\gamma_1$  detected at  $\theta_2$  gated on  $\gamma_2$  detected at  $\theta_1$ . In the case of the AFRODITE gamma-ray spectrometer the angles  $\theta_1$  and  $\theta_2$  are  $90^\circ$  and  $135^\circ$ . For this work the angle  $\phi$  is  $\approx 15^\circ$  on average.

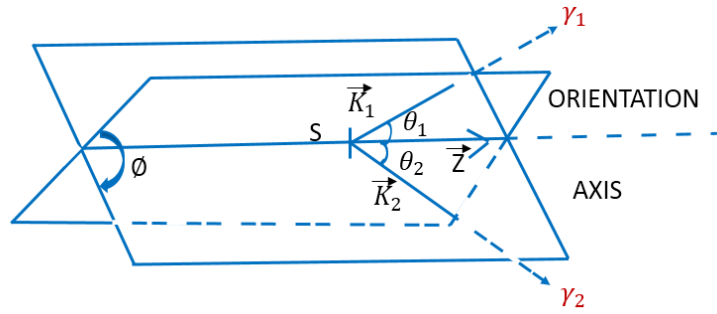


Figure 24: The angles in a directional correlation of two successive radiations emitted from an axially oriented state (DCO).

### 3.4.5 Linear Polarization Measurements

DCO ratios are complemented by linear polarization to give an unambiguous multipolarity assignment. Using clover detectors makes linear polarization measurement possible, which is very important since it tells us whether the transition is of electric or magnetic in nature. Figure 25 is the illustration of how linear polarization works when a gamma-ray strikes a crystal of the clover detector (at  $90^\circ$  to the beam direction) and Compton scatters into another crystal where it is absorbed. The direction of Compton scattering is different for electric and magnetic type transitions [47]. When gamma-rays are linearly polarized, the angular distribution function of scattered gamma-rays does not only depend on their outgoing direction  $\theta$  with respect to the beam axis, but also on their electric field direction with respect to the reaction plane defined by outgoing gamma-rays and the beam axis. Since the linear polarization of gamma-rays emitted from oriented states of nuclei has a close relation to their angular distribution, the linear polarization of these gamma-rays in terms of their angular distribution functions is given by [48]:

$$P(\theta) = \frac{W(\theta, \zeta = 0^\circ) - W(\theta, \zeta = 90^\circ)}{W(\theta, \zeta = 0^\circ) + W(\theta, \zeta = 90^\circ)} \quad (22)$$

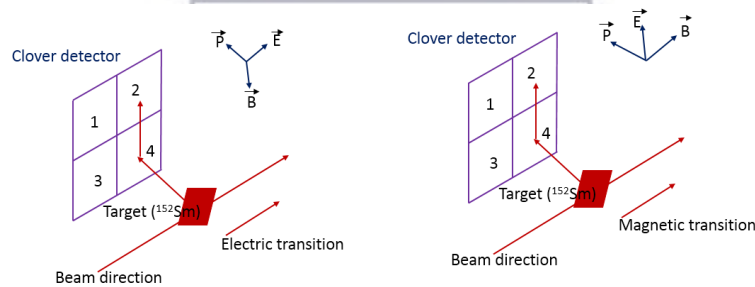


Figure 25: Linear polarization measurements using a clover detector.

where  $W(\theta, \zeta = 0^\circ)$  represents the angular distribution function when their electric field is parallel to the reaction plane, and  $W(\theta, \zeta = 90^\circ)$  represents the angular distribution function where it is perpendicular to the reaction plane, see Figure 26 [49]. The linear polarization anisotropy is defined by the difference between the number of gamma-rays scattered perpendicular and parallel with respect to the beam direction divided by their sum:

$$A_P = \frac{aN_{\perp} - N_{\parallel}}{aN_{\perp} + N_{\parallel}} \quad (23)$$

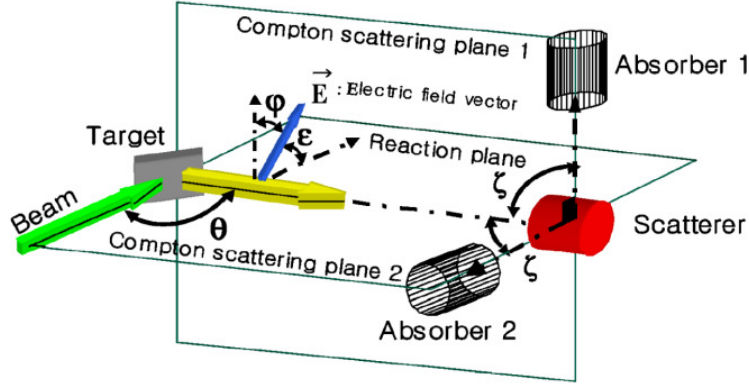


Figure 26: The setup showing linear polarization measurements of gamma-rays [49].

Table 1: Indicates the sign of the linear polarization of gamma-rays for different radiation type.

Radiation type	$A_2$	$A_4$	$P(\theta)$
Stretched M1	-	0	-
Unstretched M1	+	0	+
Stretched E1	-	0	+
Unstretched E1	+	0	-
Stretched M2	+	-	-
Stretched E2	+	-	+

where  $N_{\perp}$  and  $N_{\parallel}$  indicates coincidence counts perpendicular and parallel to the reaction plane, respectively. The coefficient  $a$  represents the relative efficiency of the detector (normalization constant). The normalization constant  $a$  can be deduced by taking the ratio of  $N_{\perp}$  and  $N_{\parallel}$  for unpolarised gamma-rays emitted from a standard calibration source, such as  $^{152}\text{Eu}$ , and it also corrects for any instrumental effect between horizontal and vertical planes. The linear polarization and the linear polarization anisotropy are related through the equation:

$$A_p = QP(\theta) \quad (24)$$

where  $Q$  is the polarization sensitivity. In general, the polarization anisotropy has positive sign for stretched electric transitions and negative sign for stretched magnetic transitions due to its preferential scattering along the parallel direction, and the opposite for unstretched transitions. Table 1 shows the signs of linear polarization of gamma-rays for different radiation types.

## 3.5 Data Analysis

### 3.5.1 Energy Calibration

Energy calibration is the first work to be done in a gamma-ray spectroscopy experiment before the start of the measurement. In this experiment a  $^{152}\text{Eu}$  radioactive source was used to obtain a reliable set of calibration coefficients for all clover detectors. The crystals of the clover detector collect data independently (i.e., there is no correspondence between the energies and the channels for each crystal) therefore they have to be gain matched. Energy calibration coefficients are obtained through the quadratic equation which calibrates the clover crystals to the same relation. The quadratic energy calibration equation is given by:

$$E = a_0 + a_1x + a_2x^2 \quad (25)$$

where  $E$  is the energy,  $x$  is a channel number, and  $a_0, a_1, a_2$  are gain matching coefficients [47].

The  $^{152}\text{Eu}$  radioactive source was run for approximately one hour, to accumulate sufficient counting statistics. The quadratic energy calibration was mapped onto a linear energy equation  $E = 0.5x'$  with channels as shown in Figure 27.



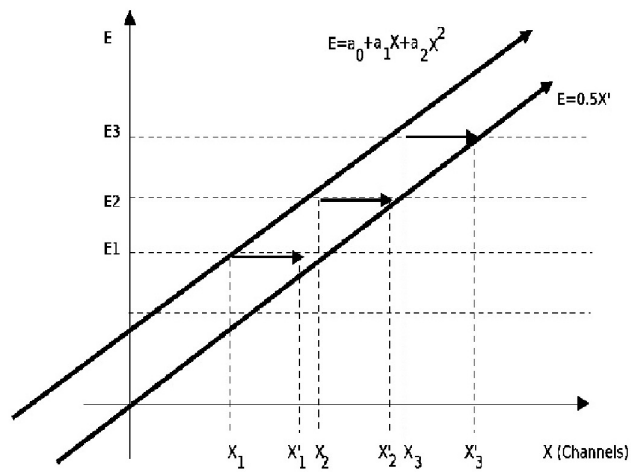


Figure 27: The schematic mapping of the quadratic equation  $E = a_0 + a_1x + a_2x^2$  and the linear equation  $E = 0.5x'$  [35].

### 3.5.2 Efficiency Calibration

There are various types of efficiency measurements that exist in radiation detection, including absolute, relative, and photopeak efficiency.  $^{152}\text{Eu}$  radioactive source was used to determine the efficiency calibration. This measurement is very important because it gives us a precise figure for the detector efficiency in order to relate the number of pulses counted to the number of gamma-rays incident on the detector. These efficiencies can be defined as:

- The photopeak efficiency is given by:

$$E_{ph} = \frac{N_{peak}}{\Omega N_{emitted}} \quad (26)$$

where,  $N_{peak}$  is the number of gamma-rays in the photopeak, and  $\Omega$  is the solid angle covered by the detector, and  $N_{emitted}$  is the number of gamma-rays emitted by the source.

- The absolute efficiency is given by:

$$E_{abs} = \frac{N_{det}}{\Omega N_{emitted}} \quad (27)$$

where,  $N_{det}$  is the number of events detected.

Usually the relative efficiency of detectors is compared to that of a 7.6 cm length and 7.6 cm diameter NaI(Tl) detector at a distance of 25 cm from the source.

- The relative efficiency is given by:

$$E_{rel} = \frac{(E_{ph}\Omega)_{detector}}{(E_{ph}\Omega)'_{NaI}} \quad (28)$$

where,  $(E_{ph}\Omega)'_{NaI} = 1.244 \times 10^{-3}$  for a NaI detector of 7.6 cm length and 7.6 cm diameter at a distance of 25 cm from the source [50]. Finally Radware [50] was used to determine the relative efficiency curves for clovers at  $90^\circ$  and  $135^\circ$ . Figure 28 shows the relative efficiency curve for all 8 AFRODITE clover detectors measured with a  $^{152}\text{Eu}$  radioactive source.

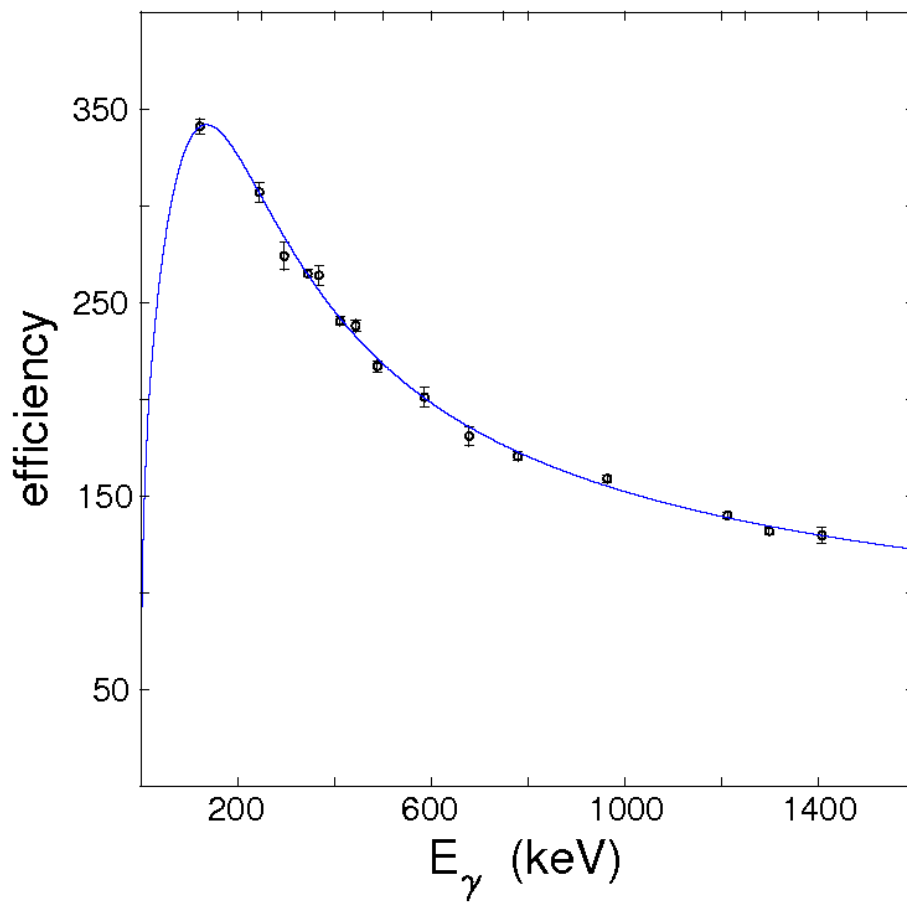


Figure 28: Relative efficiency curve for all 8 AFRODITE clover detectors measured with a  $^{152}\text{Eu}$  radioactive source.

### 3.5.3 Gamma-gamma matrix construction

The analysis of data from HIFE reactions often begins with the creation of two-dimensional histograms from double-coincidence data or three-dimensional histograms from triple-coincidence data [15]. These histograms can then be examined by specifying energies for all but one of the axes and inspecting the projection onto the remaining axis. The Radware graphical-analysis package (ESCL8R) [50] was used in this experiment to create and examine the gamma-gamma matrix (two dimensional histogram), through which the level scheme for the nucleus of interest was created. MTSort software [51] was used in this experiment to sort the massive data which was measured to construct gamma-gamma matrices used in the DCO and polarization measurements. For DCO measurements we used the gamma-rays detected by clover detectors positioned at  $90^\circ$  on the y-axis in coincidence with gamma-rays detected at  $135^\circ$  on the x-axis. And for polarization measurements we used the gamma-rays scattered parallel and perpendicular to the reaction plane in the clover detectors at  $90^\circ$  in coincidence with any other gamma-rays. Figure 29 represents the time (X-axis) spectrum for coincidences between two gamma-ray detectors obtained in the current experiment.

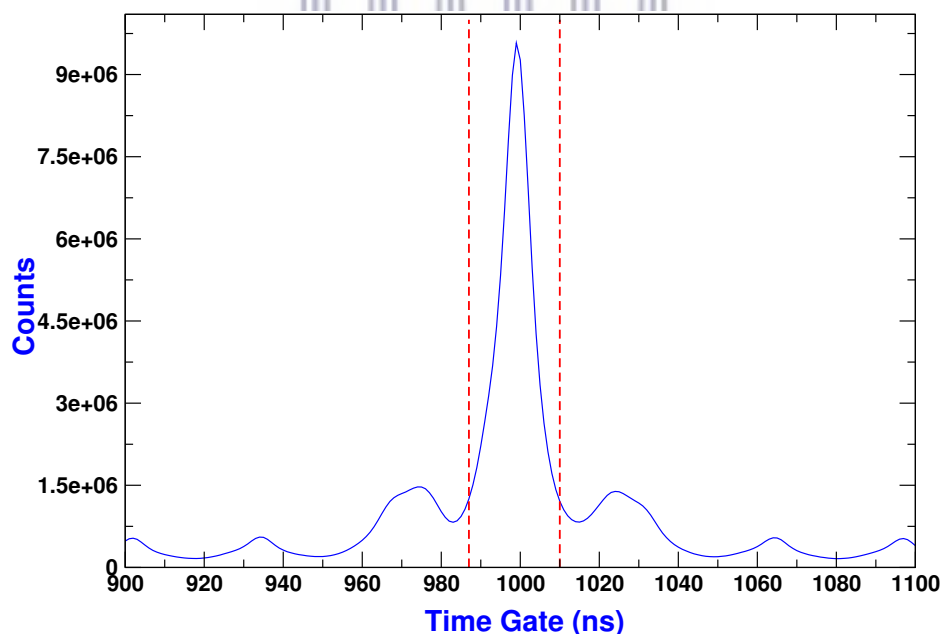


Figure 29: Time spectrum used for extraction of coincidence events obtained in the current experiment. Typical events occurred in the gate 987-1010 ns.

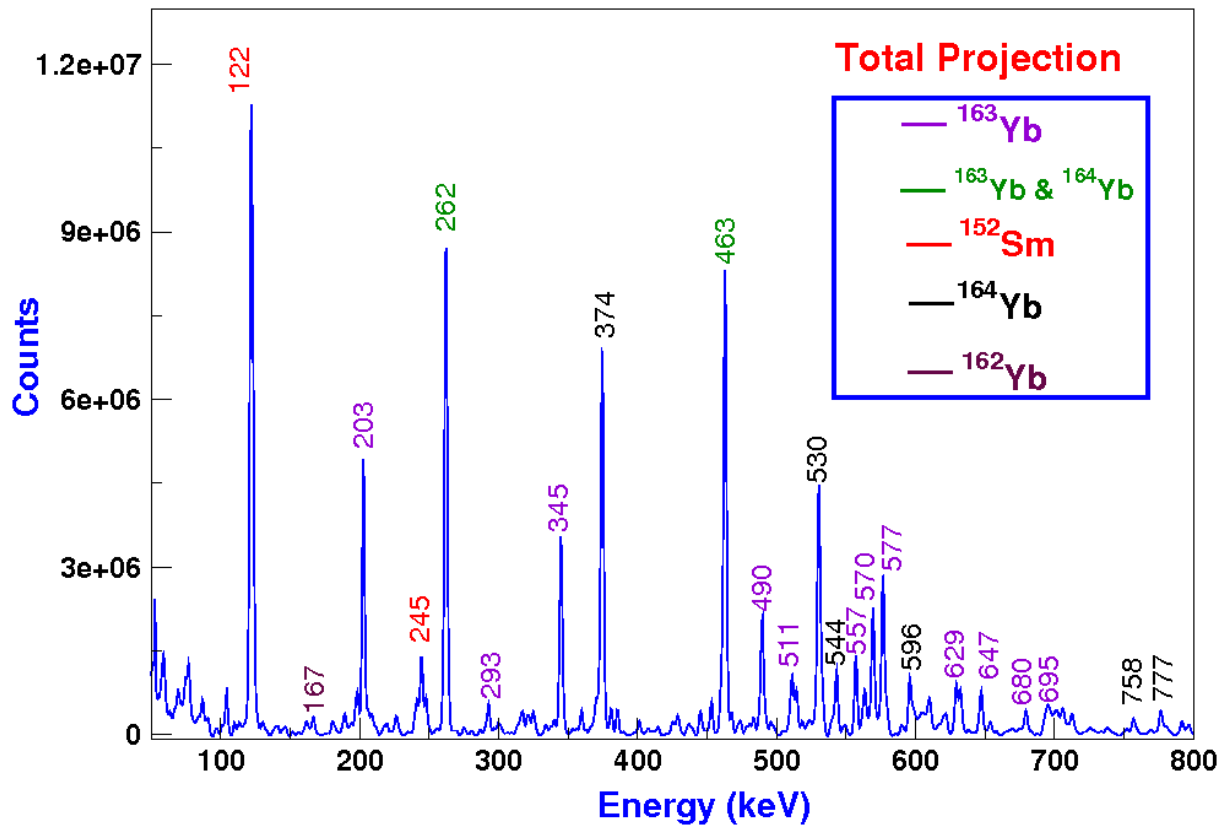


Figure 30: Background-subtracted total projection Spectrum (gamma-gamma coincidences  $2.5 \times 10^9$ ). The gamma rays labelled in black colour belong to  $^{164}\text{Yb}$  and are produced by 4n channel. The gamma ray labelled in maroon belongs to  $^{162}\text{Yb}$  and was produced by 6n channel of the present heavy-ion fusion evaporation reaction. The gamma rays labelled in green belong to both  $^{163}\text{Yb}$ , and  $^{164}\text{Yb}$  nuclei. The gamma rays labelled in red belong to  $^{152}\text{Sm}$  and are produced by the coulomb excitation of the target. The gamma rays belonging to  $^{163}\text{Yb}$  are produced by the 5n channel of the present HIFE reaction and are labelled in violet colour.

### 3.5.4 Spin and Parity Selection Rules

Spins ( $I$ ) and parities ( $\pi$ ) are the major tools used to describe the structural behaviour of nuclei. Spin ( $I$ ) can be defined as an intrinsic form of angular momentum carried by elementary particles, composite particles (hadrons), and atomic nuclei [52]. Parity ( $\pi$ ) is a property of a wave function that depends on the result of the operation of inversion in which all co-ordinates are reflected through the origin, i.e.  $\mathbf{r} \rightarrow -\mathbf{r}$ . In quantum mechanics, a multipole transition  $2^\ell$ , from the initial  $I_i$  to the final  $I_f$  nuclear state, carries an angular momentum of  $l\hbar$  per gamma ray. The index  $l$  denotes the order of the multipole expansion where  $l = 1$  (dipole),  $l = 2$  (quadrupole),  $l = 3$  (octupoles) and so on. During an electromagnetic transition between the initial level at excitation energy  $E_i$  and the final state at excitation energy  $E_f$ , the conservation of angular momentum is actually governed by the following expression:

$$|\vec{I}_i - \vec{I}_f| \leq |\vec{I}_i + \vec{I}_f| \quad \forall \neq 0 \quad (29)$$

where  $I_i$  and  $I_f$  denote the initial and final spins and are also vector quantities. The expression above reveal the information about the possible amount of angular momentum that can be carried off by the emitted electromagnetic transitions. The transitions are said to be stretched when  $\Delta I = \ell$  and unstretched when the difference in  $I < \ell$  [15]. Also depending on the parity of the initial or final level, the identity of a gamma-ray linking two nuclear states can be classified as either electric (E) or magnetic (M) where the conservation of parity is given by:

$$\Pi(E\ell) = (-1)^\ell \quad (30)$$

$$\Pi(M\ell) = (-1)^{\ell+1} \quad (31)$$

$$\Pi_i = \Pi_\gamma \bullet \Pi_f \quad (32)$$

The selection rules above dictates that the parity of nuclear states connecting M1, E2, M3, E4, M5 etc should be the same while it is opposite for E1, M2, E3, M4, E5 and so on [15].

### 3.5.5 Midas MTsort

MTsort requires the MIDAS analysis package. This program was used to sort the massive data and convert it into a form that is compatible with Radware. In order to run MTsort, the user needs to supply a file of sorting instructions written in the sort language. This file should contain a description of the experimental setup, the number of spectra (histograms) required and set of commands to be applied to each event being sorted. The sort package checks the syntax of these instructions and translate them into a more low level language, i.e. C. If there are mistakes in your sortfile the sort package reports them as warnings or errors. The reason of sorting the data is to get rid of what you don't want (junk) and leave only what is useful [16].



## Chapter 4

# 4 Experimental Results

## 4.1 Contaminants

There are quite a number of contaminants that were observed in this work. This is despite the fact that our target had a high isotopic enrichment of about 98.27%. In Heavy-Ion Fusion Evaporation reaction experiments there are many sources of contaminants. However, the most predominant ones are the residual nuclei, due to other reaction channels. PACE4 simulation, discussed in section 3.1 was successfully used to determine the optimal percentage yield and cross section of various isotopes of Yb, including that of the nucleus of interest namely,  $^{163}\text{Yb}$ . The results obtained from the plot of percentage yield as a function of energy are listed in the table 2.

The level schemes of those contaminants observed in our data, were constructed. The reason for constructing those level schemes, was to avoid the confusion between new transitions and contaminants. As can be seen in Figure 30, the gamma decays that correspond to  $^{162}\text{Yb}$  contaminant are due to the emission of 6 neutrons from the reaction  $^{152}\text{Sm}(^{16}\text{O},6n)^{162}\text{Yb}$ .  $^{164}\text{Yb}$  (contaminant) were generated through the emission of 4 neutrons from the above mentioned reaction. As shown in Figure 30 gamma decays from  $^{164}\text{Yb}$  gammas are predominant in the total projection spectrum compared to the ones of the nucleus of interest ( $^{163}\text{Yb}$ ). This is because the core nucleus  $^{162}\text{Yb}$  is an even-even nucleus with a lower density of states such that the intensity gets concentrated in fewer transitions. The other reason is that the PACE4 calculations were slightly unreliable in estimating an optimum beam energy.



Table 2: Energy versus % yields from PACE4. In this work a beam of  $E_{lab} = 93$  MeV was used.

Energies (MeV)	$^{165}\text{Yb}$	$^{164}\text{Yb}$	$^{163}\text{Yb}$	$^{162}\text{Yb}$
70	26.3	67.9	0	0
75	7.4	83.5	0.2	0
80	1.7	71.9	15.8	0
84	0.3	43.2	43.6	0
85	0.1	37.5	49.2	0
90	0	16.9	63.5	3.3
93	0	8.1	60.2	13.8
95	0	5.2	53.5	22.9
100	0.1	1.2	31.9	42.7

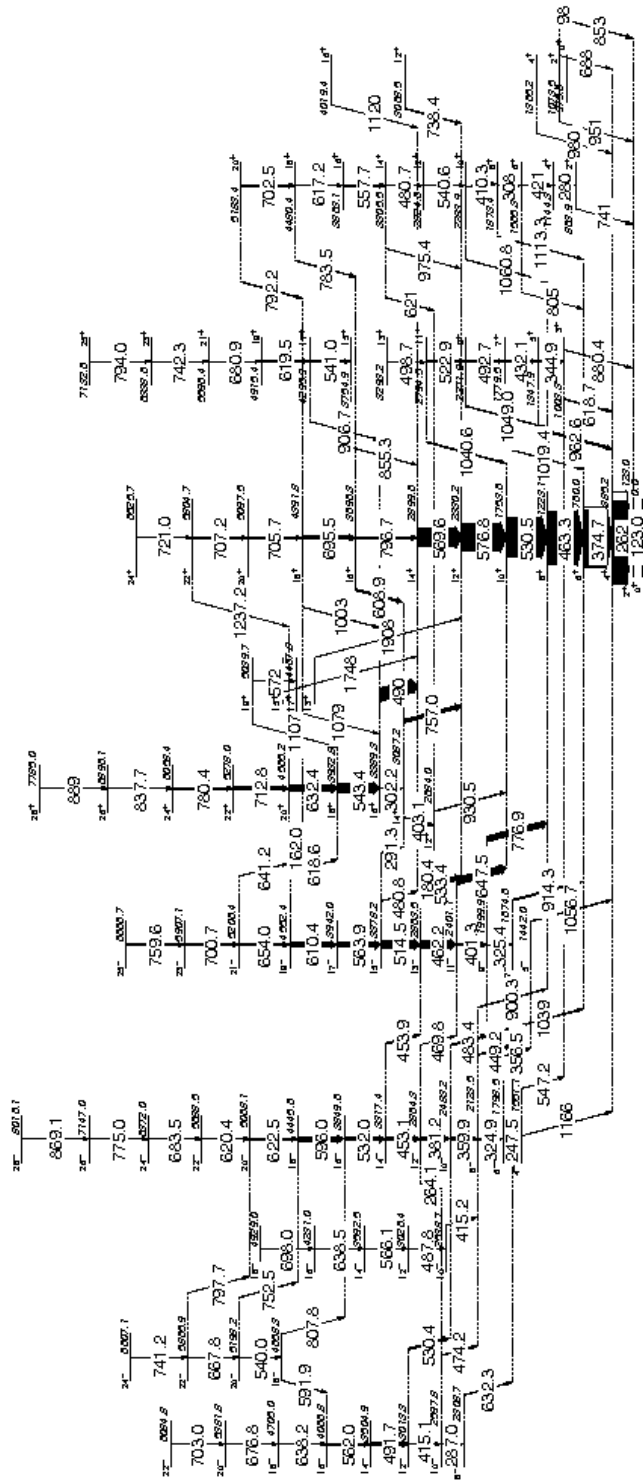


Figure 31: Partial level scheme of  $^{164}\text{Yb}$ .

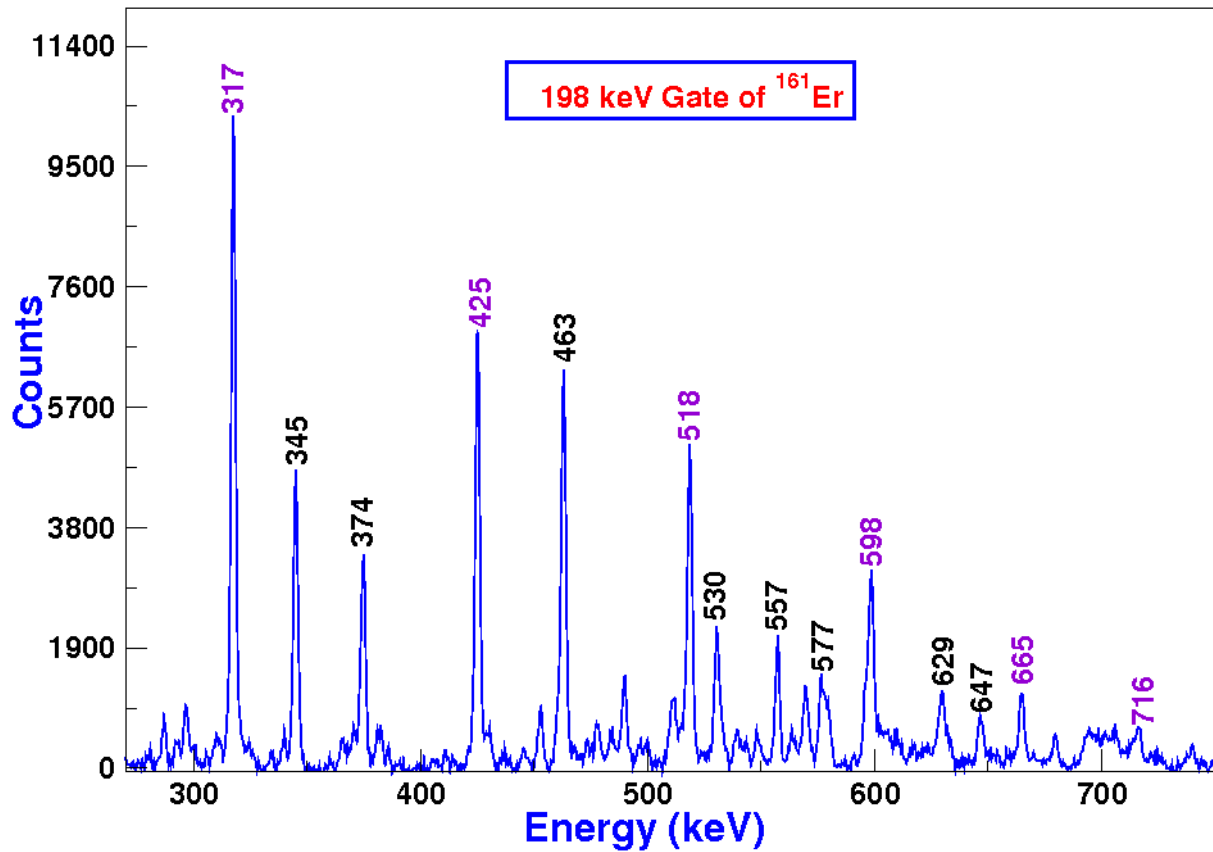


Figure 32: Coincidence spectrum from the  $^{152}\text{Sm}(^{16}\text{O},5\text{n})^{163}\text{Yb}$  and  $^{152}\text{Sm}(^{16}\text{O},\alpha3\text{n})^{161}\text{Er}$  reactions obtained by setting a gate on the transition at 198 keV. The yrast sequence in  $^{161}\text{Er}$  is labelled in violet. Transitions labelled in black belong to  $^{163}\text{Yb}$ , and  $^{164}\text{Yb}$ .

Richter [6] proposed a cascade of stretched E2 transitions (198, 318, 425, 519, 597 and 667 keV) in  $^{163}\text{Yb}$  with intensity below 10% of that of the 203 keV transition in the yrast band, using the  $^{152}\text{Sm}(^{16}\text{O},5\text{n})^{163}\text{Yb}$ , but Kownacky *et al.*, [5] suggested that this decay sequence is not associated with  $^{163}\text{Yb}$ . With the aid of the  $^{149}\text{Sm}(^{18}\text{O},4\text{n})^{163}\text{Yb}$  reaction, Kownacky *et al.*, [5] discovered that the intensity of this cascade is only  $\approx 2\%$  when compared to that of the 203 keV transition, thus making it less likely for the band in question to be in  $^{163}\text{Yb}$ . This decay cascade is also observed in our data as shown in Figure 32. Our findings are consistent with those of Kownacky *et al.*, as we also found out that this transition does not belong to  $^{163}\text{Yb}$ , but to  $^{161}\text{Er}$ .

## 4.2 Status of the Rotational Bands in $^{163}\text{Yb}$ Nucleus

The spin-parity selection rules and DCO values have been used to assign multipolarity to newly observed transitions. The polarization sensitivity possessed by the AFRODITE array has been very instrumental in confirming the electromagnetic nature of the gamma-rays observed in this study (see Figures 39 and 40). The DCO ratios ( $R_{DCO}$ ) for the AFRODITE data-set were deduced using detectors at  $135^\circ$  versus those at  $90^\circ$  in this work.

### 4.2.1 The Yrast Band (+,+)

The previous in-beam work [6] and [5] established the yrast band the favoured signature (+,+) based on the odd neutron occupying the  $i_{13/2}$  Nilsson  $5/2^+$ [642] orbital. Members of this band have previously been observed up to a level with spin-parity assignment  $45/2^+$  [5]. The subsequent study reported an additional 769.6 keV stretched E2 transition which extended the yrast cascade to the  $49/2^+$  level [5]. Figure 34 shows all nine transitions (203, 345, 463, 557, 629, 680, 706, 726 and 769 keV) as reported in [5]. Table 3 shows that this study does not only confirm the existence of this band but also the spin and parity assigned to its inband member by the previous in-beam works. In [5] they proposed the extension of this band up to spin  $53/2^+$  with an energy  $\approx 835$  keV, but we could not observe it in our coincidence data. Figure 33 shows the coincidence spectrum confirming the existence of this band in this work. It was obtained by setting a gate on the 345 keV transition.

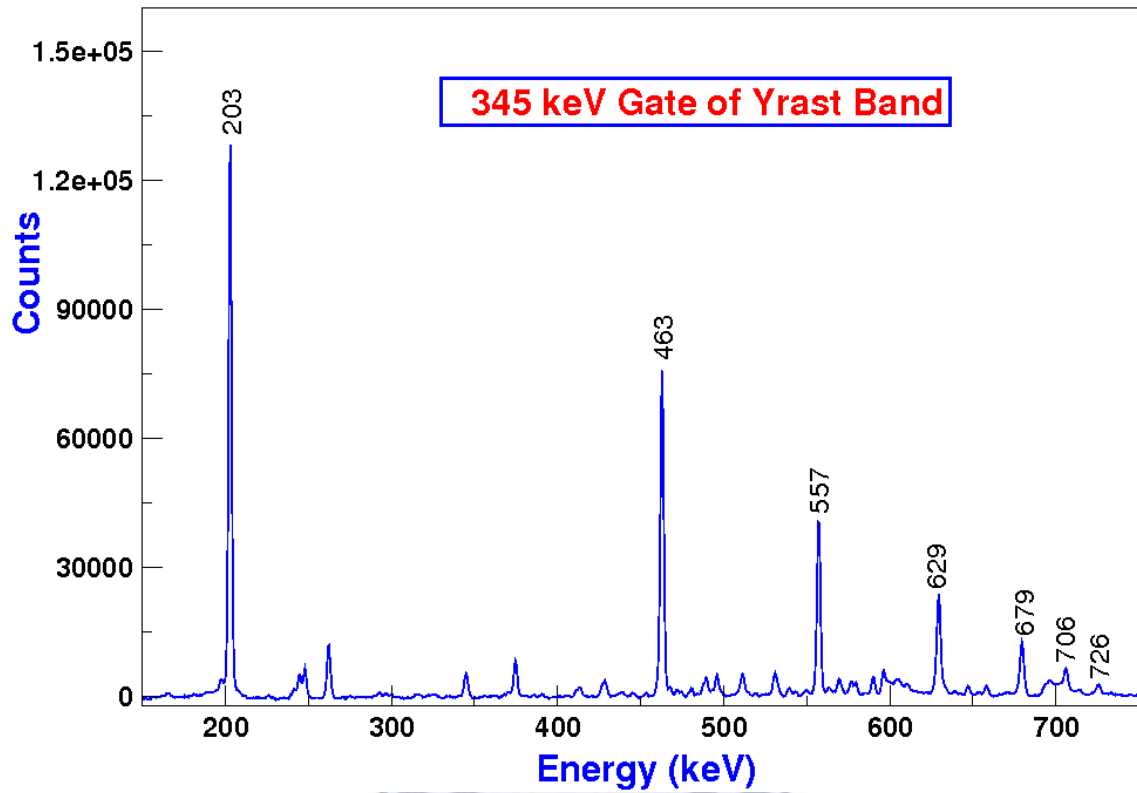
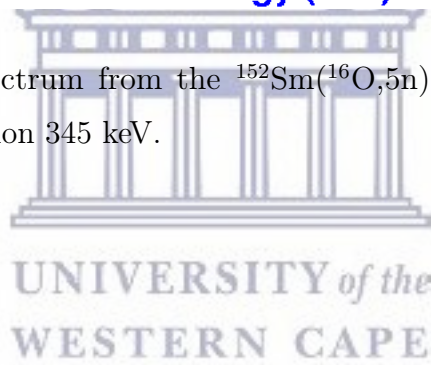


Figure 33: Coincidence spectrum from the  $^{152}\text{Sm}(^{16}\text{O},5n)^{163}\text{Yb}$  reaction obtained by setting a gate on the transition 345 keV.



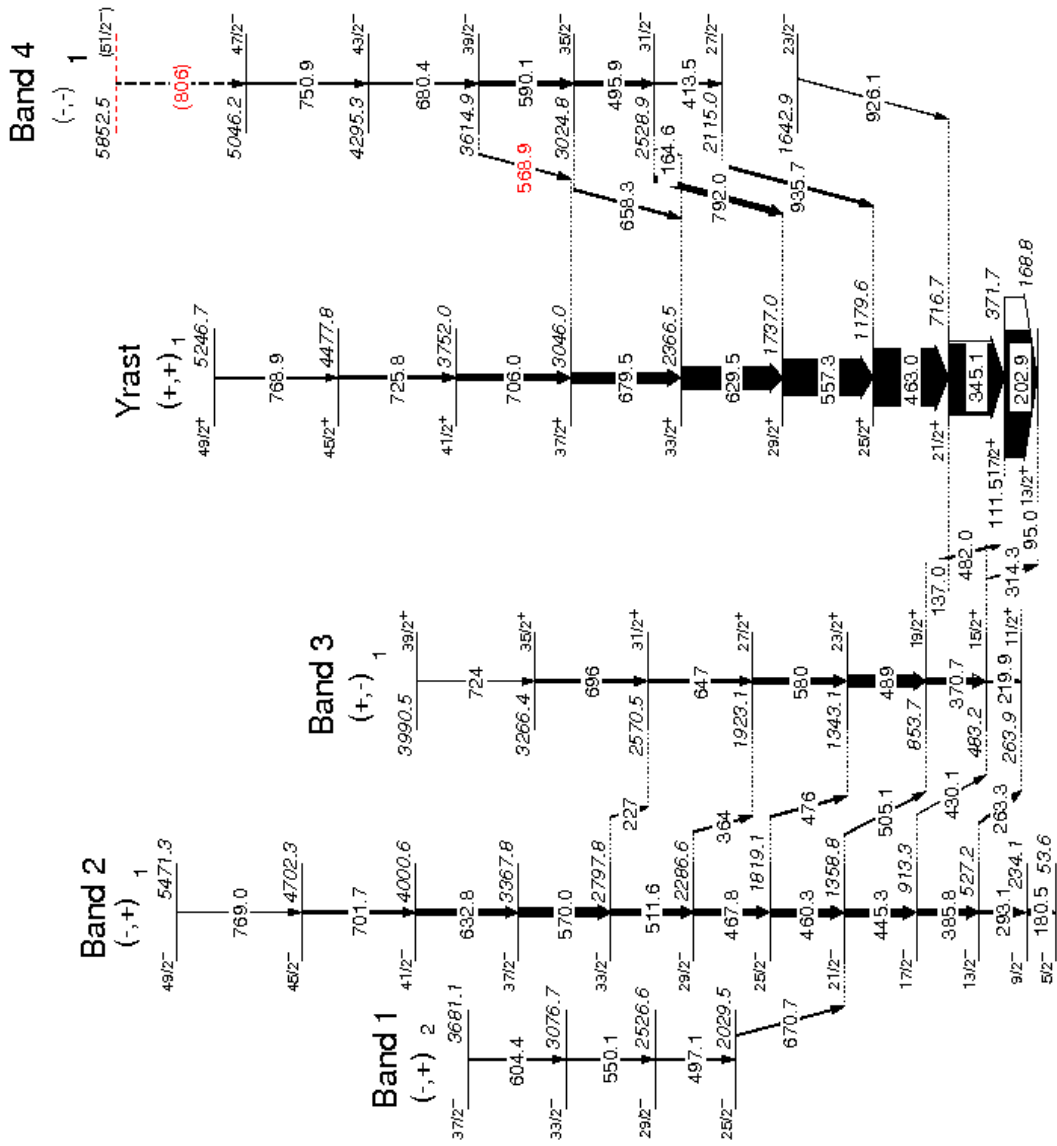


Figure 34: Partial level scheme of  $^{163}\text{Yb}$  deduced from the current work, showing previously known bands. Findings from the current work are labelled in red.

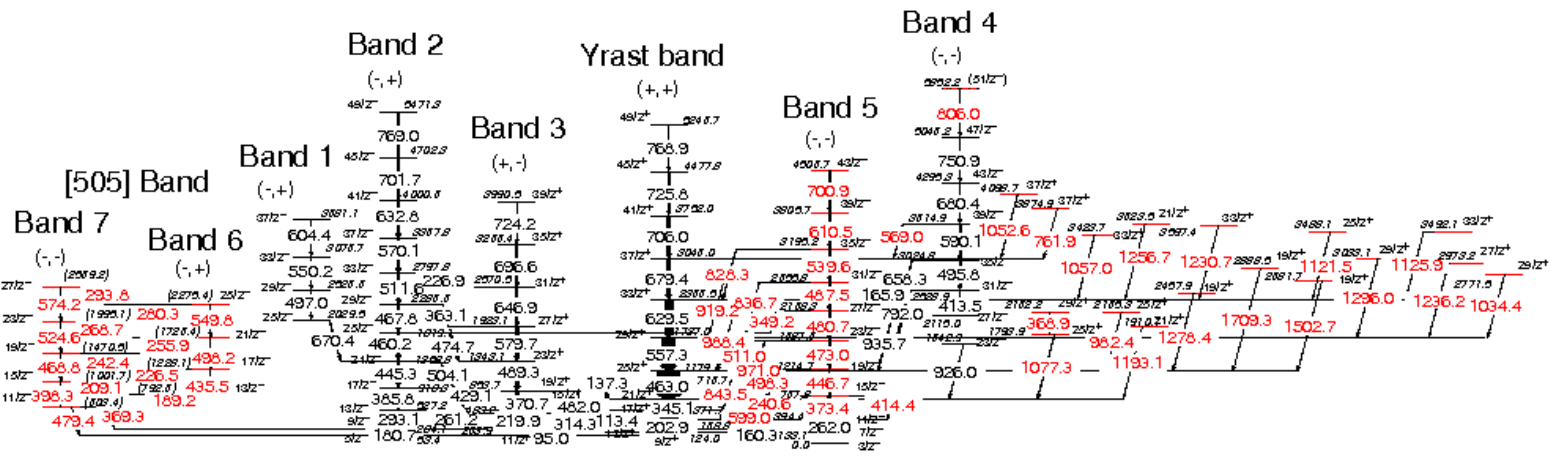


Figure 35: The complete level scheme of  $^{163}\text{Yb}$  deduced from the current work. Findings from the current work are labelled in red while previously known transitions, deduced from previous in-beam work are labelled in black.

Table 3: Energy levels, gamma-ray energies ( $E_\gamma$ ),  $R_{DCO}$  ratios, linear polarization anisotropy  $A_p$ , and multipolarity (multi.) assignments of transitions depopulating the yrast band.

E-levels (keV)	$E_\gamma$ (keV)	$J_i^\pi \rightarrow J_f^\pi$	$R_{DCO}$	$A_p$	Multi.	Band
Yrast band						
371.7	202.9	$17/2^+ \rightarrow 13/2^+$	1.074(3)	0.194(19)	E2	Yrast
716.7	345.1	$21/2^+ \rightarrow 17/2^+$	1.076(5)	0.155(8)	E2	Yrast
1179.6	463	$25/2^+ \rightarrow 21/2^+$	1.110(5)	0.134(14)	E2	Yrast
1737	557.3	$29/2^+ \rightarrow 25/2^+$	1.081(7)	0.137(17)	E2	Yrast
2366.5	629.5	$33/2^+ \rightarrow 29/2^+$	1.074(10)	0.038 (19)	E2	Yrast
3046	679.5	$37/2^+ \rightarrow 33/2^+$	1.026(14)	0.123(24)	E2	Yrast
3752	706	$41/2^+ \rightarrow 37/2^+$	1.039(26)	0.052(37)	E2	Yrast
4477.8	725.8	$45/2^+ \rightarrow 41/2^+$	0.924(80)	0.111(53)	E2	Yrast
5246.7	768.9	$49/2^+ \rightarrow 45/2^+$	1.020 (112)	) <sup>b</sup>	) <sup>c</sup>	Yrast

)<sup>b</sup> insufficient statistics to measure linear polarization Anisotropy.

)<sup>c</sup> multipolarity could not be determined



Figures 36 and 37 show the polarization and DCO spectra used for the analysis of linear polarization anisotropy and DCO ratios respectively. The theory about linear polarization anisotropy and DCO ratios is discussed in detail in chapter 3 of this thesis.

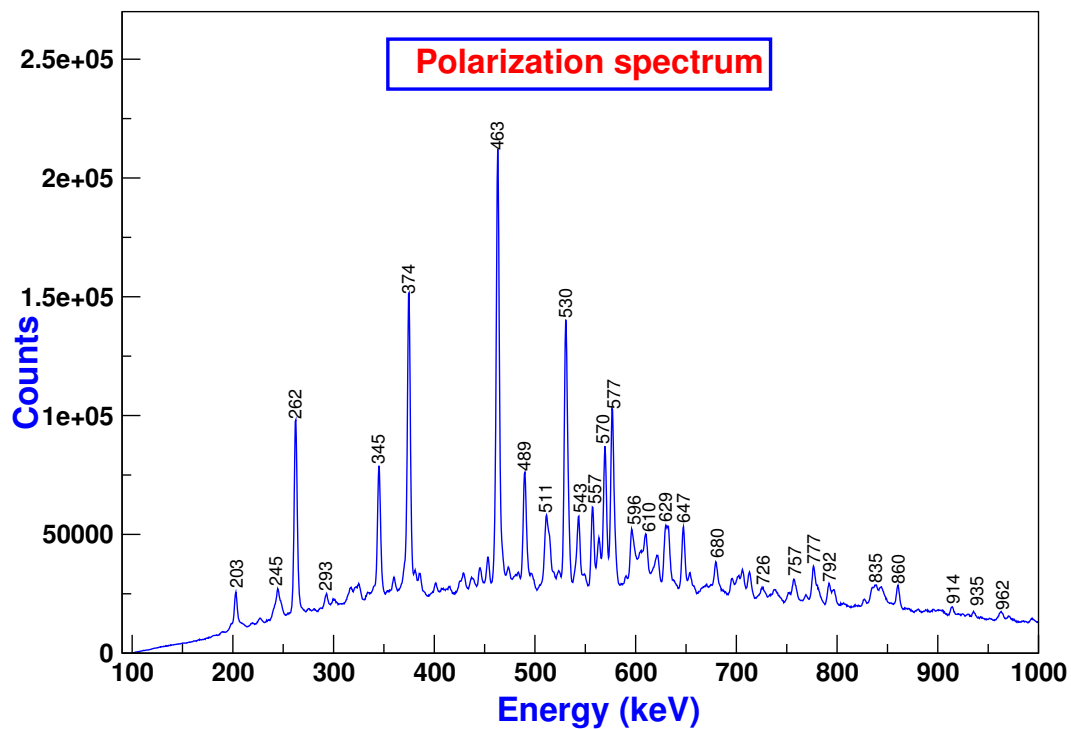
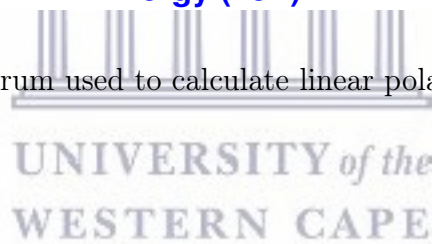


Figure 36: Polarization spectrum used to calculate linear polarization anisotropy in  $^{163}\text{Yb}$  (see equation 21).



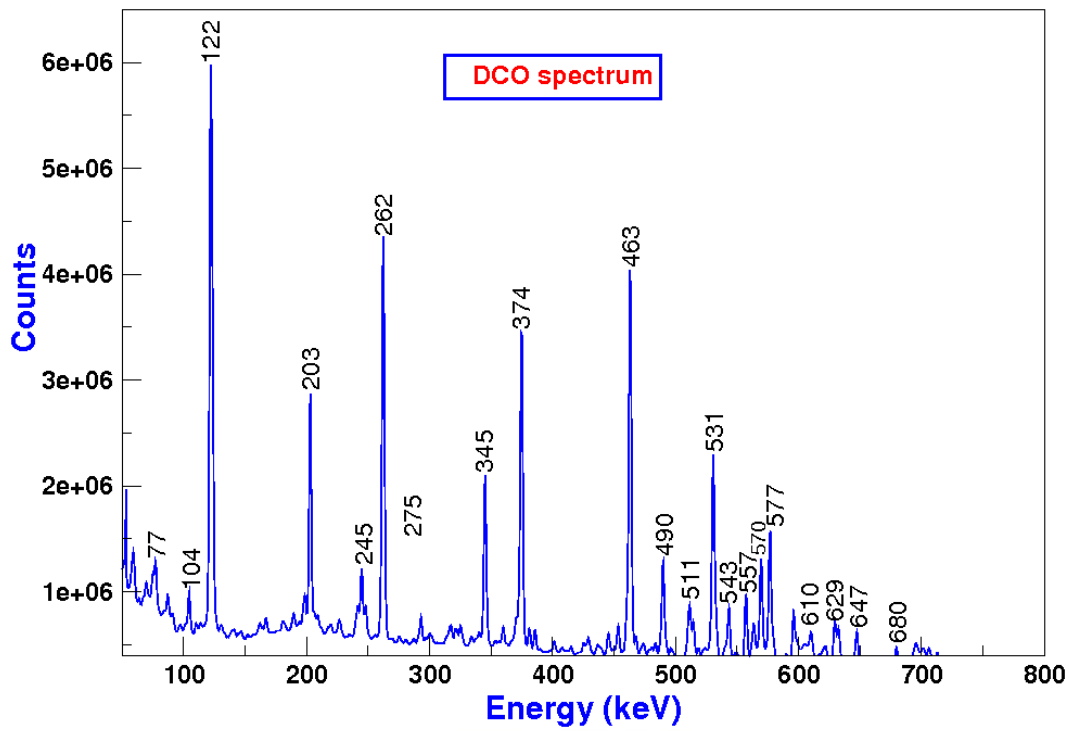


Figure 37: DCO spectrum of the matrix constructed for the measurements of  $R_{DCO}$  ratios projected onto  $135^0$  in  $^{163}\text{Yb}$  nucleus.



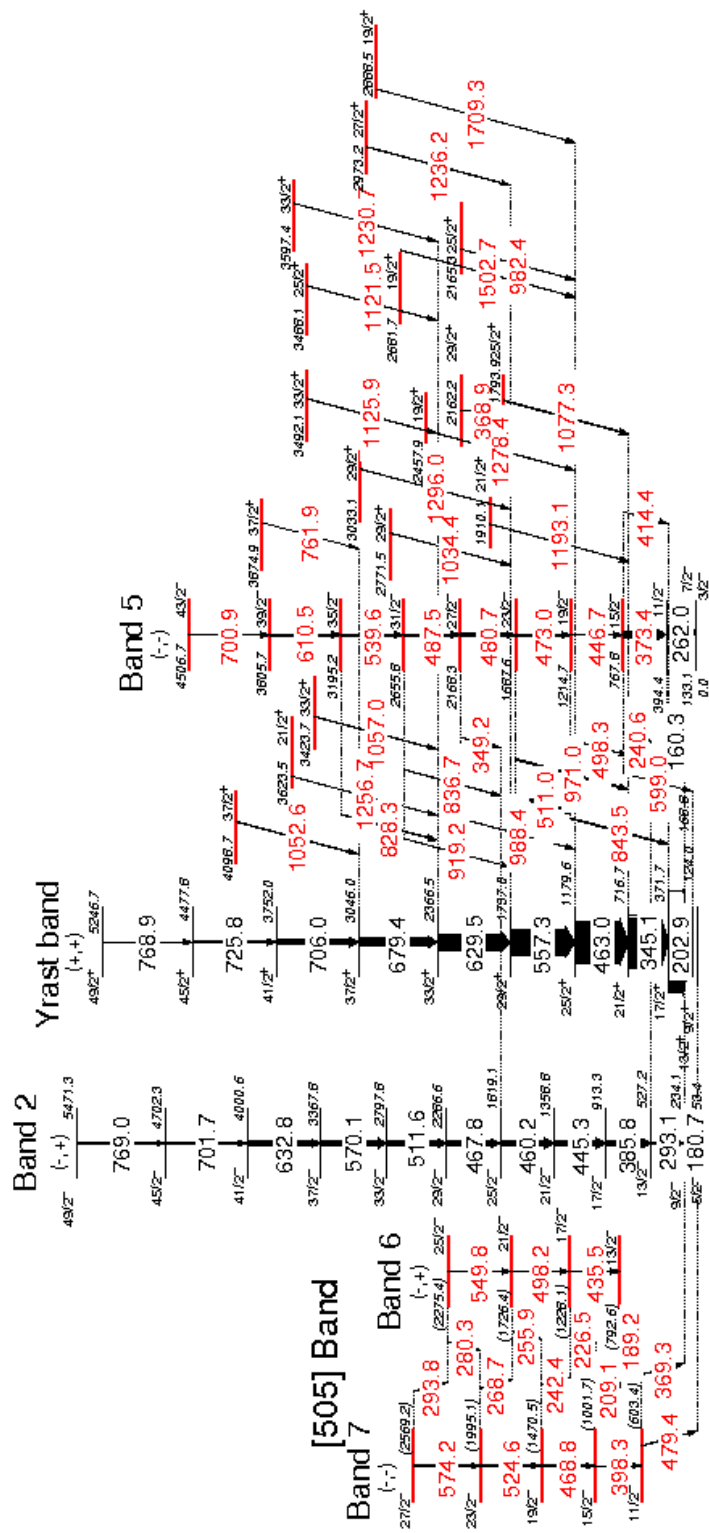


Figure 38: Partial level scheme of  $^{163}\text{Yb}$  showing new nuclear levels transition, (highlighted in red).

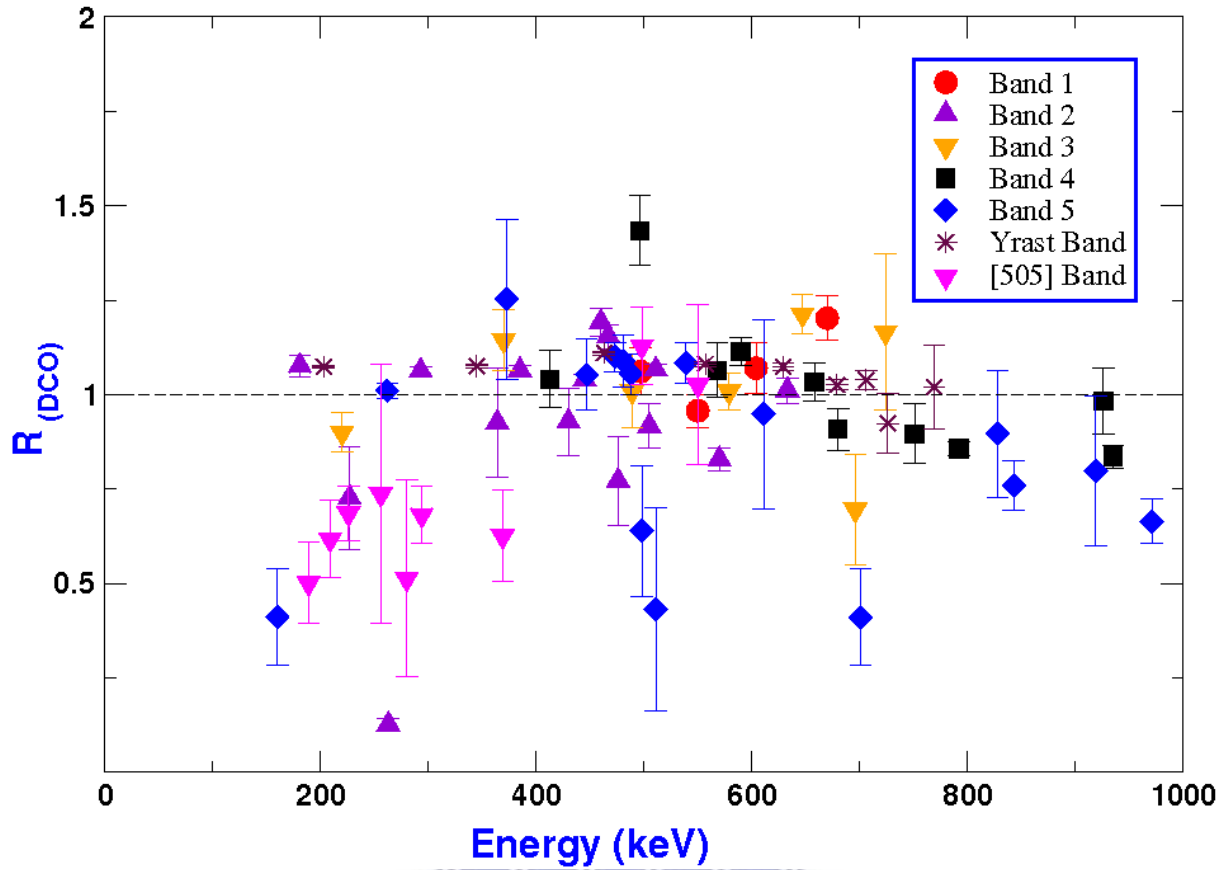


Figure 39: Experimentally measured DCO ratios, ( $R_{DCO}$ ), in  $^{163}\text{Yb}$ , deduced in the current work versus gamma-ray energies.

The most commonly used approach for determining the spin and parity of new levels, is by first determining the multipolarity of the linking transitions to levels of known spin and parity. In this work, the measured DCO ratio ( $R_{DCO}$ ), is defined as

$$R_{DCO} = \frac{W(90^\circ, 135^\circ)}{W(135^\circ, 90^\circ)}. \quad (33)$$

The numerator of equation 27 denotes the angular correlation function between de-excitation  $\gamma$ -rays, detected at  $90^\circ$  relative to the beam direction, and coincident  $\gamma$ -rays, detected at  $135^\circ$ . Figure 39 shows a  $R_{DCO}$  plot as function of energy (keV) obtained from this work. All the ratios in Figure 39 were obtained by setting a gate on pure stretched quadrupole transitions. The  $R_{DCO}$  value for known dipole transitions is  $\approx 0.56$  and is  $\approx 1.05$  for known quadrupole, when gates are set on quadrupole transitions. Alternatively when gating on a transition the corresponding values are  $\approx 1.1$  and  $\approx 1.8$  for dipole and quadrupole transitions respectively [53].

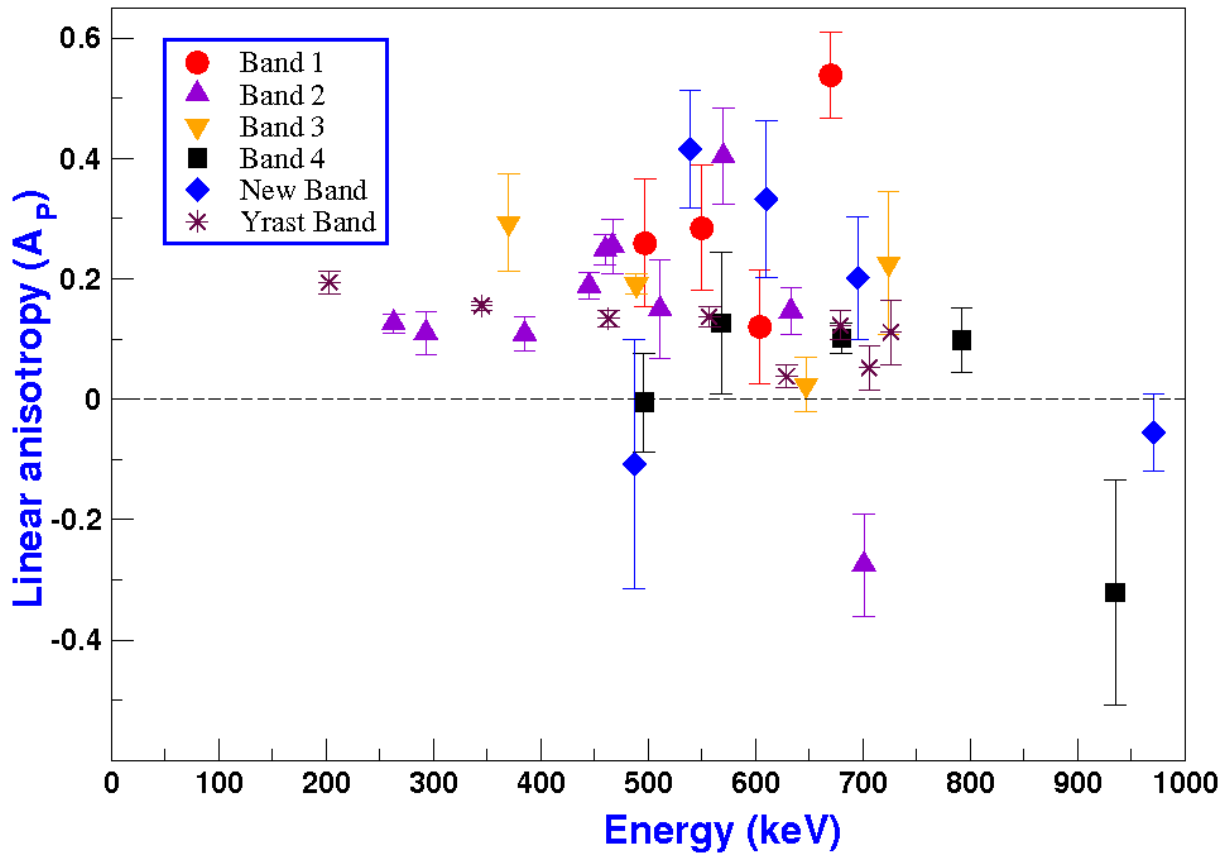


Figure 40: Plot for polarization anisotropy measurements as a function of energy obtained from this work.

The polarization measurements were deduced using clover detectors at  $90^\circ$ , such that stretched magnetic transitions have a negative sign while their electric counterparts have a positive sign, as shown in Figure 40. The polarization measurements for the newly established transitions are coloured in blue, while those of well-established transitions are coloured in, red, violet, orange, black and maroon.

#### 4.2.2 Other New States

We observed an additional 16 new states in  $^{163}\text{Yb}$  (Figure 38) all decaying to the yrast band. With the data available we were not able to assign these states to any particular configurations except for band 5.

### 4.2.3 Band 1 (-,+)

Band 1 consists of three stretched E2 transitions (see Figure 35). This band was observed for the first time by Kownacky *et al.*, [5] up to  $37/2^-$ . This band is linked to band 2 (-,+) via 670 keV transition. As can be seen in Figure 35 and Table 4, the current work confirms the placements made by [5]. In addition our work also confirms the spin and parity assignments made to the members of this structures by previous in-beam works. Finally, Figure 41 shows a spectrum with decays associated with this band, this confirming its existence in our work.

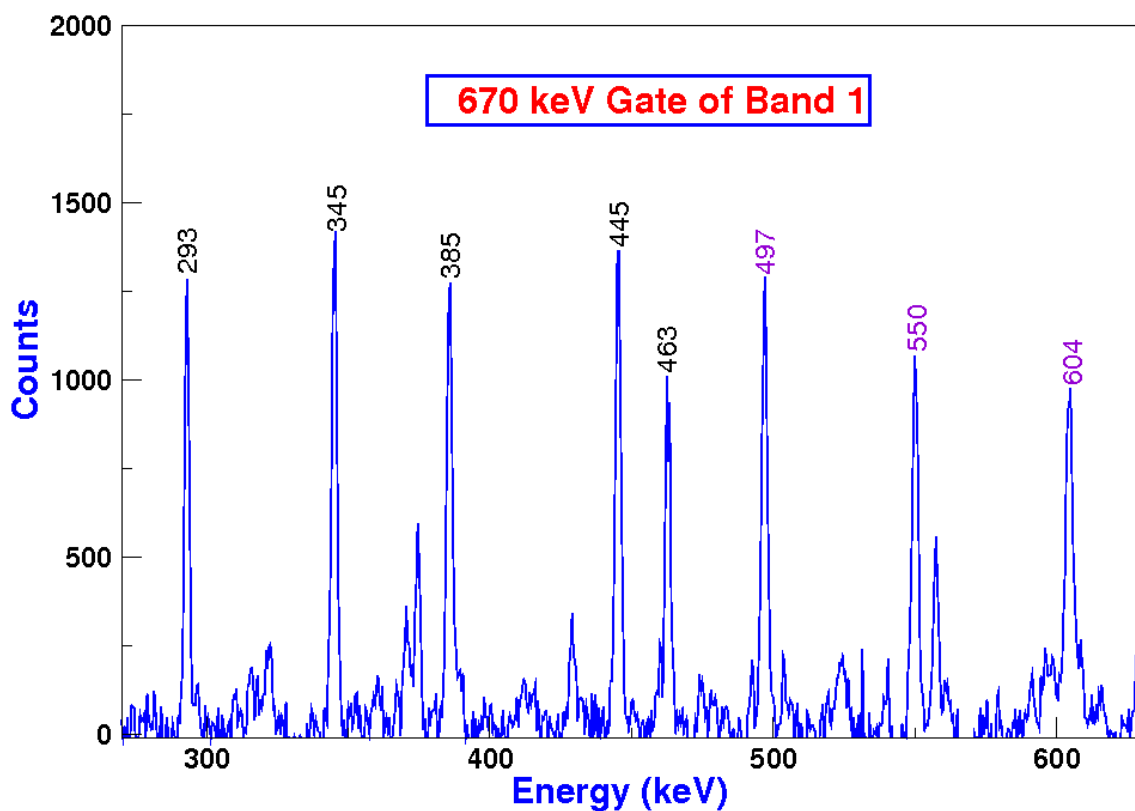
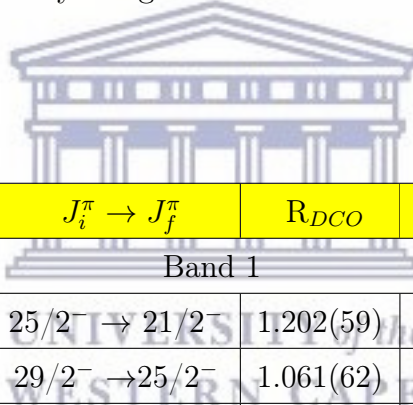


Figure 41: Coincidence spectrum from the  $^{152}\text{Sm}(^{16}\text{O},5\text{n})^{163}\text{Yb}$  reaction obtained by setting a gate on the transition 670 keV. Transitions labelled in violet are E2 transitions that belong to band 1, and transitions labelled in black are also E2 transitions that belong to band 2 and the yrast band of  $^{163}\text{Yb}$  nucleus.

Table 4: Energy levels, gamma-ray energies ( $E_\gamma$ ),  $R_{DCO}$  ratios, linear polarization anisotropy  $A_p$ , and multipolarity assignments of transitions depopulating band 1 in  $^{163}\text{Yb}$



E-levels (keV)	$E_\gamma$ (keV)	$J_i^\pi \rightarrow J_f^\pi$	$R_{DCO}$	$A_p$	Multi.	Band
Band 1						
2029.5	670.7	$25/2^- \rightarrow 21/2^-$	1.202(59)	0.538(71)	E2	1→2
2526.6	497.1	$29/2^- \rightarrow 25/2^-$	1.061(62)	0.259(106)	E2	1
3076.7	550.1	$33/2^- \rightarrow 29/2^-$	0.957(44)	0.284(104)	E2	1
3681.1	604.4	$37/2^- \rightarrow 33/2^-$	1.070(67)	0.120(95)	E2	1

#### 4.2.4 Band 2 (-,+)

Band 2 is the negative parity band which was first established in [6] and later revised by [5]. In fact, [5] changed the order of three transitions that were first observed in [6] and also managed to add 769 keV “stretched E2” transition which extended this sequence to  $\frac{49-}{2}$  level. These changes led to a smooth upbend instead of a sharp backbend as reported in [5]. The current work does not only confirm the placements made by [5] but also the assignment of spin and parity for this band (see Table 5). Figure 42, shows a coincidence spectrum deduced in the current work, which confirms the existence of this band.

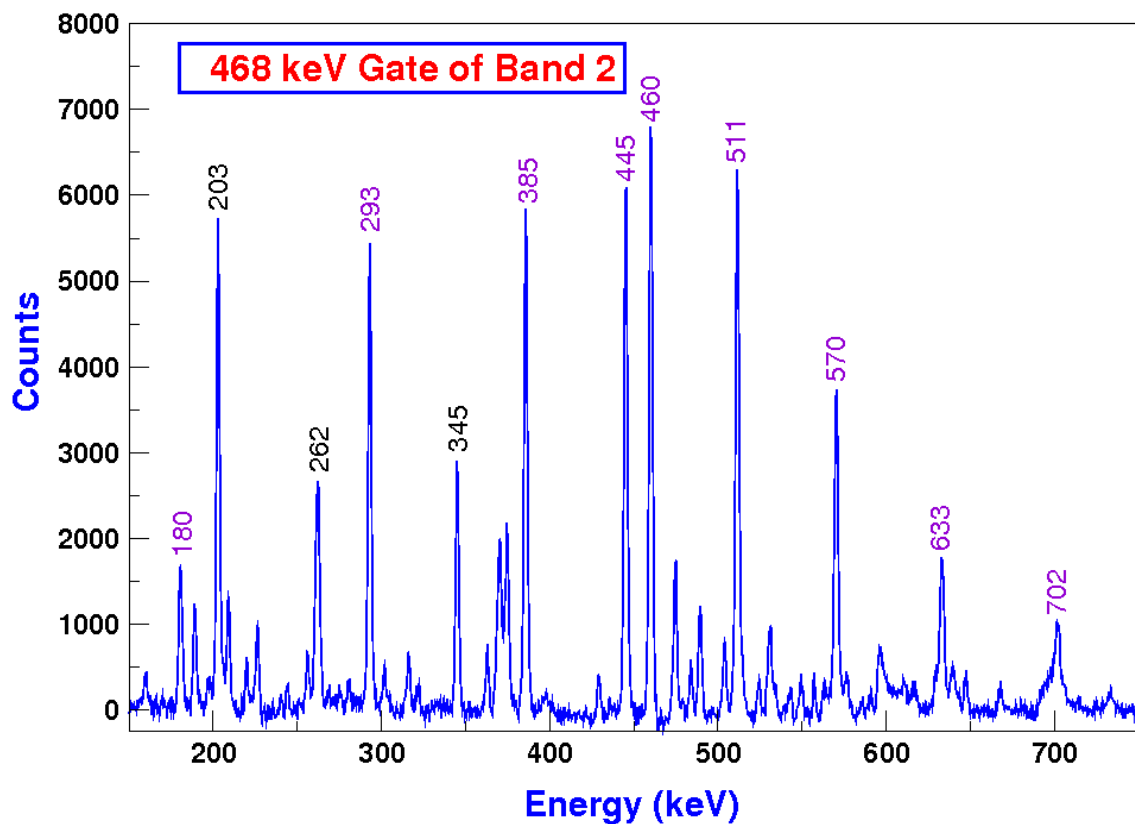


Figure 42: Coincidence spectrum from the  $^{152}\text{Sm}(^{16}\text{O},5n)^{163}\text{Yb}$  reaction obtained by setting a gate on the transition 468 keV. Transitions labelled in violet are E2 transitions that belong to band 2, labelled in black are also E2 transitions of the yrast band.



Table 5: Energy levels, gamma-ray energies ( $E_\gamma$ ),  $R_{DCO}$  ratios, linear polarization anisotropy  $A_p$ , and multipolarity assignments of transitions depopulating the rotational levels of band 2.

E-levels	$E_\gamma$ (keV)	$J_i^\pi \rightarrow J_f^\pi$	$R_{DCO}$	$A_p$	Multi.	Band
Band 2						
234.1	181.5	$9/2^- \rightarrow 5/2^-$	1.075(29)	) <sup>b</sup>	) <sup>c</sup>	2
527.2	261.2	$13/2^- \rightarrow 11/2^+$	) <sup>a</sup>	0.126(16)	) <sup>c</sup>	2→3
527.2	293.1	$13/2^- \rightarrow 9/2^-$	1.062(12)	0.110(36)	E2	2
913.3	385.8	$17/2^- \rightarrow 13/2^-$	1.064(12)	0.108(28)	E2	2
913.3	429.1	$17/2^- \rightarrow 15/2^+$	0.928(89)	) <sup>b</sup>	) <sup>c</sup>	2→3
1358.8	445.3	$21/2^- \rightarrow 17/2^-$	1.039(15)	0.188(22)	E2	2
1358.8	504.1	$21/2^- \rightarrow 19/2^+$	0.916(59)	) <sup>b</sup>	) <sup>c</sup>	2→3
1819.1	460.3	$25/2^- \rightarrow 21/2^-$	1.191(38)	0.248(25)	E2	2
1819.1	474.7	$25/2^- \rightarrow 23/2^+$	0.771(118)	) <sup>b</sup>	) <sup>c</sup>	2→3
2286.6	363	$29/2^+ \rightarrow 27/2^+$	0.925(144)	) <sup>b</sup>	) <sup>c</sup>	2→3
2286.6	467.8	$29/2^- \rightarrow 25/2^-$	1.153(33)	0.254(45)	E2	2
2797.8	227	$33/2^- \rightarrow 31/2^+$	0.726(136)	) <sup>b</sup>	) <sup>c</sup>	2→3
2797.8	511.6	$33/2^- \rightarrow 29/2^-$	1.065(16)	0.149(82)	E2	2
3367.8	570	$37/2^- \rightarrow 33/2^-$	0.945(18)	0.403(80)	E2	2
4000.6	632.8	$41/2^- \rightarrow 37/2^-$	1.011(34)	0.146(39)	E2	2
4702.3	701.7	$45/2^- \rightarrow 41/2^-$	1.119(115)	) <sup>b</sup>	) <sup>c</sup>	2
5471.3	769	$49/2^- \rightarrow 45/2^-$	) <sup>a</sup>	) <sup>b</sup>	) <sup>c</sup>	2

)<sup>a</sup> insufficient statistics to measure DCO ratios.

)<sup>b</sup> insufficient statistics to measure linear polarization Anisotropy.

)<sup>c</sup> multipolarity could not be determined

#### 4.2.5 Band 3 (+,-)

Band 3 is the unfavoured signature partner of the yrast band (+,-). This band was reported for the first time by Richter [6] who identified the following sequence of quadrupole transitions (220, 371, 489 and 580 keV) as band members of this structure. Richter [6] had observed this band up to  $27/2^+$ . The subsequent in-beam study by [5] confirmed these placements. In addition the latter also added three more transitions (647, 696 and 724 keV). The current study confirms the existence of this band (see Figures 42, and 43). In addition, we also confirm the spin and parity assignments made to this band by previous studies (see Table 6).

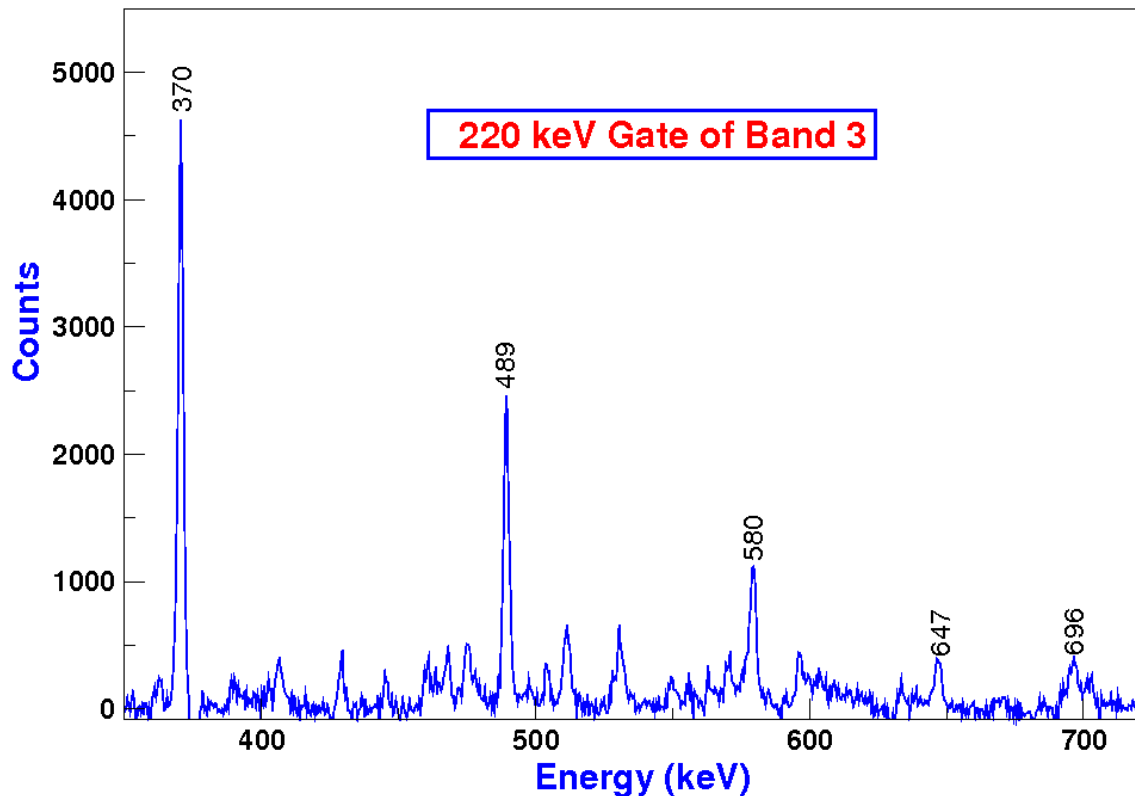


Figure 43: Coincidence spectrum from the  $^{152}\text{Sm}(^{16}\text{O},5n)^{163}\text{Yb}$  reaction obtained by setting a gate on the transition 220 keV.

Table 6: Energy levels, gamma-ray energies ( $E_\gamma$ ),  $R_{DCO}$  ratios, linear polarization anisotropy  $A_p$ , and multipolarity assignments of transitions depopulating the rotational levels of band 3 in  $^{163}\text{Yb}$ .

E-levels (keV)	$E_\gamma$ (keV)	$J_i^\pi \rightarrow J_f^\pi$	$R_{DCO}$	$A_p$	Multi.	Band
Band 3						
483.2	219.9	$15/2^+ \rightarrow 11/2^+$	0.900(52)	) <sup>b</sup>	) <sup>c</sup>	3
483.2	314.3	$15/2^+ \rightarrow 13/2^+$	) <sup>a</sup>	) <sup>b</sup>	) <sup>c</sup>	3→Yrast
853.7	137	$21/2^+ \rightarrow 19/2^+$	) <sup>a</sup>	) <sup>b</sup>	) <sup>c</sup>	3→Yrast
853.7	370.7	$19/2^+ \rightarrow 15/2^+$	1.144(81)	0.293 (88)	E2	3
853.7	482	$19/2^+ \rightarrow 17/2^+$	) <sup>a</sup>	) <sup>b</sup>	) <sup>c</sup>	3→Yrast
1343.1	489	$23/2^+ \rightarrow 19/2^+$	1.009(98)	0.191(17)	E2	3
1923.1	580	$27/2^+ \rightarrow 23/2^+$	1.009(48)	) <sup>b</sup>	) <sup>c</sup>	3
2570.5	647	$31/2^+ \rightarrow 27/2^+$	1.213(51)	0.024(45)	E2	3
3266.4	696	$35/2^+ \rightarrow 31/2^+$	0.977(45)	) <sup>b</sup>	) <sup>c</sup>	3
3990.5	724	$39/2^+ \rightarrow 35/2^+$	0.874(98)	0.226(118)	E2	3

)<sup>a</sup> insufficient statistics to measure DCO ratios.

)<sup>b</sup> insufficient statistics to measure linear polarization Anisotropy.

)<sup>c</sup> multipolarity could not be determined

#### 4.2.6 Band 4 (-,-)

Band 4 was first established by Kownacky *et al.*, [5]. This band is connected to the yrast band by five transitions with energies 658 ( $\frac{35}{2}^- \rightarrow \frac{33}{2}^+$ ), 792 ( $\frac{31}{2}^- \rightarrow \frac{29}{2}^+$ ), 379 ( $\frac{27}{2}^- \rightarrow \frac{29}{2}^+$ ), 936 ( $\frac{27}{2}^- \rightarrow \frac{25}{2}^+$ ), and 926 keV ( $\frac{23}{2}^- \rightarrow \frac{21}{2}^+$ ). The current work does not only confirm the placements made by [5] but also the assignment of spin and parity for this band (see Table 7). In the current work this band has been extended up to a level with spin-parity  $51/2^-$ . An additional E1 transition which connects the yrast band has been observed for the first time in the current work (see Figures 44 and 34).

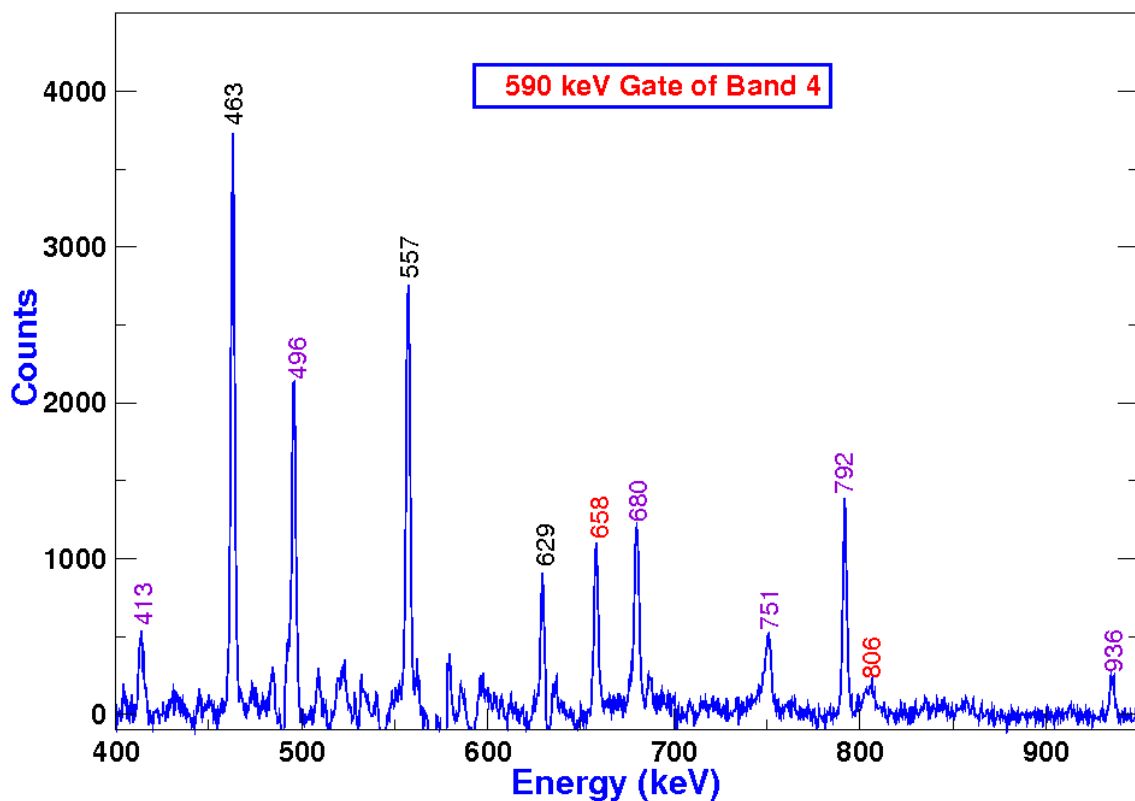


Figure 44: Coincidence spectrum from the  $^{152}\text{Sm}(^{16}\text{O},5\text{n})^{163}\text{Yb}$  reaction obtained by setting a gate on the transition 590 keV. Transitions labelled in violet are E2 transitions that belong to band 4, while those labelled in black are E2 transitions of yrast band. The transition labelled in red is the new E1 transition that connects band 4 and the yrast band and also the E2 transition which extend band 4 up to spin  $51/2^-$ .

Table 7: Energy levels, gamma-ray energies ( $E_\gamma$ ),  $R_{DCO}$  ratios, linear polarization anisotropy  $A_p$ , and multipolarity assignments of transitions depopulating the rotational levels of band 4 in  $^{163}\text{Yb}$ .

E-levels (keV)	$E_\gamma$ (keV)	$J_i^\pi \rightarrow J_f^\pi$	$R_{DCO}$	$A_p$	Multi.	Band
Band 4						
1642.9	926.1	$23/2^- \rightarrow 21/2^+$	0.982(87)	) <sup>b</sup>	) <sup>c</sup>	4→Yrast
2115.0	935.7	$27/2^- \rightarrow 25/2^+$	0.836(30)	0.195(85)	E2	4→Yrast
2528.9	413.5	$31/2^- \rightarrow 27/2^-$	1.041(75)	) <sup>b</sup>	) <sup>c</sup>	4
2528.9	792	$31/2^- \rightarrow 29/2^+$	0.857(20)	0.098(54)	E2	4→Yrast
3024.8	495.9	$35/2^- \rightarrow 31/2^-$	1.434(92)	) <sup>b</sup>	) <sup>c</sup>	4
3024.8	658.3	$35/2^- \rightarrow 33/2^+$	1.033(50)	) <sup>b</sup>	) <sup>c</sup>	4→Yrast
3614.9	568.9	$39/2^- \rightarrow 37/2^+$	1.064(72)	0.126(118)	E2	4→Yrast
3614.9	590.1	$39/2^- \rightarrow 35/2^-$	1.114(37)	) <sup>b</sup>	) <sup>c</sup>	4
4295.3	680.4	$43/2^- \rightarrow 39/2^-$	0.908(55)	0.101(25)	E2	4
5046.2	750.9	$47/2^- \rightarrow 43/2^-$	0.896(79)	) <sup>b</sup>	) <sup>c</sup>	4
5852.5	806	$51/2^- \rightarrow 47/2^-$	) <sup>a</sup>	) <sup>b</sup>	) <sup>c</sup>	4

)<sup>a</sup> insufficient statistics to measure DCO ratios.

)<sup>b</sup> insufficient statistics to measure Linear Polarization Anisotropy.

)<sup>c</sup> multipolarity could not be determined

#### 4.2.7 Band 5

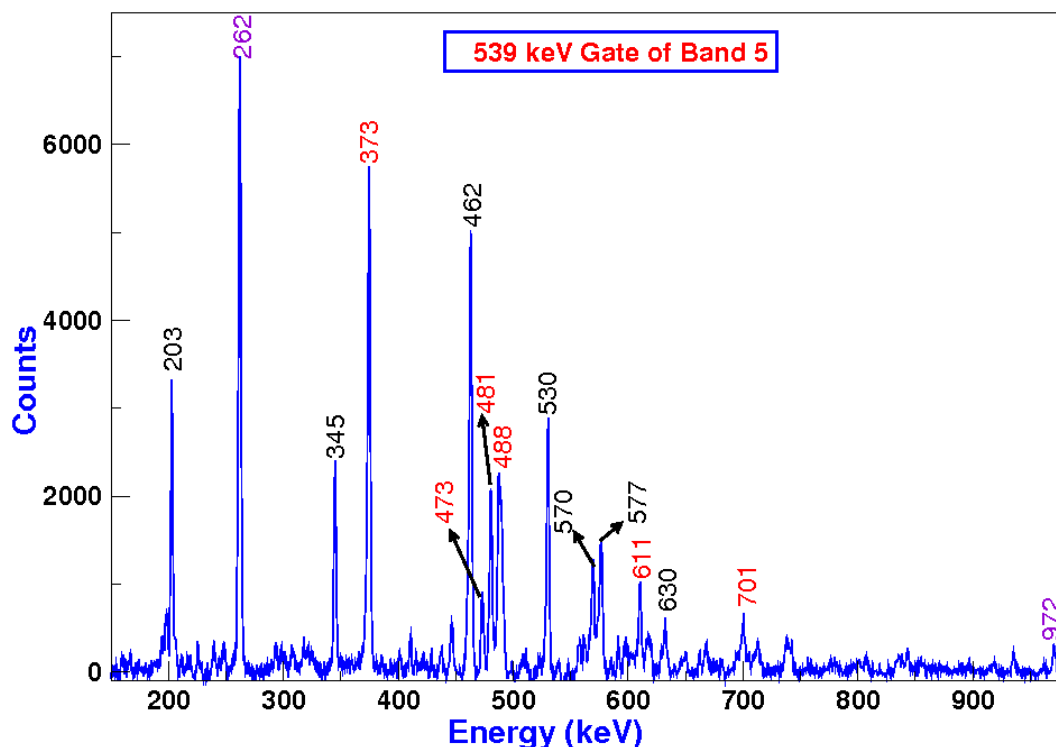


Figure 45: Coincidence spectrum from the  $^{152}\text{Sm}(^{16}\text{O},5n)^{163}\text{Yb}$  reaction obtained by setting a gate on the newly observed transition 539 keV. Newly observed transitions are labelled in red, the known transitions of this band are labelled in violet and the transitions labelled in black belong to the yrast band in the present coincidence spectrum.

A sequence of 11 rotational levels based on a nuclear state 0 keV, has been observed. Previous studies by Richter [6], and Kownacky *et al.*, [5] had reported this band up to the  $11/2^-$  state. However, in the present study, this band has been extended significantly by 8 new transitions up to spin  $43/2^-$ . Polarization and DCO measurements were performed for the majority of new in-band transitions and they are consistent with them being stretched E2s, see Table 8. As can be seen in Figure 38, in this work, we also report a series of new E1 ( $J \rightarrow J \pm 1$ ) interband transitions that links band 5 to the yrast band. The spectrum showing transitions associated with this rotational structure is shown in Figure 45.

Table 8: Energy levels, gamma-ray energies ( $E_\gamma$ ),  $R_{DCO}$  ratios, linear polarization anisotropy  $A_p$ , and multipolarity assignments of transitions depopulating the rotational levels in  $^{163}\text{Yb}$ .

E-levels (keV)	$E_\gamma$ (keV)	$J_i^\pi \rightarrow J_f^\pi$	$R_{DCO}$	$A_p$	Multi.	Band
Band 5						
133.1	80	$7/2^- \rightarrow 5/2^-$	) <sup>a</sup>	) <sup>b</sup>	) <sup>c</sup>	5→2
394.4	160.3	$11/2^- \rightarrow 9/2^-$	0.411(128)	) <sup>b</sup>	) <sup>c</sup>	5→2
394.4	262	$11/2^- \rightarrow 7/2^-$	1.010(19)	0.305(72)	E2	5
767.8	240.6	$15/2^- \rightarrow 13/2^-$	) <sup>a</sup>	) <sup>b</sup>	) <sup>c</sup>	5→Yrast
767.8	373.4	$15/2^- \rightarrow 11/2^-$	1.253(212)	0.183(142)	E2	5
767.8	414.4	$15/2^- \rightarrow 17/2^+$	) <sup>a</sup>	-0.163(68)	) <sup>c</sup>	5
767.8	599	$15/2^- \rightarrow 13/2^+$	) <sup>a</sup>	) <sup>b</sup>	) <sup>c</sup>	5→Yrast
1214.7	446.7	$19/2^- \rightarrow 15/2^-$	1.053(94)	0.384(129)	E2	5
1214.7	498.3	$19/2^- \rightarrow 21/2^+$	0.639(173)	) <sup>b</sup>	) <sup>c</sup>	5→Yrast
1214.7	843.5	$19/2^- \rightarrow 17/2^+$	0.759(65)	0.107(177)	E1	5→Yrast
1687.6	473	$23/2^- \rightarrow 19/2^-$	1.100(39)	0.038(181)	E2	5
1687.6	511	$23/2^- \rightarrow 25/2^+$	0.432(269)	) <sup>b</sup>	) <sup>c</sup>	5→Yrast
1687.6	971	$23/2^- \rightarrow 21/2^+$	0.665(58)	0.184(68)	E1	5→ Yrast
2168.3	349.2	$27/2^- \rightarrow 25/2^-$	) <sup>a</sup>	) <sup>b</sup>	) <sup>c</sup>	5→2
2168.3	480.7	$27/2^- \rightarrow 23/2^-$	1.088(69)	0.412(109)	E2	5
2168.3	988.4	$27/2^- \rightarrow 25/2^+$	) <sup>a</sup>	) <sup>b</sup>	) <sup>c</sup>	5→Yrast
2655.8	487.5	$31/2^- \rightarrow 27/2^-$	1.054(55)	0.328(197)	E2	5
2655.8	836.7	$31/2^- \rightarrow 25/2^-$	) <sup>a</sup>	) <sup>b</sup>	) <sup>c</sup>	5→2
2655.8	919.2	$31/2^- \rightarrow 29/2^+$	0.798(199)	) <sup>b</sup>	) <sup>c</sup>	5→Yrast
3195.2	539.6	$35/2^- \rightarrow 31/2^-$	1.084(53)	0.416(98)	E2	5
3195.2	828.3	$35/2^- \rightarrow 33/2^+$	0.896(169)	) <sup>b</sup>	) <sup>c</sup>	5→Yrast
3805.7	610.5	$39/2^- \rightarrow 35/2^-$	0.948(250)	0.332(131)	E2	5
4506.7	700.9	$43/2^- \rightarrow 39/2^-$	0.959(33)	0.037(177)	E2	5

)<sup>a</sup> insufficient statistics to measure DCO ratios.

)<sup>b</sup> insufficient statistics to measure linear polarization Anisotropy.

)<sup>c</sup> multipolarity could not be determined

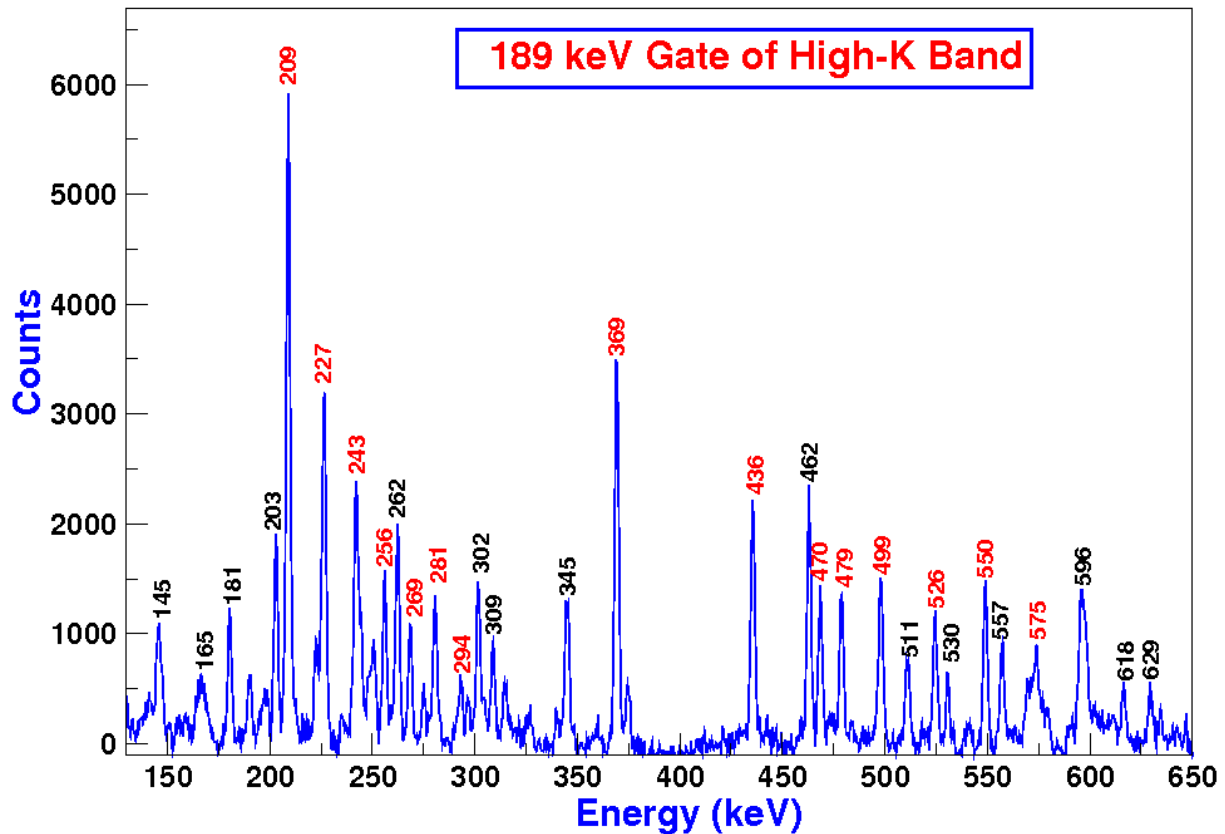
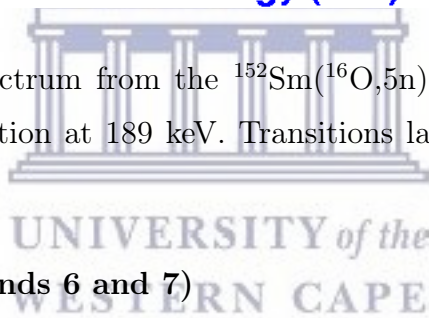


Figure 46: Coincidence spectrum from the  $^{152}\text{Sm}(^{16}\text{O},5n)^{163}\text{Yb}$  reaction obtained by setting a gate on the transition at 189 keV. Transitions labelled in red belong to the high-K band.



#### 4.2.8 High-K Band (Bands 6 and 7)

A new strongly coupled band, based on the 603.4 keV level, has been established for the first time in the current work. This structure decays mainly to the yrast band via the 369 and 479 keV transitions. These inter-band transitions are too weak (intensity) for DCO and polarization measurements, we therefore could not use these techniques to assign spins and parities to band members of these new rotational structures. As a result, we had to rely on other physics arguments, which are discussed in the following chapter. The table of gamma-rays and spectrum which confirms the existence of these band structures in this work are shown in Table 9 and Figure 46.



Table 9: Energy levels, gamma-ray energies ( $E_\gamma$ ),  $R_{DCO}$  ratios, linear polarization anisotropy  $A_p$ , and multipolarity assignments for transitions in  $^{163}\text{Yb}$  decay scheme.

E-levels (keV)	$E_\gamma$ (keV)	$J_i^\pi \rightarrow J_f^\pi$	$R_{DCO}$	$A_p$	Multi.	Band
11/2 <sup>-</sup> Bands 6 and 7						
603.4	369	11/2 <sup>-</sup> → 9/2 <sup>-</sup>	0.626(121)	) <sup>b</sup>	) <sup>c</sup>	7 → 2
603.4	479	11/2 <sup>-</sup> → 9/2 <sup>+</sup>	) <sup>a</sup>	) <sup>b</sup>	) <sup>c</sup>	7 → Yrast
792.6	189	13/2 <sup>-</sup> → 11/2 <sup>-</sup>	0.502(108)	) <sup>b</sup>	) <sup>c</sup>	6 → 7
1001.7	209	15/2 <sup>-</sup> → 13/2 <sup>-</sup>	0.618(103)	) <sup>b</sup>	) <sup>c</sup>	7 → 6
1001.7.1	398	15/2 <sup>-</sup> → 11/2 <sup>-</sup>	) <sup>a</sup>	) <sup>b</sup>	) <sup>c</sup>	7
1228.1	226	17/2 <sup>-</sup> → 15/2 <sup>-</sup>	0.686(73)	) <sup>b</sup>	) <sup>c</sup>	6 → 7
1228.1	436	17/2 <sup>-</sup> → 13/2 <sup>-</sup>	) <sup>a</sup>	) <sup>b</sup>	) <sup>c</sup>	6
1470.5	242	19/2 <sup>-</sup> → 17/2 <sup>-</sup>	) <sup>a</sup>	) <sup>b</sup>	) <sup>c</sup>	7 → 6
1470.5	469	19/2 <sup>-</sup> → 15/2 <sup>-</sup>	) <sup>a</sup>	) <sup>b</sup>	) <sup>c</sup>	7
1726.4	256	21/2 <sup>-</sup> → 19/2 <sup>-</sup>	0.737(342)	) <sup>b</sup>	) <sup>c</sup>	6 → 7
1726.4	498	21/2 <sup>-</sup> → 17/2 <sup>-</sup>	1.129(102)	) <sup>b</sup>	) <sup>c</sup>	6
1995.1	269	23/2 <sup>-</sup> → 21/2 <sup>-</sup>	) <sup>a</sup>	) <sup>b</sup>	) <sup>c</sup>	7 → 6
1995.1	525	23/2 <sup>-</sup> → 19/2 <sup>-</sup>	) <sup>a</sup>	) <sup>b</sup>	) <sup>c</sup>	7
2275.4	280	25/2 <sup>-</sup> → 23/2 <sup>-</sup>	0.513(260)	) <sup>b</sup>	) <sup>c</sup>	6 → 7
2275.4	550	25/2 <sup>-</sup> → 21/2 <sup>-</sup>	1.027(212)	) <sup>b</sup>	) <sup>c</sup>	6
2569.4	294	27/2 <sup>-</sup> → 25/2 <sup>-</sup>	0.682(75)	) <sup>b</sup>	) <sup>c</sup>	7 → 6
2569.4	574	27/2 <sup>-</sup> → 23/2 <sup>-</sup>	) <sup>a</sup>	) <sup>b</sup>	) <sup>c</sup>	7

)<sup>a</sup> insufficient statistics to measure DCO ratios.

)<sup>b</sup> insufficient statistics to measure linear polarization Anisotropy.

)<sup>c</sup> multipolarity could not be determined

## Chapter 5

### 5 Discussion

Figures 47 and 48 respectively show the alignments  $i$  and Routhians  $e'$  plots (as a function of frequency  $\omega$ ), experimentally deduced for rotational structures observed in  $^{163}\text{Yb}$ . Harris parameterization with values  $\mathcal{J}_0 = 23\hbar^2.\text{MeV}^{-1}$  and  $\mathcal{J}_1 = 90\hbar^4.\text{MeV}^{-3}$  [5] have been used in both plots and they were adopted from previous in-beam studies [5]. In a quest to meaningfully describe the rotational properties of the majority of structures observed in the current work, the cranked shell model [5, 59, 58] has been used. Figures 49 and 50 respectively show the cranked shell model diagrams of  $^{162}\text{Yb}$  for both neutrons and protons [55]. These diagrams may also be used to explain the rotational properties of quasi-particle excitation in  $^{163}\text{Yb}$  because of the negligible differences in the Fermi surface of these two isotopes. The cranked shell model (CSM) calculations for the ground state band of  $^{162}\text{Yb}$  were performed with the following nuclear deformation parameters:  $\epsilon_2 = 0.212$ ,  $\epsilon_4 = -0.011$ . In  $^{162}\text{Yb}$ , the vacuum configuration correspond to  $Z = 70$  and  $N = 92$ . The Fermi level of the neutrons lie close to high-j  $i_{13/2}$  and  $h_{9/2}$ , low-j  $2f_{7/2}$  orbital, while the one for the protons lie close to high-j  $h_{11/2}$  and low-j  $g_{7/2}$ ,  $2d_{5/2}$ ,  $2d_{3/2}$  orbitals.

In CSM all quasi-particle Routhians are calculated relative to the vacuum configuration defined as the lowest configuration for even-even nucleus with positive parity  $\pi = +1$ , and signature  $\alpha = 0$ . In principle, for the vacuum configuration, all the Routhians with  $e'(\omega = 0) < 0$ , remain occupied. Table 10 shows the convention used for labelling of quasi-neutron states in Figure 49. Similarly, Table 11 shows the labelling convention used for quasi-protons in Figure 50. Figure 49 clearly shows the positive energy Routhians for neutrons and they are labelled with letters A, B, C etc., while for protons they are labelled with a, b, c, etc. In the CSM quasi-neutron Routhian plot of  $^{163}\text{Yb}$ , the lowest positive energy Routhian (A) will be occupied, while that of its complex conjugate ( $A^+$ ) will be empty. The  $A(+,+1/2)$  and  $B^+(+,+1/2)$  Routhians come close, interact and exchange their wave function properties at a rotational frequency of  $\omega/\omega_0 = 0.027 \omega$ . This phenomenon is called the AB band crossing and it corresponds to the experimental alignment of two neutron pairs of the  $i_{13/2}$  orbital. Similarly, the CSM calculations can be used to predict the band crossings associated with the alignments of the second (BC) and/

or the third (AD) neutron pairs of the  $i_{13/2}$  orbital in the frequency range between  $\sim 0.3$  and  $\sim 0.4$  MeV, see Figure 49. Similarly, at higher frequencies, these kind of alignments can also be deduced for band crossings associated with the first (ab), second (bc) and third (ad) pairs of the  $h_{11/2}$  proton orbitals. In  $^{163}\text{Yb}$  the  $5/2^+[642]$  neutron orbital becomes low in energy compared to the  $3/2^+[651]$  orbital [5]. In the context of the CSM formalism, the A(+,+) and B(+,+) letters, previously assigned to signature partners of Routhians belonging to the  $3/2^+[651]$  orbital in the  $N = 91$  nuclei, can now be assigned to Routhian trajectories associated with the  $5/2^+[642]$  orbital since they carry the highest alignments when compared to other Routhians- including those that originate from the  $3/2^+[651]$  neutron orbital.



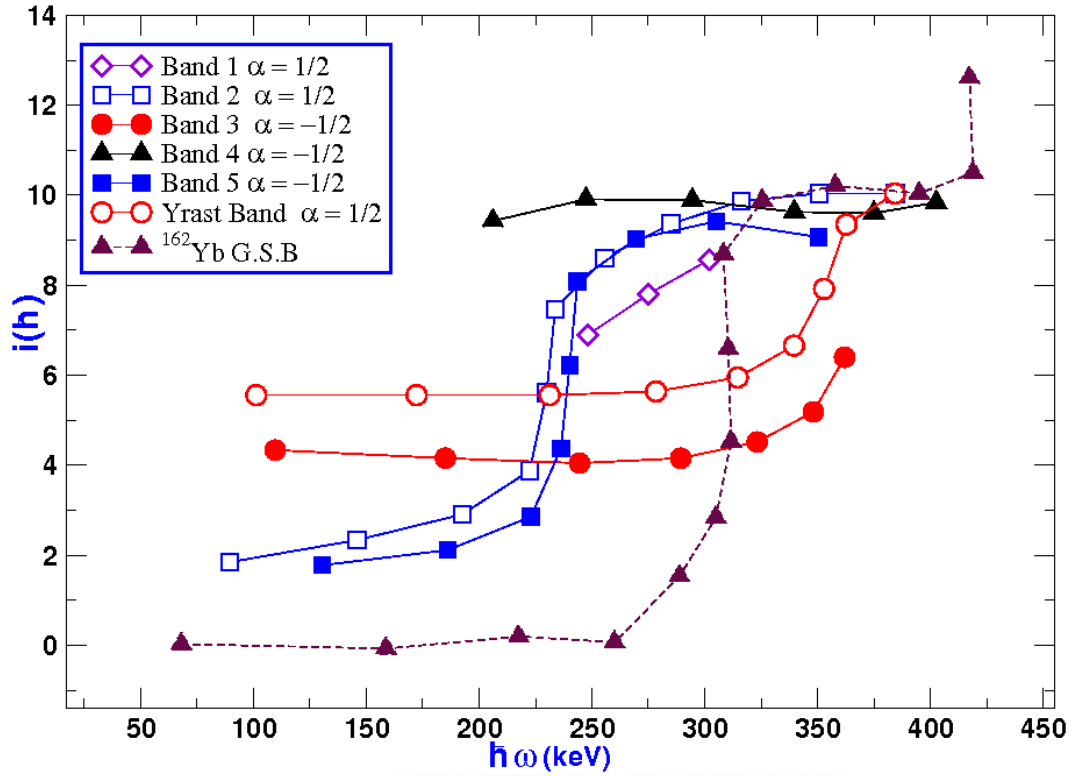


Figure 47: Alignments deduced for bands in  $^{163}\text{Yb}$  as function of  $\hbar\omega$  in the current work. The labels in the legends indicate the bands as they are labelled in Figure 35. The reference parameters are chosen to be  $\mathcal{J}_0 = 23\hbar^2.\text{MeV}^{-1}$  and  $\mathcal{J}_1 = 90\hbar^4.\text{MeV}^{-3}$  for  $^{163}\text{Yb}$ . The alignment for the ground state band of  $^{162}\text{Yb}$  is also shown for comparison. Here, Harris parameterization with values  $\mathcal{J}_0 = 20\hbar^2.\text{MeV}^{-1}$  and  $\mathcal{J}_1 = 90\hbar^4.\text{MeV}^{-3}$  are used for  $^{162}\text{Yb}$  [54].

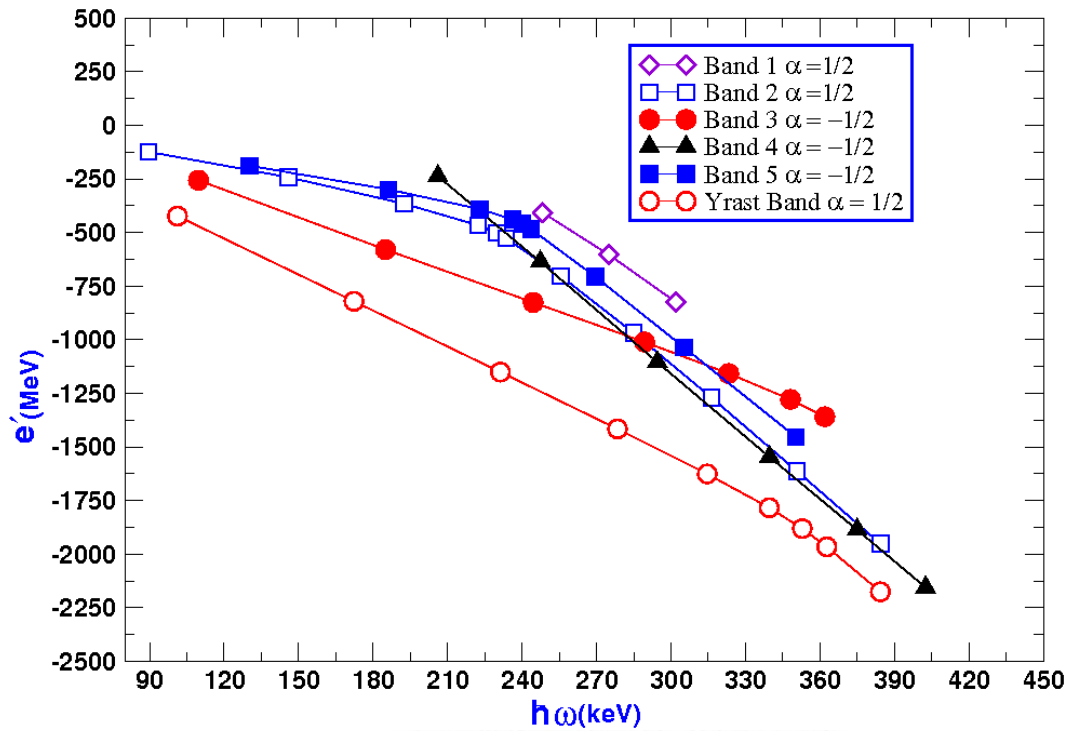


Figure 48: Experimental Routhians (single-particle energies in the rotating frame) plotted against rotational frequency,  $\hbar\omega$  for bands belonging to  $^{163}\text{Yb}$ . The Harris parameters used for the reference are  $\mathcal{J}_0 = 23\hbar^2.\text{MeV}^{-1}$  and  $\mathcal{J}_1 = 90\hbar^4.\text{MeV}^{-3}$ . Signature partner bands are labelled in the same colours. Open symbols denote positive signature and closed symbols represent negative signature.

Table 10: Convention for labelling the quasi-neutron orbitals shown in Figure 49.

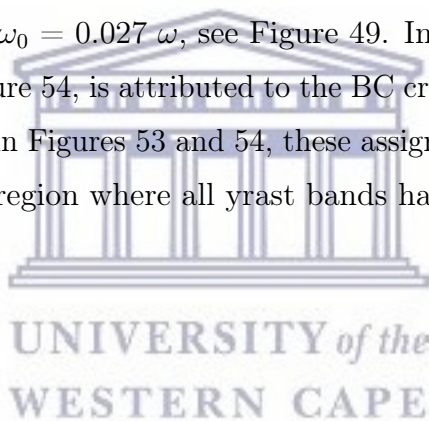
Odd neutron orbital		
CSM labels $(\pi, \alpha)$	shell model label	Nilsson label
A(+,+1/2)	$\nu i_{13/2}$	$5/2^+[642]$
B(+,-1/2)	$\nu i_{13/2}$	$5/2^+[642]$
C(+,+1/2)	$\nu i_{13/2}$	$3/2^+[651]$
D(+,-1/2)	$\nu i_{13/2}$	$3/2^+[651]$
E(-,+1/2)	$\nu h_{9/2}$	$3/2^- [521]$
F(-,-1/2)	$\nu h_{9/2}$	$3/2^- [521]$
G(-,-1/2)	$\nu h_{9/2}$	$5/2^- [523]$
H(-,+1/2)	$\nu h_{9/2}$	$5/2^- [523]$

Table 11: Convention for labelling the quasi-proton orbitals shown in Figure 50.

Proton orbital		
CSM labels $(\pi, \alpha)$	shell model label	Nilsson label
a(+,+1/2)	$\pi d_{3/2}$	$1/2^+[411]$
b(+,-1/2)	$\pi d_{3/2}$	$1/2^+[411]$
c(+,+1/2)	$\pi g_{7/2}$	$7/2^+[404]$
d(+,-1/2)	$\pi g_{7/2}$	$7/2^+[404]$
e(-,-1/2)	$\pi h_{11/2}$	$7/2^- [523]$
f(-,+1/2)	$\pi h_{11/2}$	$7/2^- [523]$
g(-,-1/2)	$\pi h_{11/2}$	$9/2^- [514]$
h(-,+1/2)	$\pi h_{11/2}$	$9/2^- [514]$

## 5.1 The Positive Parity Bands: Yrast and Band 3

The CSM calculation shown in Figure 49 is consistent with the “yrast band” and band 3 being the favoured and unfavoured members/signatures of the  $5/2^+[642]$  state originating from the  $i_{13/2}$  neutron orbital. The CSM calculation also predicts the slope of both bands to be steepest in the rotating frame, and thus larger alignments. In fact, this is evident in the alignments values of  $\sim 6 \hbar$  and  $4.5 \hbar$ , which have been experimentally (from Figure 53 and 54) deduced for both the yrast band and band 3, respectively. This is in agreement with  $5 \hbar$  and  $4 \hbar$ , which are values that have been predicted by CSM, at about 0.323 MeV, for both bands, respectively. According to the convention used in Table 10, the yrast band and band 3 can also be understood as A and B. It is worth noting that the AB band crossing (mentioned above) is blocked in  $^{163}\text{Yb}$  because A and B Routhians are both occupied. In fact, the first possible band crossing is the BC crossing and it occurs at a rotational frequency of  $\omega/\omega_0 = 0.027 \omega$ , see Figure 49. In fact the gradual alignment observed at 0.35 MeV, in Figure 54, is attributed to the BC crossing predicted by the CSM calculations. As can be seen in Figures 53 and 54, these assignments are also in agreement with the systematics of the region where all yrast bands have a signature partner with relatively higher alignments.





## 5.2 The Negative Parity Bands 2 and 5

Band 2 is well known from previous studies and has been assigned as the even spin member of the  $3/2^-$ [521] Nilsson that originates from the  $h_{9/2}$  neutron spherical shell model [5, 6]. On the other hand, band 5 is a relatively new structure established in this work. As can be seen in Figure 35, the first three low-lying band members of this band are known from the previous in-beam works and they were assumed to be due to the  $3/2^-$ [521] neutron orbital [6], thus making it a candidate for the odd-spin partner of band 2. Numerous levels that have been added on this band, in the current work, have made it possible for us to confirm the quasi-particle configuration of this structure using the CSM. In fact, cranked shell model calculations performed in this work are consistent with both bands 2 and 5 being built on the  $3/2^-$ [521] orbital as suggested by former studies [5, 6]. As can be seen in Figure 53, the order of appearance and slopes of Routhians corresponds to the  $3/2^-$ [521] configuration, namely bands 2 and 5 are as predicted in Figure 49. The alignments deduced experimentally for both bands 2 and 5, which are  $\sim 2.5 \hbar$  and  $2 \hbar$ , are also in agreement with  $\sim 3 \hbar$  and  $2.3 \hbar$ , which are alignments that have been predicted by the CSM calculation for both bands 2 and 5, respectively.

In order to understand our findings in the context of the systematics of the region, we consider the excitation energies (minus the rigid rotor) for the  $3/2^-$ [521] candidates in  $^{163}\text{Yb}$  and we compare them with those in the neighbouring odd-N isotones namely,  $^{157}\text{Gd}$ ,  $^{159}\text{Dy}$  and  $^{161}\text{Er}$  (see Figure 52). These plots clearly show that we are dealing with the same structure. In fact, the similarities become more apparent with increase in proton number. Firstly, the  $3/2^-$ [521] candidates start at 0 keV and have signature partners in all four cases. In all cases, signature partners track each other as a function of spin with minimal signature splitting. Figures 52 and 54 also show that these bands have the same moment of inertia in all four cases. The odd spin sequence is relatively higher for odd spin signatures in all four cases. At high spin, there is a common crossing between the odd spin signature of the  $5/2^+$ [642] and  $3/2^-$ [521] bands, particularly in  $^{159}\text{Dy}$ ,  $^{161}\text{Er}$ , and  $^{163}\text{Yb}$ . This crossing takes place between 14-18  $\hbar$ .

Furthermore, numerous  $J \rightarrow (J \pm 1)$  transitions have been established (between the  $3/2^-$ [521] and  $5/2^+$ [642] orbitals) as a result of massive extensions that have been made on the odd spin signature candidate of the  $3/2^-$ [521] neutron orbital, see Figure 35. These

relatively strong  $J \rightarrow (J \pm 1)$  transitions have also been reported in the neighbouring odd-N nuclei [58, 60]. Figure 55 shows the  $B(E1)/B(E2)$  branching ratios for the aforementioned transitions in  $^{163}\text{Yb}$  and they are compared with those in  $^{159}\text{Dy}$  and  $^{161}\text{Er}$ . This figure clearly shows that the branching ratio for these transitions are within the same order of magnitude. This therefore gives us confidence that we are dealing with the same structure and that the newly established band 5 belongs to the  $3/2^- [521]$  configuration. Band 5 is therefore the first odd spin candidate for the  $3/2^- [521]$  state to be observed beyond band crossing for Yb isotopes in the 160 to 170 mass region. According to the notation used in Table 10, bands 5 and 2 can therefore be assigned to quasi-particle configurations E and F, respectively.



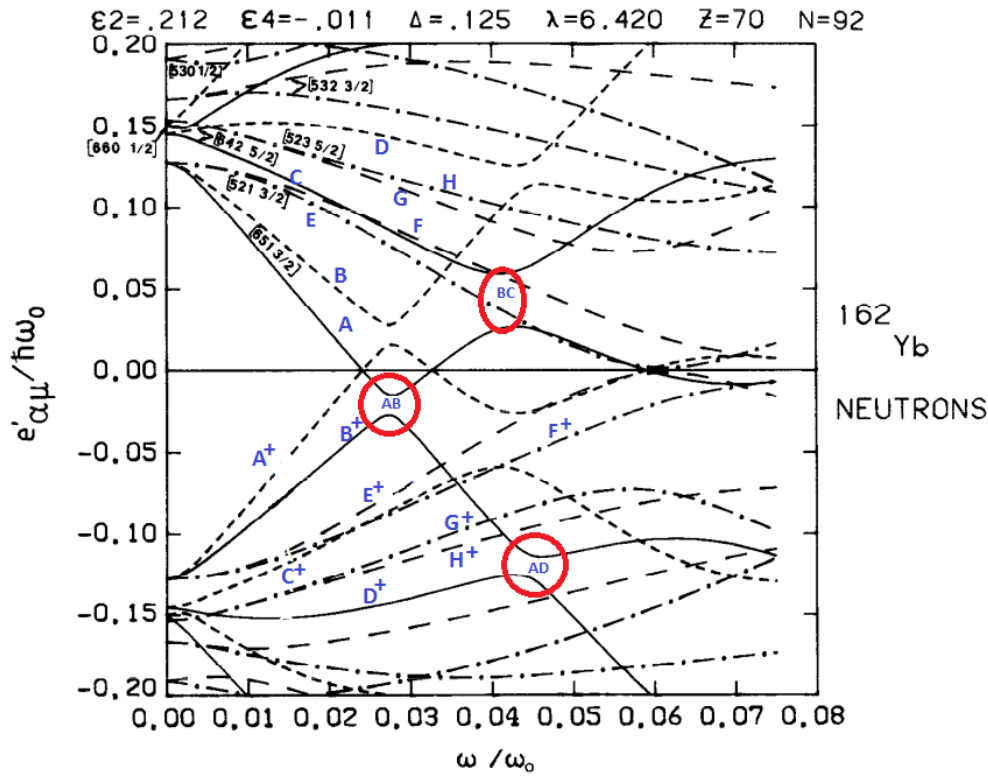


Figure 49: cranked shell model diagram of quasi-particle routhians for  $^{162}\text{Yb}$  neutrons. The rotational frequency in this diagram denoted by  $\omega/\omega_0$ , is expressed in units of the oscillator frequency  $\omega_0$ . The quasi-particle routhians, are expressed in units of the harmonic oscillator energy  $\hbar\omega_0$ . Full lines are used for quasi-particle trajectories with positive parity and signature  $\alpha = 1/2$ , that is  $(+,1/2)$ . Short-dashed lines are used for quasi-particle trajectories with positive parity and signature  $\alpha = -1/2$ , that is  $(+,-1/2)$ . Dot-dashed lines are used for quasi-particle trajectories with negative parity and signature  $\alpha = 1/2$ , that is  $(-,1/2)$ . Long-dashed lines are used for quasi-particle trajectories with negative parity and signature  $\alpha = -1/2$ , that is  $(-,-1/2)$  [55]. The labelling convention used for the Routhian energies shown in the plot are given in Table 10.

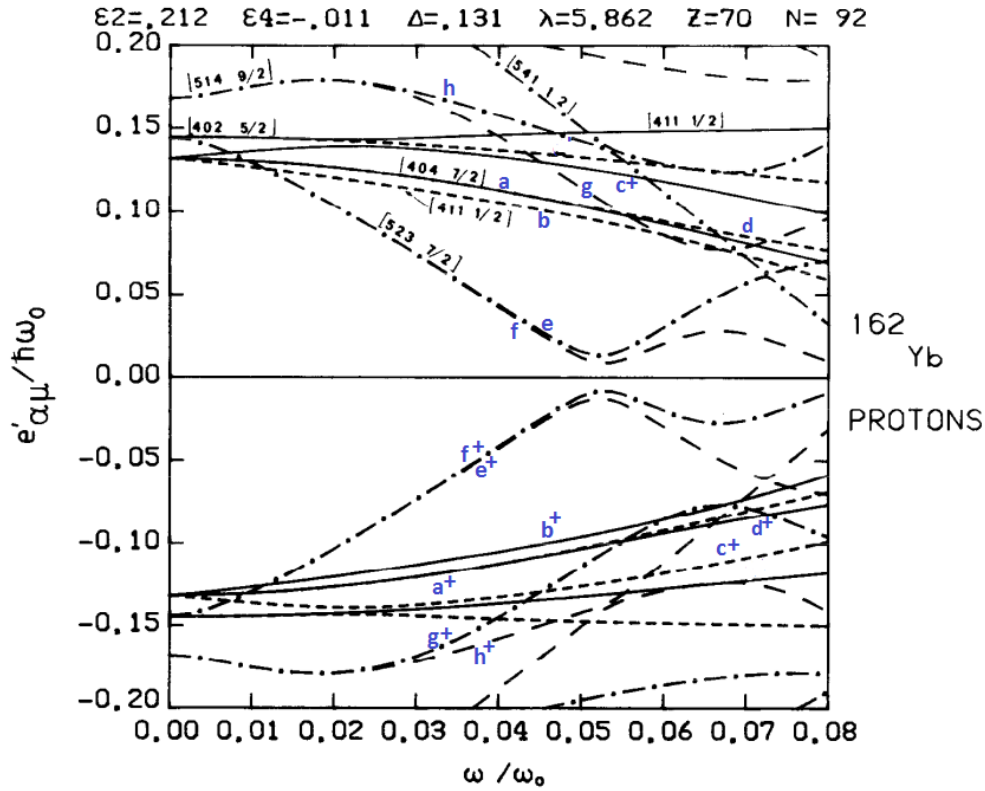


Figure 50: cranked shell model diagram of quasi-particle routhians for  $^{162}\text{Yb}$  protons. The rotational frequency in this diagram denoted by  $\omega/\omega_0$ , is expressed in units of the oscillator frequency  $\omega_0$ . The quasi-particle routhians, are expressed in units of the harmonic oscillator energy  $\hbar\omega_0$ . Full lines are used for quasi-particle trajectories with positive parity and signature  $\alpha = 1/2$ , that is  $(+, 1/2)$ . Short-dashed lines are used for quasi-particle trajectories with positive parity and signature  $\alpha = -1/2$ , that is  $(+, -1/2)$ . Dot-dashed lines are used for quasi-particle trajectories with negative parity and signature  $\alpha = 1/2$ , that is  $(-, 1/2)$ . Long-dashed lines are used for quasi-particle trajectories with negative parity and signature  $\alpha = -1/2$ , that is  $(-, -1/2)$  [55]. The labelling convention used for the Routhian energies shown in the plot are given in Table 11.

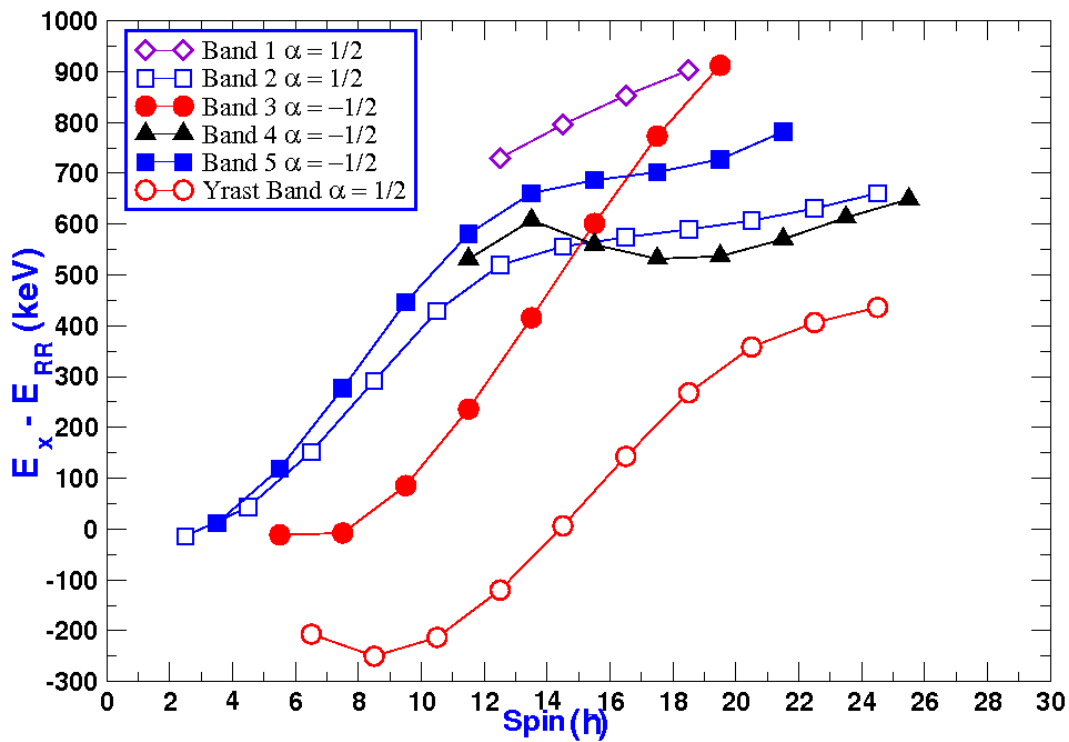


Figure 51: A plot of experimental excitation energies minus a rigid rotor for all bands in  $^{163}\text{Yb}$ . Open symbols denote positive signature and closed symbols represent negative signature.

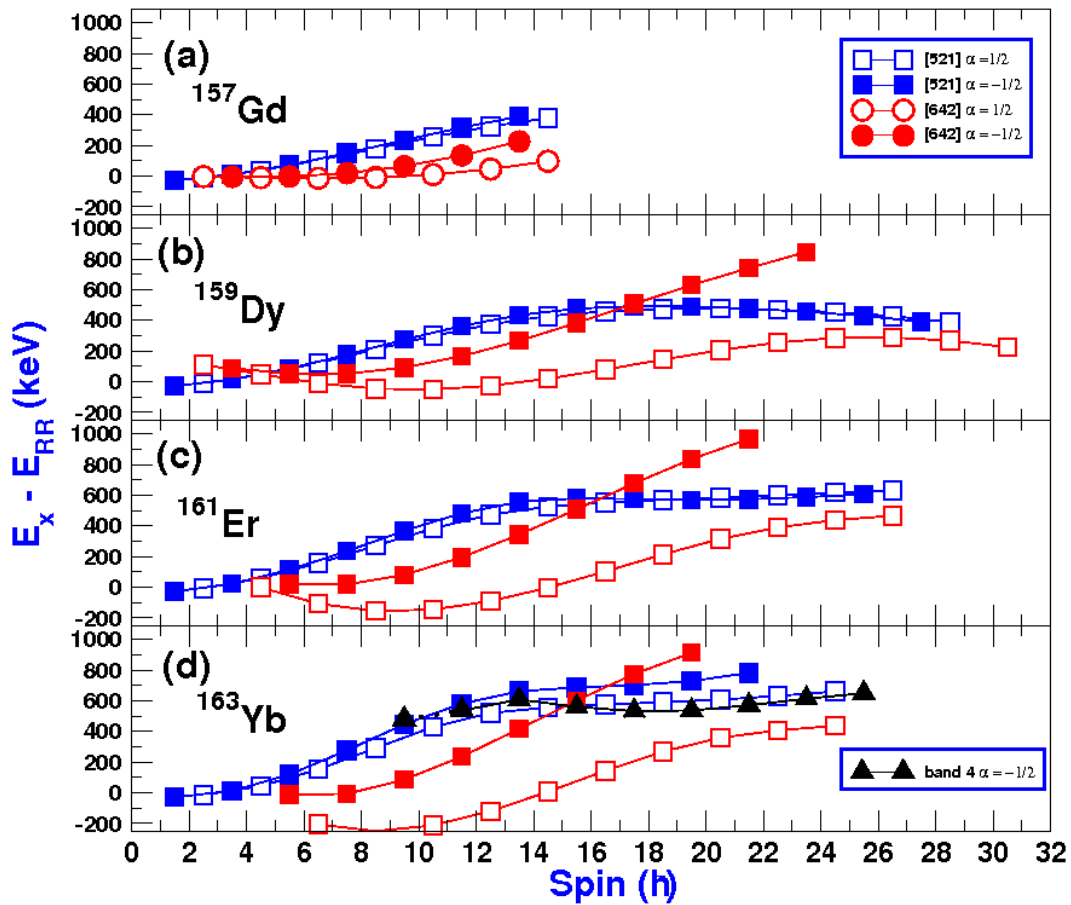


Figure 52: Compilation of experimental excitation energies minus a rigid rotor for the  $3/2^- [521]$  and  $5/2^+ [642]$  signature partner bands in  $^{157}\text{Gd}$  [58],  $^{159}\text{Dy}$  [59],  $^{161}\text{Er}$  [5], and  $^{163}\text{Yb}$ . The addition of band 4 in  $^{163}\text{Yb}$  is to show the signature inversion around  $10 \hbar$ . Signature partner bands are labelled in the same colours. Open symbols denote positive signature and closed symbols represent negative signature.

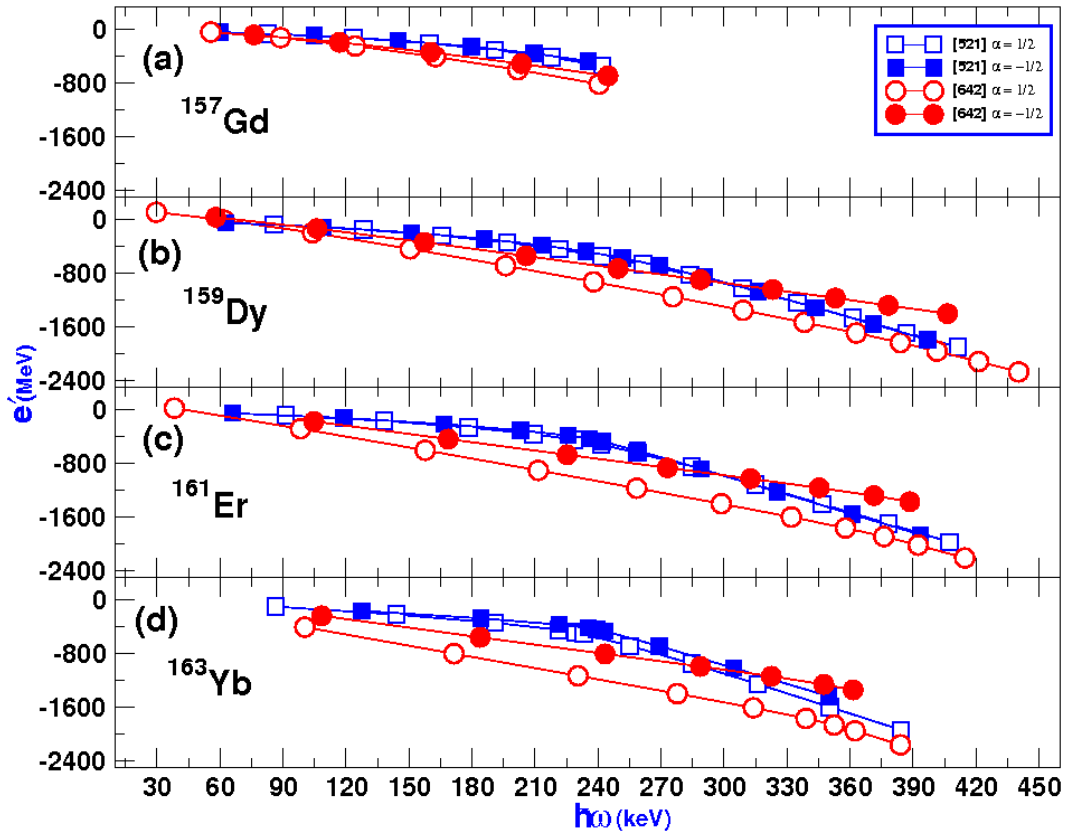


Figure 53: Compilation of Routhian plots for the  $3/2^- [521]$  and  $5/2^+ [642]$  signature partner bands in  $^{157}\text{Gd}$ ,  $^{159}\text{Dy}$ ,  $^{161}\text{Er}$ , and  $^{163}\text{Yb}$ . The Harris parameters for  $^{157}\text{Gd}$ :  $\mathcal{J}_0 = 27.3\hbar^2.\text{MeV}^{-1}$  and  $\mathcal{J}_1 = 256.6\hbar^4.\text{MeV}^{-3}$ ,  $^{159}\text{Dy}$ :  $\mathcal{J}_0 = 28\hbar^2.\text{MeV}^{-1}$  and  $\mathcal{J}_1 = 110\hbar^4.\text{MeV}^{-3}$ ,  $^{161}\text{Er}$ :  $\mathcal{J}_0 = 26\hbar^2.\text{MeV}^{-1}$  and  $\mathcal{J}_1 = 90\hbar^4.\text{MeV}^{-3}$ , and  $^{163}\text{Yb}$ :  $\mathcal{J}_0 = 23\hbar^2.\text{MeV}^{-1}$  and  $\mathcal{J}_1 = 90\hbar^4.\text{MeV}^{-3}$ . Signature partner bands are labelled in the same colours. Open symbols denote positive signature and closed symbols represent negative signature.

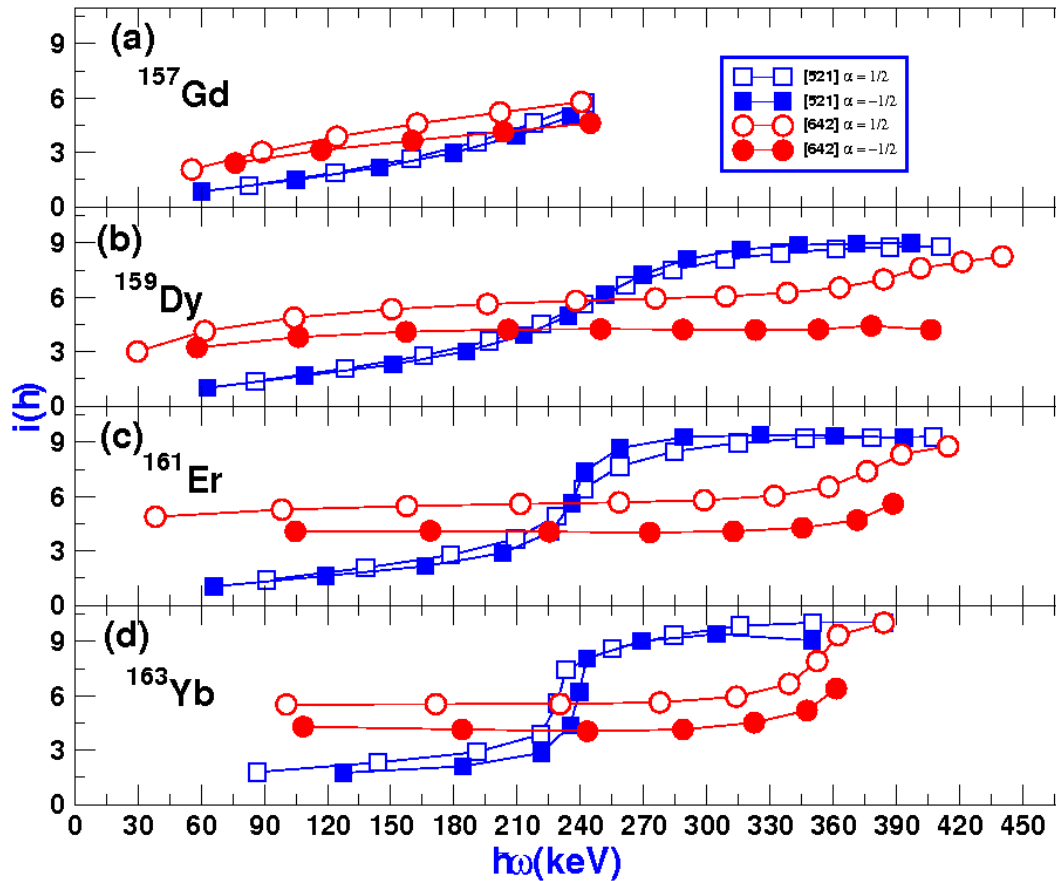


Figure 54: Compilation of spin alignment plots for the  $3/2^-$ [521] and  $5/2^+$ [642] signature partner bands in  $^{157}\text{Gd}$ ,  $^{159}\text{Dy}$ ,  $^{161}\text{Er}$ , and  $^{163}\text{Yb}$ . The Harris parameters for  $^{157}\text{Gd}$ :  $\mathcal{J}_0 = 27.3\hbar^2.\text{MeV}^{-1}$  and  $\mathcal{J}_1 = 256.6\hbar^4.\text{MeV}^{-3}$  [60],  $^{159}\text{Dy}$ :  $\mathcal{J}_0 = 28\hbar^2.\text{MeV}^{-1}$  and  $\mathcal{J}_1 = 110\hbar^4.\text{MeV}^{-3}$ ,  $^{161}\text{Er}$ :  $\mathcal{J}_0 = 26\hbar^2.\text{MeV}^{-1}$  and  $\mathcal{J}_1 = 90\hbar^4.\text{MeV}^{-3}$ , and  $^{163}\text{Yb}$ :  $\mathcal{J}_0 = 23\hbar^2.\text{MeV}^{-1}$  and  $\mathcal{J}_1 = 90\hbar^4.\text{MeV}^{-3}$ . Signature partner bands are labelled in the same colours. Open symbols denote positive signature and closed symbols represent negative signature.



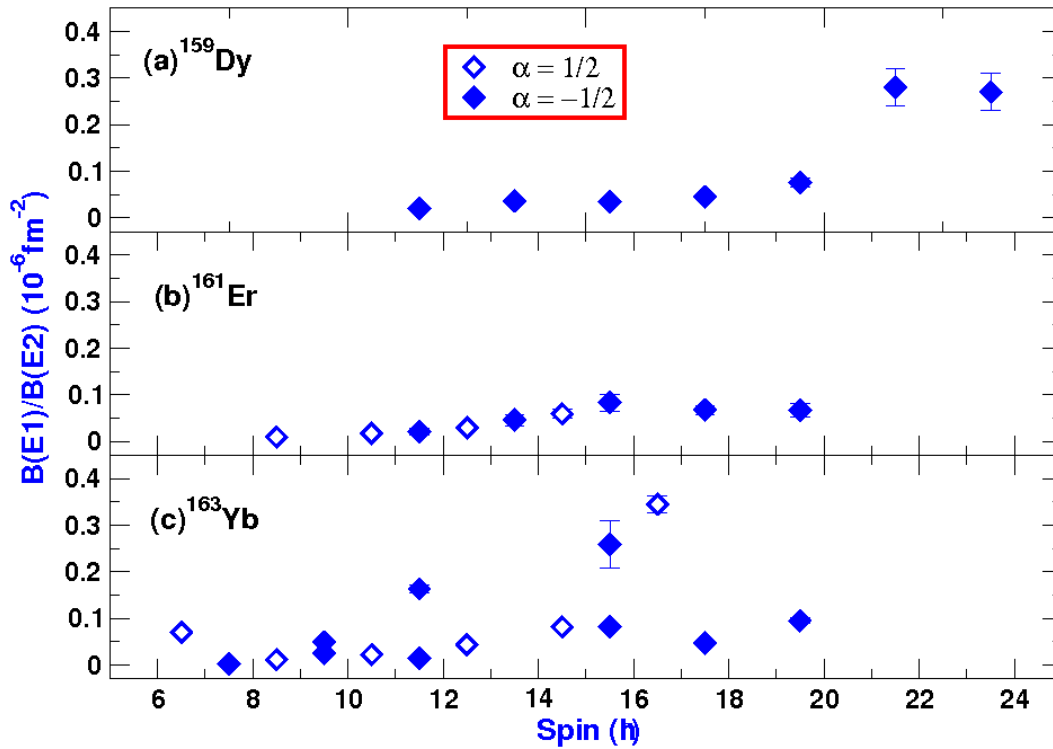


Figure 55: Compilation of  $B(E1)/B(E2)$  ratios as a function of spin for  $3/2^- [521]$  bands in  $^{161}\text{Yb}$ ,  $^{159}\text{Dy}$  and in  $^{163}\text{Yb}$ .

In the present work, the strong E1 transitions from the  $3/2^- [521]$  band to the  $5/2^+ [642]$  band have been observed in  $^{163}\text{Yb}$ . In fact, the occurrence of relatively enhanced E1 transitions is a general phenomenon in the rare-earth region. The enhanced E1 transitions between two bands with opposite parities are observed in batch of odd-A nuclei [59]. The measured  $B(E1)/B(E2)$  ratios for the  $^{163}\text{Yb}$  nucleus are comparable with those observed in the neighbouring nuclei  $^{159}\text{Dy}$  [58], and  $^{161}\text{Er}$  [59]. The measured  $B(E1)/B(E2)$  ratios for the decay of states with negative signature are systematically lower than the ones with positive signature states (see Figure 55).

### 5.3 Band 4

Kownacky *et al.*, [5] proposed that for the lowest negative-parity bands a small positive splitting is observed at low rotational frequency ( $\hbar\omega$ ), that is band 2 is lowered in energy relative to band 2. At larger  $\hbar\omega$  a small negative decoupling is observed (band 4 lies lower in energy than band 2). This is also confirmed in the current work (see Figure 48).

### 5.4 High-K Bands (Bands 6 and 7)

A pair of strongly coupled bands with strong M1 transitions has been established in this study. In a search for a microscopic identity of these bands, we consider the possible ways through which they can be formed. The band-head of this high-K structure is at about 600 keV. This suggests that these bands are likely to be built on a single-particle orbital. In the Nilsson and cranked shell models, the most obvious candidate that better fits the description of a high-K negative parity sequence with a  $K = 11/2^-$  band-head is the  $11/2^- [505]$  neutron orbital.

Indeed, this high-K structure appears to share a lot of similarities with  $K = 11/2^-$  bands built on the  $11/2^- [505]$  neutron orbital that have been identified in the neighbouring  $N = 93$  isotones. Firstly, these bands show no signature splitting (see Figure 56), and this is consistent with the behaviour of  $11/2^- [505]$  bands observed in adjacent neighbouring odd- $N$  nuclei. As can be seen in Figure 48, these bands also have the same moment of inertia. The strong M1 transitions (between bands 6 and 7) are also present in their neighbouring nuclei and are due to the fact that the microscopic configuration responsible for the formation of these bands involves a high-K orbit (with a higher magnetic moment) such as the  $11/2^- [505]$  neutron orbital. Further,  $B(M1)/B(E2)$  branching ratios have been deduced for these bands in  $^{163}\text{Yb}$ , see Figure 57 (a). These ratios show further similarities with those measured for  $^{159}\text{Dy}$  and  $^{163}\text{Er}$ , see Figure 57 (a), (b), and (c). In fact, in all three cases, the ratios are within the same order of magnitude. In addition, they are typically less than 2, and they decrease gradually as a function of spin. These pieces of information are consistent with the conjecture given above about the microscopic identity of bands 6 and 7 being built on the single-particle neutron  $11/2^- [505]$  Nilsson state. These finding mark the first observation of high-K structure to be reported in  $^{163}\text{Yb}$ .

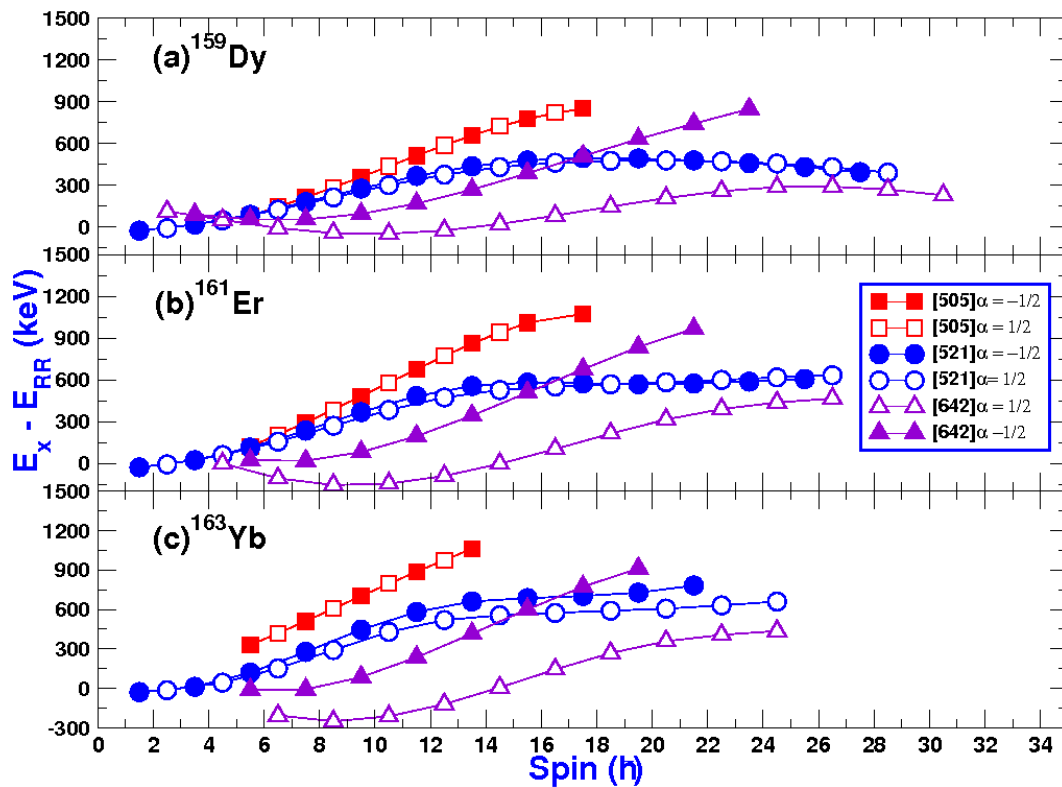


Figure 56: Compilation of the experimental excitation energies, minus the rigid rotor plots for the  $11/2^-$  [505],  $3/2^-$  [521] and  $5/2^+$  [642] signature partner bands in  $^{159}\text{Dy}$  [58],  $^{161}\text{Er}$  [59], and  $^{163}\text{Yb}$  [5]. The Signature partner bands are labelled in the same colours. Open symbols denote positive signature and closed symbols represent negative signature.

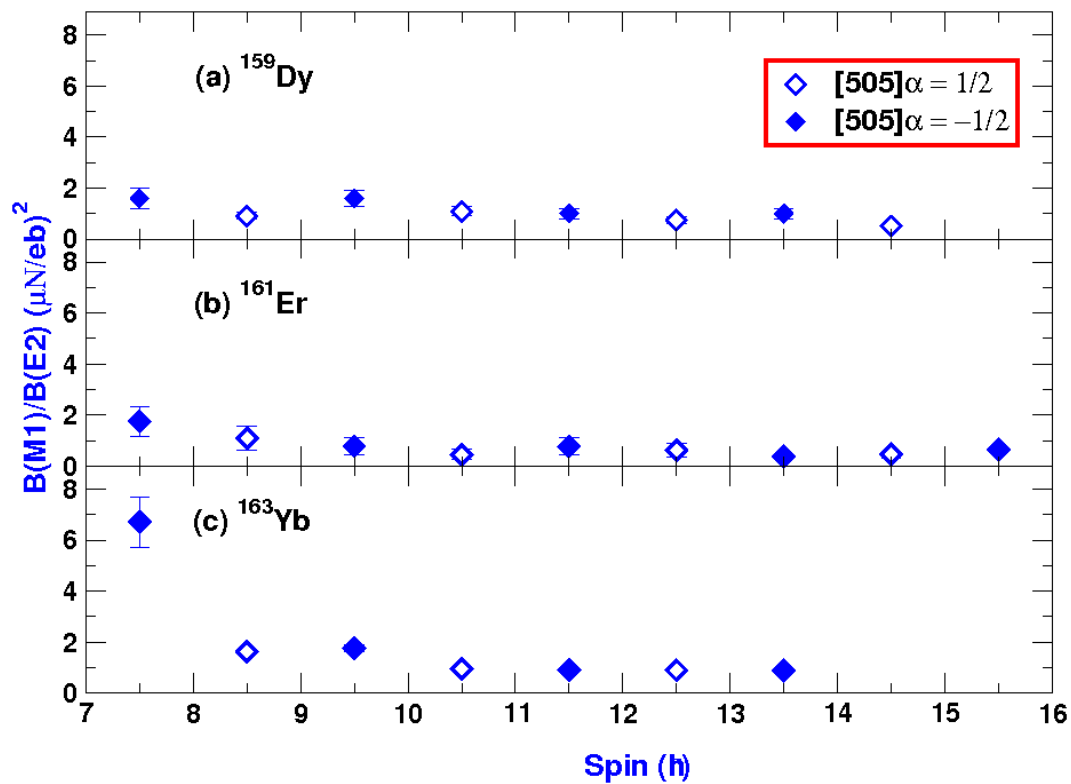


Figure 57: Compilation of  $B(M1)/B(E2)$  ratios as a function of spin for  $11/2^- [505]$  bands in  $^{163}\text{Yb}$ ,  $^{161}\text{Er}$ , and the  $11/2^- [505]$  bands in  $^{159}\text{Dy}$  [59, 58].

## Chapter 6

### 6 Conclusion

The nuclear structure of  $^{163}\text{Yb}$  has been studied in detail from low to medium spin. To understand the nuclear structure it is also necessary to interpret the experimental results in terms of a model. The cranked shell model was used for comparison of experimental data in this work. After a comprehensive analysis, the level scheme of  $^{163}\text{Yb}$  has been extended with fragments of about 3 new rotational bands. In fact, bands 5, 6 and 7 are as a result of findings from this work. The spins and parities of new and well established rotational structures, established in previous in-beam works, have been successfully assigned using DCO and polarization measurements. In order to meaningfully describe the rotational properties of structures observed in this work, the Nilsson and cranked shell models have been used. In some of the cases, systematic comparisons have been made in order to understand the microscopic behaviour of some of the rotational structures observed in the nucleus of interest.

In summary, the newly established band 5 has been identified as the odd spin sequence of the  $3/2^- [521]$  neutron orbital or the ground state band. Thus, making this band the first odd spin candidate for the  $3/2^- [521]$  state to be observed beyond band crossing for odd-N Yb isotopes in the 160 to 170 mass region. Bands 6 and 7, also are new high-K structure established in the current work, have been identified as signature partners built on the  $11/2^- [505]$  single neutron configuration. These findings mark the first observation of a high-K structure to be reported in  $^{163}\text{Yb}$ . Overall, this study has been rich in spectroscopy. Despite this, one of the major objectives of this work was to observe the coupling of the single particle configuration in  $^{163}\text{Yb}$  to collective excitations of the neighbouring even-even core, namely  $^{162}\text{Yb}$  as has been the case for odd nucleon nuclide such as,  $^{155}\text{Gd}$ ,  $^{155}\text{Dy}$ ,  $^{157}\text{Dy}$ ,  $^{159}\text{Er}$ ,  $^{165}\text{Ho}$  and  $^{167}\text{Er}$ . This feature remains elusive in  $^{163}\text{Yb}$ . We therefore attribute the absence of this phenomenon due to the entry distribution of the reaction which did not favour the population of these states. In fact, the experiment analysed in this work used a beam projectile that brought in relatively higher angular momentum onto the system, and this makes the population of low-lying states to be at a minimal.

## 7 Future Plan

For our future studies, we would like to carry on the analysis of this nucleus, also the neighbouring nucleus  $^{164}\text{Yb}$ . We would like to conduct an experiment for measurements of life-time of the  $11/2^- [505]$  bandhead. These measurements could be done with the recently aquired  $2'' \times 2''$  LaBr<sub>3</sub>:Ce detectors. We would like to search for other  $11/2^- [505]$  structures in other Yb nuclei. Do further experiments to study the systematics of the collective excited  $K = 0$  and  $K = 2$  bands in the Yb isotopes.



## 8 References

### References

- [1] G. Gervais *et al.*, Nucl. Phys. A624, 257 (1997)
- [2] M. Lipoglavsek, Nucl. Inst. Meth. Phys. Res. A361, 297 (1995)
- [3] J.F. Sharpey-Schafer *et al.*, Eur. Phys. J. A47, 5 (2011)
- [4] J.F. Sharpey-Schafer *et al.*, Eur. Phys. J. A47, 6 (2011)
- [5] J. Kownacky *et al.*, Nucl. Phys. A394, 269 (1983)
- [6] L. Richter, Z. Phys. A290, 213 (1979)
- [7] V.K. Mittal and R.C. Verma, Introduction to Nuclear and Particle Physics, 2nd edition (Prentice-Hall of India Pvt.Ltd, 2011)
- [8] K.S. Krane, Introductory Nuclear Physics, (John Wiley & Sons, 1988).
- [9] <http://www2.lbl.gov/abc/wallchart/guide.html>
- [10] G.J. Aubrecht *et al.*, The Nuclear Science Wall Chart, The Physics Teacher 35, 544 (1997)
- [11] W. Pauli, Naturwissenschaft, 12, 741 (1924)
- [12] H.Schüler and T. Schmidt, Z. Phys. 94, 457 (1935)
- [13] N. Bohr, Nature 137, 344 (1936)
- [14] J.M. Arias and M. Lozano, An Advanced Course in Modern Nuclear Physics (Springer, 2001)

- [15] S.N.T. Majola, PhD thesis, University of Cape Town, (2015)
- [16] [ns.ph.liv.ac.uk/MTsort-manual/MTsort.html](http://ns.ph.liv.ac.uk/MTsort-manual/MTsort.html)
- [17] J. Lilley, Nuclear Physics, Principles and Applications, (John Wiley & Sons Ltd, 2001)
- [18] E.S. Paul, Postgraduate Lectures, Liverpool Nuclear Physics Group (2003)
- [19] S.G. Nilsson, Kong.Dan.Vid.Sel.Mat.Fys.Med. Binding States of Individual Nucleons in Strongly Deformed Nuclei 29N16 1-69 CERN-55-30 (1955)
- [20] J.M. Eisenberg and W. Greiner, Nuclear Theory, I, North Holland, Amsterdam, First edition, (1970)
- [21] B.R. Mottelson and S.G. Nilsson. Classification of the Nucleonic States in Deformed Nuclei. Phys. Rev. 99, 1615 (1955)
- [22] W. Greiner and J. Maruhn, Nuclear Models, (Springer, 1996)
- [23] G. K. Kumar, PhD thesis, The Maharaja Sayajirao University of Baroda (2008)
- [24] R.F. Casten, Nuclear Structure from a Simple Perspective. Oxford Science Publications, (2000)
- [25] D. R. Inglis, Particle Derivation of Nuclear Rotation Properties Associated with a Surface Wave. Phys. Rev. 96, 1059 (1954)
- [26] D. R. Inglis, Nuclear Moments of Inertia due to Nucleon Motion in a Rotating Well. Phys. Rev. 103, 1786 (1956)
- [27] R. Bengtsson and S. Frauendorf, Nucl. Phys. A327, 139 (1979)
- [28] M. J. A. de Voigt, J. Dudek and Z. Szymański. High-Spin Phenomena in Atomic Nucl. Rev. of Modern Physics 55(4):949-1046 (1983)



- [29] P.A. Pipidis, PhD thesis, the Florida University Collage of Arts and Culture, (2006)
- [30] M. Lipoglavsek, Nucl. Inst. Meth. Phys. Res., A557, 523 (2006)
- [31] G. Nelson and D. Reilly, Gamma-ray Interactions with matter, in Passive Nondestructive Analysis of Nuclear Materials, Los Alamos National Laboratory (1991)
- [32] G.F. Knoll, Radiation Detection and Measurement (John Wiley & Sons, Inc., 2000) 3rd edition
- [33] R.D. Evans, The Atomic Nucleus (McGraw Hill, 1955)
- [34] N. Noorae, PhD thesis, National University of Ireland, Cork, (2014)
- [35] T.S. Dinoko, PhD thesis, University of the Western Cape, (2013)
- [36] J. Gibelin *et al.*, Nucl. Inst. Meth. Phys. Res. A648,109 (2011)
- [37] J.F. Sharpey-Schafer, Introduction to Quantum Physics Notes (Unpublished notes, 2015)
- [38] E.A. Gueorguieva-Lawrie, Introduction to Nuclear Physics Notes (Unpublished notes, 2015)
- [39] E.A.M.A. Khaleel, MSc thesis, University of Stellenbosch, (2011)
- [40] J. Eberth, and J. Simpson, Progress in Particle and Nuclear Physics 60, 283-337 (2008)
- [41] P.M Jones, Nucl. Instr. Phys. A362, 556 (1995)
- [42] P. Regan, Post Graduate Nuclear Experimental Techniques (4NET) Course Notes, University of Surrey Guildford, GU2 7XH, UK, (2003)
- [43] C. Wheldon, PhD thesis, University of Surrey, (1999)

- [44] E. Der Mateosian and A.W. Sunyar, Atomic Data and Nuclear Data Tables, vol.13  
Iss.4 293 (1974)
- [45] K.S. Krane, R.M. Steffen and R.M. Wheeler, Nuclear Data Tables 11, 351 (1988)
- [46] T.E. Madiba, MSc thesis, University of the Western Cape, (2008)
- [47] L. Msebi, MSc thesis, University of Johannesburg, (2016)
- [48] P.J. Twin, Nucl. Inst. Meth. 103, 301 (1971)
- [49] S.P. Bvumbi, MSc thesis, University of the Western Cape, (2008)
- [50] D.C. Radford, ESCL8R and LEVIT8R: Nucl. Inst. Meth. Phys. Res., A361, 297  
(1995)
- [51] [http:// ns.ph.liv.ac.uk/software.html](http://ns.ph.liv.ac.uk/software.html)
- [52] E. Merzbacher, Quantum mechanics, 3rd ed. (John Wiley & Sons, Inc., 1988)
- [53] D.G. Roux *et al.*, Eur. Phys. J. A48, 99 (2012)
- [54] L.L. Riedinger, Nucl. Phys. A347, 141 (1980)
- [55] R. Bengtsson and S. Frauendorf, Nucl. Phys. A327, 139(1979)
- [56] J.F. Sharpey-Schafer, Collective Excitations of Deformed Nuclei and their Coupling to  
Single Particles States Proc. 30<sup>th</sup> Int. Workshop on Nucl. Th., vol.30, Rila Mountains,  
Bulgaria (Eds. A. Georghiera and N. Minkov) pp138-152 (1980)
- [57] J.M. Garrett *et al.*, Phys. Lett. B118, 297 (1982)
- [58] M. Sugawara, Nucl. Phys. A699, 450 (2002)
- [59] L. Chen. *et al.*, Phys. Rev. C83, 034318 (2011)
- [60] S.M. Harris, Phys. Rev. B509, 138 (1965)